EPFL

Thèse n° 8557

Analysis and Modeling of the Dynamics of Traction Forces during Cell Polarization and their Role in the Organization of Edge Activity

Présentée le 9 juillet 2021

Faculté des sciences de base
Laboratoire de physique de la matière vivante
Programme doctoral en physique

pour l'obtention du grade de Docteur ès Sciences

par

Zeno MESSI

Acceptée sur proposition du jury

Prof. R. Houdré, président du jury
Dr A. Verkhovskiy, Dr F. C. Raynaud, directeurs de thèse
Prof. M. Sixt, rapporteur
Prof. M. Balland, rapporteur
Prof. P. De Los Rios, rapporteur

École polytechnique fédérale de Lausanne

2021

We are scientists in our lab
Looking through the microscope
The little glass slides they never lie
How can this small mind cope?
— Amoeba, Adolescents

To my friends and family…

Acknowledgements

This thesis has been a beautiful journey. I discovered what it means to work as a researcher and I want to see more.

First, I would like to thank my two advisors, Sasha and Franck for their unwavering support, insightful guidance and continued friendship. I will always remember happily Sasha's awareness and constant high-level thinking. Everyone who has worked with him knows that if he would say "what a minute...", a very sharp comment or question about a matter that they might have overlooked would rapidly arise and an intense conversation would follow. I cannot be grateful enough to Franck for introducing me to the project and hiring me (twice!).

I also want to thank the members of my thesis jury for their kind advice and comments, Professor De Los Rios, who had already been an excellent teacher throughout my undergraduate studies and supervised, and Professors Balland and Sixt who showed great commitment despite not knowing me before the exam day. I hope that we will be able to collaborate in the future!

Of course, I need to mention Professors Meister, Dietler and Stahlberg who welcomed me in their laboratories and the people I met working there.

Finally, I would like to thank my parents and family for supporting me all the way, my friends who were always interested to hear about little dancing cells and of course a special thought for Charlotte for being there at all times.

Lausanne, February 26, 2021 Z. M.

Abstract

The capacity to break symmetry and organize activity to move directionally is a fundamental property of eukaryotic cells. To explain the organization of cell-edge activity, models commonly rely on front-to-back gradients of functional components or regulatory factors, but they do not explain how the front-back axis is defined in the first place. Recently, a novel and successful principle for self-organization of cell-edge activity was proposed, in which local cell-edge dynamics depends on the distance from the cell center, but not on the orientation with respect to the front-back axis. In this thesis, we test the hypothesis that edge motion is controlled by distance sensing via traction forces.

We show that traction forces exerted on the substrate by polarizing cells are highly dynamical and follow motion of the cell-edge, that stress increases with the distance from the cell center and that maximal forces are located at a fixed distance from the edge near the sites of protrusion-retraction switches. We observe that traction forces correlate with edge extension in cell populations under different experimental conditions. We demonstrate with a fully mechanical model that distance dependence of the force is an emergent property of elastic fiber networks. We next show that dynamics of traction forces and cell-edge motion are correlated during protrusion-retraction cycles, indicating that traction forces trigger the switch from protrusion to retraction. Actin retrograde flow correlates with stress during retraction but not during protrusion suggesting that increase of stress during protrusion is independent of the motion of the actin network. Finally, incorporating a mechanism of cytoskeletal turnover in our model of fiber network we produce systems that display oscillatory fluctuations of their edge and other experimental behaviors.

Our results provide strong evidence that traction forces play a major role in the organization of cell-edge activity and polarization.

Keywords: cell polarization, cell-edge activity, self-organization, traction forces, actin flow, elastic fibers, modeling.

Résumé

La capacité d'organiser les mouvements de leur bord et de briser leur symétrie afin de se déplacer est une propriété fondamentale des cellules eukaryotes. Pour expliquer l'organisation des mouvements du bord de la cellule, les modèles s'appuient généralement sur des gradients de composants essentiels ou d'agents modulateurs allant de l'avant à l'arrière de la cellule mais n'expliquent pas comment la brisure de symétrie s'effectue en premier lieu. Récemment, un nouveau et simple principe d'auto-organisation de l'activité cellulaire dans lequel la dynamique du bord de la cellule dépend de la distance au centre de la cellule, mais pas de la direction du bord par rapport à un axe avant-arrière a été proposé. Ce principe de détection de la distance explique avec succès les mouvements du bord de la cellule avant et après la polarization. Dans cette thèse, nous testons l'hypothèse que les mouvements du bord de la cellule sont contrôlés par un mécanisme de détection de la distance basé sur les forces de traction.

Nous montrons que les forces de traction exercées par la cellule sur son substrat pendant la polarization sont très dynamiques et suivent les mouvement du bord de la cellule, que la contrainte augmente avec la distance au centre de la cellule et que les forces maximales se trouvent à une distance fixe du bord de la cellule près des sites où le bord passe de la protrusion á la rétraction. Nous observons que les forces de traction sont corrélées à l'extension du bord dans des populations de cellules dans des conditions expérimentales différentes. Nous démontrons, à l'aide d'un modèle complètement mécanique, que le lien entre les forces de traction et la distance au centre est une propriété émergente des réseaux de fibres élastiques. Nous montrons que la dynamiques des forces de traction et des mouvements du bord de la cellule sont corrélés pendant les cycles de protrusion-rétraction, indiquant que les forces de traction provoquent le changement du mouvement du bord de la protrusion à la rétraction. Nous montrons que le flux rétrograde d'actine est corrélé à la force de traction pendant la rétraction mais ne l'est pas pendant la protrusion, suggérant que l'augmentation de la contrainte exercée par la cellule sur son substrat pendant la protrusion est indépendante du mouvement du réseau d'actine. Finalement, en incorporant un mécanisme de renouvellement du cytosquelette dans notre modèle, nous produisons des systèmes qui présentent des mouvements oscillatoires et d'autres charactéristiques observées dans des expériences.

Nos résultats apportent des preuves que les forces de tractions jouent un rôle majeur dans l'organisation de l'activité du bord de la cellule et la polarisation.

Mots-clefs : polarisation, activité cellulaire, auto-organisation, forces de traction, flux d'actine, fibres élastiques, modélisation.

Contents

List of Figures

List of Tables

General Introduction Part I

1 Background

1.1 Unravelling Cell Motility

Immune cells slithering between cells and patrolling the body looking for pathogens, fibroblasts migrating to close wounds in connective tissues, spermatozoa swimming up the cervix to fertilize the egg, cell motility is required for many physiological processes (Pollard (2019)). Despite the diversity of modes and functions, motility in all eukaryotic cells relies on the cytoskeleton and motor proteins[1]. The three different protein structures of the cytoskeleton are actin filaments (also called microfilaments), intermediate filaments and microtubules. They all take part in internal organization and scaffolding of the cell but only actin and microtubules are involved in cell migration. Intermediate filaments are merely used to organize the cell internal structure. There are three basic types of motility in eukaryotes, one with microtubules and two involving actin.

Microtubules make up cilia and flagella, permanent beating organelles used for motion. Cilia are found in large numbers on the cell surface. In addition to motion, certain epithelial cells use cilia to move substances or particles surrounding them. Such cells can be found for example in the trachea. There is generally only one or two flagella per cell. They look like tails and are used to propel the cell. It is the means of locomotion of spermatozoa (Fig. 1.1 a). The structure and functioning principle of cilia and flagella are the same. They are elongated protrusions composed of microtubule beams surrounded by a membrane: 9 microtubule doublets arranged in a circular fashion around a central pair ("9 + 2" structure). Apart from the unavoidable biological exceptions, this structure is universal among all eukaryotic cells (Chaaban and Brouhard (2017)). Crosslinkers and molecular motors dynein connect adjacent pairs. Coordinate movement of dyneins gives rise to bending waves traveling along the beam thus allowing the cell to move (Fig. 1.1 a). Flagellar based *swimming* motility also exists in prokaryotes, but the structure and operation mechanism are completely different.

Actin is featured in the two other and most prominent types of motility. Both require specific molecular motor myosin II that binds actin. Cells that adopt *blebbing* migration

[1] There is only one known exception, spermatozoa of the nematode *C. elegans* use a cytoskeletal protein specific to them and do not require molecular motors to move.

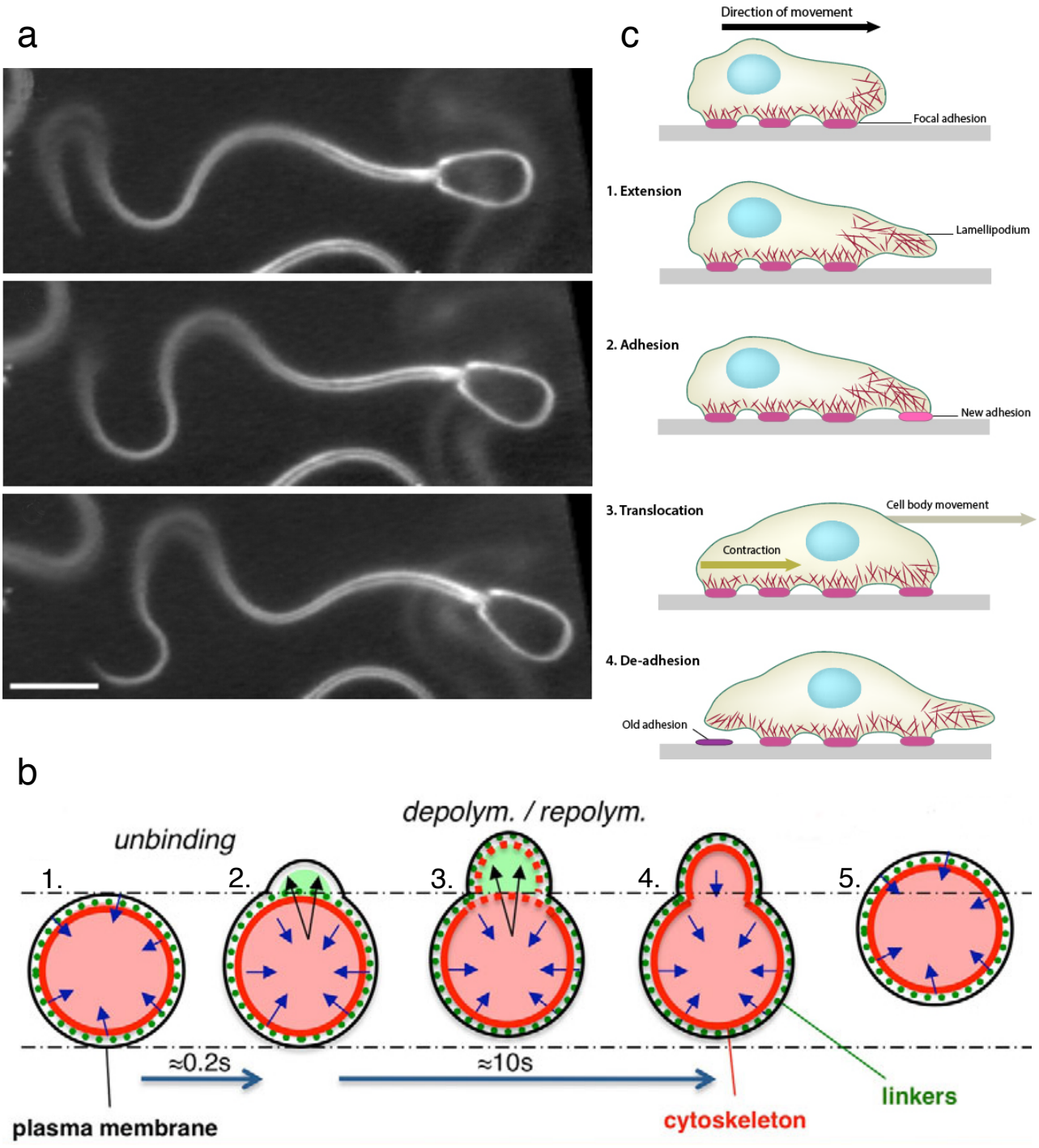

Figure 1.1 – Three types of cell motility. Legend on the next page.

form rounded protrusions (blebs) used to extend their body in the direction of motion while myosin mediated contractility retracts their back (Fig. 1.1 b). Blebs, which also appear during apoptosis, are formed when the *cell cortex*, a thin contractile actin and myosin (actomyosin)

Figure 1.1 – Three types of cell motility. (a) Flagellar motility. Three snapshots of a spermatozoon swimming showing the propagation of the bend in the flagellum. Pictures were taken $200ms$ apart. Scale bar, $10\mu m$. Figure taken from Woolley et al. (2009). (b) Steps of blebbing motility. 1. Initial state, membrane is attached to the cell cortex all round the cell 2. Plasma membrane locally detaches from the cell cortex forming a bleb 3. Old cell cortex depolymerizes and actin repolymerizes in the blebb. 4. New cortex has fully matured and is reattached to the cell membrane, pressure is reestablished. 5. Back of the cell retracts and the cell has moved (same state as 1.). Blue arrows denote internal pressure. Solid and dashed red lines respectively depict mature and (de)polymerizing actin cortex. Green dots represent proteins crosslinking actin to the plasma membrane. Adapted from Maugis et al. (2010). (c) Crawling cell motility split in 4 stages. 1. Actin filaments (red segments) are polymerized at the leading edge and form a membrane (green) protrusion, the lamellipodium. 2. New adhesions (pink) between the network of actin filaments and the extracellular matrix (gray) are rapidly established. 3. Combined activity of retrograde actin movement and contractile forces produced by stress fibers generate tension to pull the cell body and nucleus (light blue) forward. 4. Forces produced by the contractile network, combined with actin filament and focal adhesion disassembly, help to retract the trailing cell edge. Source: mechanobio.info, redrawn from (Ananthakrishnan and Ehrlicher (2007)).

network attached to the membrane, locally contracts and detaches from it. The cytosol, driven by internal pressure, is extruded between the membrane and the network inducing a spherical bulge in the membrane. The cortex is then extended and reattached to the membrane (Maugis et al. (2010)). This type of motion does not require strong adhesions and is particularly well suited for confined environments in because it does not rely on any cell-substrate bindings. In that case, cells exert forces perpendicular to the substrate to maintain their body in position while extending a new bleb or retracting their back (Charras and Paluch (2008)). Cells like neutrophils (motile immune cells), and certain amoeba use this type of motility.

Adherent cells, e.g. fibroblasta and epithelial cells, display *crawling* or *lamellipodial* motility. Briefly, actin is polymerized at the leading edge pushing the membrane forward and creating new adhesions with its substrate. Contraction of the actomyosin network together with disassembly of actin filaments and adhesions induce retraction of the trailing edge in the back of the cell (Rafelski and Theriot (2004)). See Fig. 1.1 c for a schematic description of the stages of crawling. The large thin protrusion at the leading edge is called the *lamellipodium*. Contrary to blebs, the lamellipodium is flat. Another great difference with blebbing and swimming motility is that crawling requires specific cell-substrate adhesions. Cells displaying this type of motility are surrounded by a protein network called the *extracellular matrix* (ECM). It is generally made of a network of adhesive proteins like collagen and fibronectin which the cells can bind to. The network is secreted by connective tissues cells like fibroblasts (Kendall and Feghali-Bostwick (2014)). Unlike cilia and flagella, both lamellipodia and blebs are very dynamic structures: they appear and disappear on the scale of minutes or seconds[2] and can form from any place at the cell surface. Lamellipodium and bleb-based motility are

[2] A bleb can form in a few tenth of seconds ! (Maugis et al. (2010))

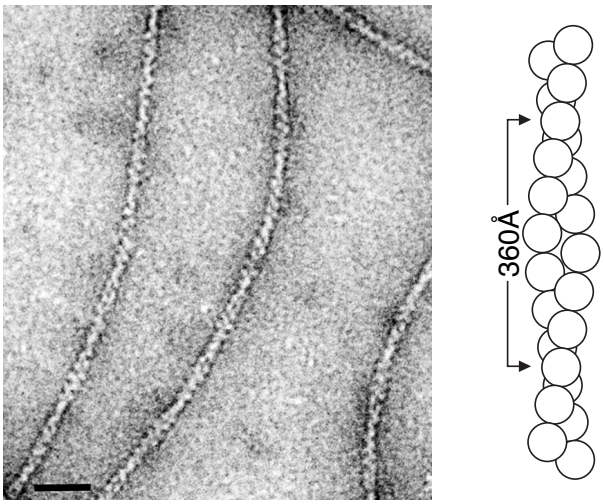

Figure 1.2 – Electron micrograph of negatively stained actin filaments and sketch showing the length of a half twist. Scale bar $20nm$. Adapted from Craig (2017)

not mutually exclusive. They sometimes can be employed by the same cells. Hybrid type of crawling displaying blebs and lamellipodia at the same time have been reported in compliant 3D environments (Sixt (2012)).

Despite being ubiquitous and despite the large number of studies devoted to actin-based motility, it is still not completely understood. Contrary to flagellate motility, it does not rely on a dedicated and permanent organelle but rather on organization and coordinate motion of the whole cell body. How cells establish and sustain directional motion is still debated. What mechanism causes them to form and maintain a constantly protruding front and retracting back ? What system coordinates actin polymerization and depolymerization, adhesion formation and dissassembly, and cell contractility to orchestrate cell motility ? Using both experiments and modeling conducted with fish epidermal keratocytes, a model system known for the persistence of its motion, this study addresses the question of how the processes of actin-based motility are coordinated at the cellular level. Before diving into our results, we are going to introduce basic notions. We will present main components of motile machinery: actin, myosin and adhesions, and the mechanisms involved. A brief review of mechanisms of regulation of cytoskeletal activity and motility models will be made and finally we will present the direction we chose for this work.

1.2 Actin structure and assemblies

Actin is the thinnest cytoskeletal filament. It consists of a double helix of diameter $5-9nm$ with a twist length of $72nm$. It is composed of a single type of monomer: globular actin (G-actin)(Fig. 1.2). Since monomers are asymmetric and they all face the same direction in the polymer, filamentous actin (F-actin) is polar. Its two ends are called barbed (+) and pointed (−) (Dominguez and Holmes (2011)).

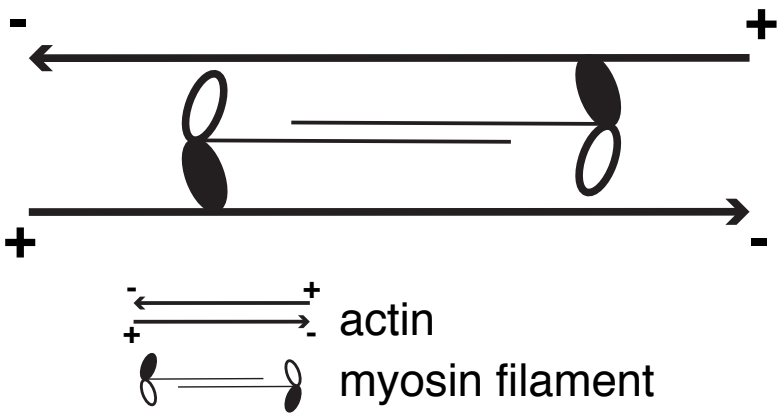

Figure 1.3 – Actomyosin organization. Schematic diagram illustrating organization of actin and myosin in the actomyosin complex. Arrows indicated the direction of motion of actin. Barbed end and pointed end are marked, respectively + and −. Filled myosin head is bound to actin. Inspired from Langanger et al. (1986).

Overcoming Flexibility

Much weaker than microtubules, F-actin has a persistence length close to $20\mu m$ (Gittes et al. (1993)) which is about the same as the cell radius. However, it is generally organized in crosslinked bundles or branched networks which are rigid enough to scaffold protrusions and stabilize the cell structure. Actin networks are found at the leading edge of motile cells in the lamellipodium. It is the center of actin polymerization. In addition, there are two types of actin bundles. *Filopodia* are slender protrusions sticking out of the lamellipodium. They are made of parallel actin filaments held together in a bundle by crosslinkers and are used in various processes like environment sensing, creating new adhesions and transmitting cell-cell signals (Mattila and Lappalainen (2008)). The second type of actin bundle is not a protrusive structure but rather contractile. *Stress fibers* are used to create tension in the cell and require myosin to operate (Pellegrin and Mellor (2007)).

Myosin and Actomyosin

Myosin is the molecular motor family that specifically binds and walks on actin filaments. There are several different myosin classes involved in various processes. Many are used to transport cargo along actin filaments (e.g. myosin I, V or VI). On top of that, other myosins are involved in highly specific tasks. For example, myosin VIIa is essential for organization of stereocilia[3] bundles, the sensory receptors of the auditory system found in the inner ear (Li et al. (2020)). But the most remarkable class is myosin II. Historically found first in muscle cells, myosin II forms, together with actin, a protein complex called *actomyosin*. This assembly is *the* protagonist of cell contractility. It is found in essential cell processes at all stages of life and

[3]The name is misleading, even though they are called cilia, stereocilia are actin based protrusions.

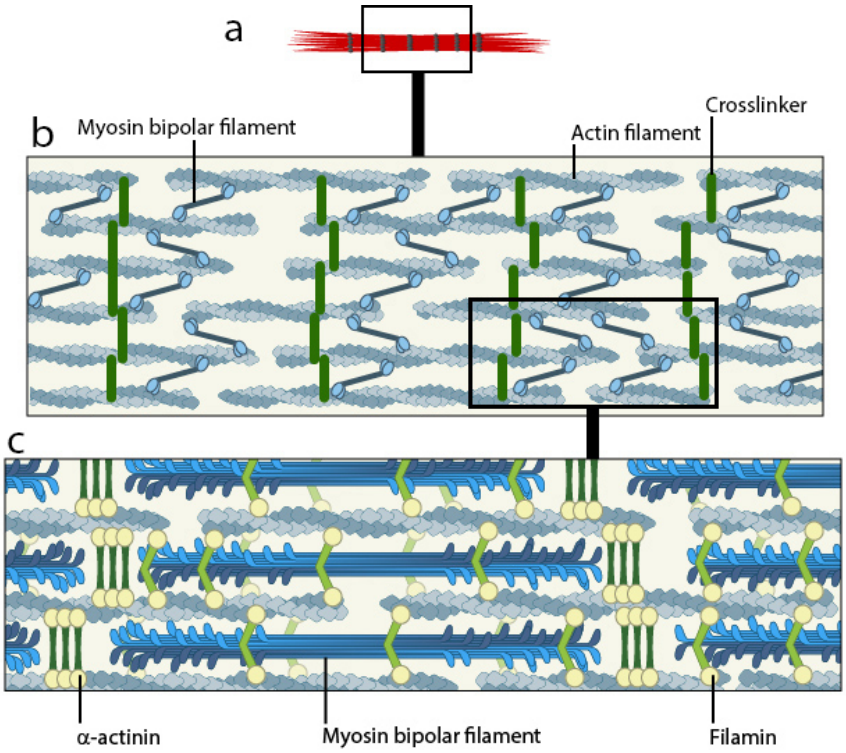

Figure 1.4 – Sketch of a stress fiber. (a) Isolated stress fiber with bundled actin filaments (red) and crosslinking proteins (black) (b) Between actin filaments lie myosin II filaments and crosslinkers. (c) A high resolution view shows bipolar myosin filament are situated between regions rich in crosslinker α-actinin. Filamin, another crosslinking protein is distributed along the entire stress fiber. Source: mechanobio.info

at all scales. It it responsible for muscle contraction, from arm wrestling to vasoconstriction. During embryonic development, it drives the formation of folds in the embryo (Munjal and Lecuit (2014)). At the level of the cell it is used during cell division to separate the two daughter cells (Cheffings et al. (2016)). Finally, actomyosin is primordial for cell motility, it participates in remodeling of actin structures and generates *traction forces* used by the cell to maintain physical integrity and move (Lauffenburger and Horwitz (1996), Cramer et al. (1994)).

Understanding actomyosin operation requires a more detailed description of actin and myosin. Polarity of actin filaments implies that myosins move on actin filaments in a preferred direction[4] (Wells et al. (1999)). Myosin molecules of all types comprise a head domain that binds actin and hydrolyses ATP to generate force, a neck that can bind regulatory proteins and a tail that binds cargo, lipid membranes or other myosin molecules (Vale (2003), Sellers (2000)). Sequential binding, hydrolysis and release of ATP induce conformational changes to the protein allowing it to advance step by step on actin filaments. This process is called the *powerstroke cycle* (Tyska and Warshaw (2002)). During the step, the motor exerts a force of a few piconewtons (Finer et al. (1994)). Some myosins, like myosin II can form dimers

[4] All myosins, except type VI travel from the − end towards the + end (Sellers (2000)

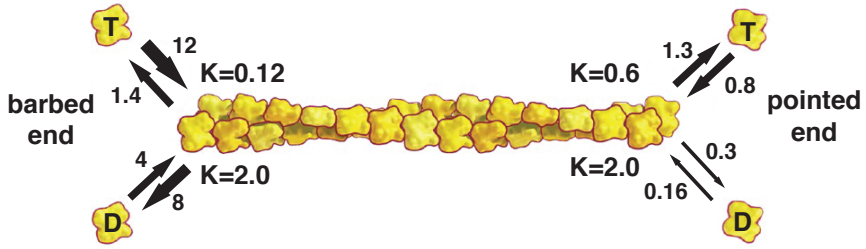

Figure 1.5 – Binding rates of actin monomers onto an actin filament. Actin monomers are shown in yellow. Letters **T** and **D** denote ATP-bound and ADP-bound monomers. Arrows with number show association $\left[\mu M^{-1} s^{-1}\right]$ and dissociation $\left[s^{-1}\right]$ rate constants. Dissociation equilibrium constant K is given in μM for each reaction. Aging of the actin monomer is not shown. Note that the equilibrium constant of ATP-bound actin is much lower at the barbed end than at the pointed end. This gives rise to treadmilling. Modified and corrected from artwork in Pollard and Borisy (2003)

consisting of two parallel molecules with their tails interlaced. Moreover, myosin II can form filaments of several parallel and antiparallel stacked dimers. The resulting bundle has head domains at both ends pointing in opposite directions. Thus movement of the myosin heads along actin filaments of opposite polarity generates a sliding motion that results in contraction. Figure 1.3 shows a sketch of actomyosin structure and operation. Several actomyosin units can then be assembled in series and in parallel. Sarcomeres, the contractile structure found in muscles, feature a very regular stacking of actin filaments intercalated with myosin filaments (Henderson et al. (2017)). In motile cells, another structure is found : *stress fibers* (Tojkander et al. (2012)). They are used to exert forces on the cell substrate. They are made of crosslinked antiparallel actin bundles and are less regular than sarcomeres (Fig. 1.4).

1.3 Actin Lifecycle

In the cell, actin filaments are assembled, barbed end forward, at the leading edge in the lamellipodium (Fig. 1.6). The lamellipodium is an almost flat protrusion. It is only a few hundreds of nanometers thick while it is up to tens of micrometers wide (in the direction perpendicular to motion) and a few micrometers along (in the direction of motion). The reason for flatness of the lamellipodia is still debated but recent works have reported that polymerization factors localize preferentially in highly curved regions of the membrane thus promoting protrusion only at the very edge of the cell (Schmeiser and Winkler (2015), Peleg et al. (2011)).

Actin Treadmilling

The first step of actin polymerization is called nucleation. It is the formation of an actin oligomere from which the filament will elongate. The process is spontaneous but inefficient.

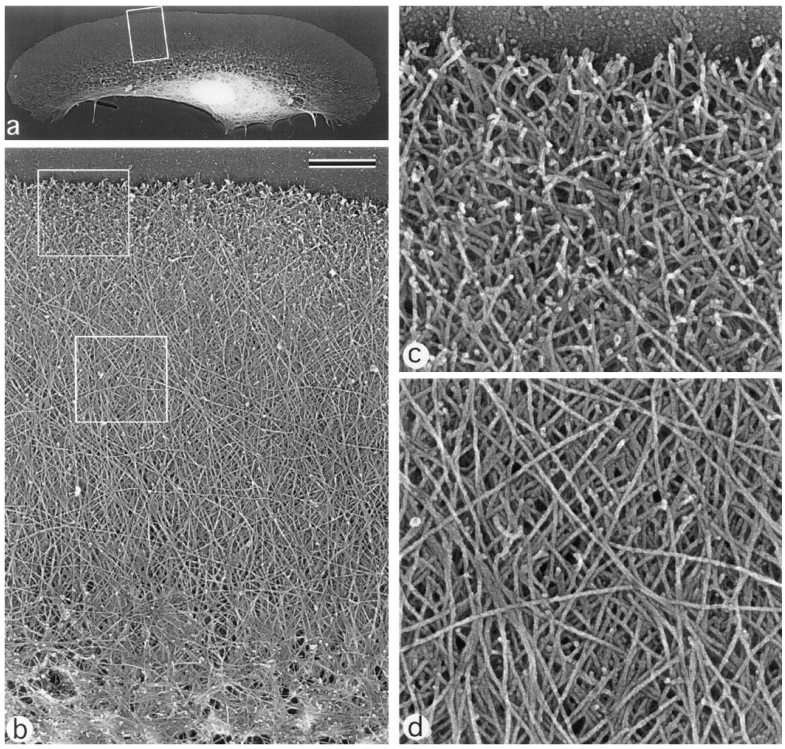

Figure 1.6 – Electron micrograph of the actin cytoskeleton of a locomoting fish epidermal keratocyte. (a) whole cell. (b) actin network in the lamellipodium. (c) dendritic zone near the leading edge. (d) smooth actin filament network in the middle part of lamellipodium. Scale bar $1\mu m$. Taken from Svitkina et al. (1997)

Short actin oligomeres (dimers and trimers) are unstable (Liu et al. (2013)). However, addition of more subunits stabilizes the assembly. Actin monomers can bind and hydrolyze ATP which in turn affects their binding rates. ATP dramatically increases the binding rate and overall affinity of actin monomers to the filament barbed end. Also, ADP-bound actin (ADP-actin) associates slower and dissociates faster from the barbed end than ATP-bound actin (ATP-actin). Finally, the dissociation rates at the pointed end are slow and similar for both species (Pollard and Borisy (2003)). Schematically, elongation of the filament happens at the barbed end where ATP-bound monomers are constantly added, ATP is hydrolyzed in the filament (ATP-hydrolysis rate of F-actin is orders of magnitudes greater than the one of G-actin) and ADP-bound monomers are removed at the pointed end (Fig. 1.5). It is the hydrolysis of ATP that makes possible simultaneous addition of subunits at one end of the filament and dissociation from the opposite end. In the steady state, if monomers are free to diffuse around, the filament will advance. This mechanism is called *treadmilling*. In absence of any regulatory protein, treadmilling is fairly slow. In vitro, at steady state and under physiological ion conditions, the dissociation rate at the pointed end limits filament treadmilling speed to $0.04\mu m \cdot min^{-1}$ whereas epidermal keratocytes can typically reach $10\mu m \cdot min^{-1}$ (Fig. 1.1 c, Kuhn and Pollard (2005)). To achieve this in vivo, actin polymerization is aided and regulated by many accessory proteins.

Regulation of actin filament polymerization, organization and disassembly is a complex process involving numerous components and interactions. A lot of regulatory pathways eventually loop and thus setting a starting point is arbitrary. We have chosen to start with membrane bound regulators of actin polymerization. We tried to avoid redundancy, however, critical components and concepts will be briefly described when they are mentioned even if a thorougher description is made further in the text.

Initiation

Initiation of actin assembly in eukaryotic cells is regulated by the Rho family of GTPases (Fig. 1.7, 1-3). It consists of several subfamilies. The most prominent subfamilies regulate the formation of different actin structures: Rac for lamellipodia, Rho for stress fibers and Cdc42 for filopodia (Pellegrin and Mellor (2007)). These proteins are switches that can be turned on by different signals sensed by transmembrane receptors. Signals can be chemical or mechanical. Neutrophils, for example, react to chemoattractant gradients, protrusion will be initiated closest to the source (Van Haastert and Devreotes (2004)). Regulators of these proteins are also associated with cell-substrate adhesions, regulating actin polymerization, and stress fiber formation near these contacts (Geiger and Yamada (2011)).

The regulatory pathways following the activation of these proteins are vast and promote a wide range of cellular activities other than migration, like, phagocytosis or fate determination (Heasman and Ridley (2008)). The detailed description of these signaling cascades goes beyond the scope of this chapter (review in Hall (2012)).

In addition to GTPases, membrane lipids of the phosphoinositide family residing in the interior of the plasma membrane also regulate membrane proteins, promoting actin polymerization and activity of the plasma membrane such as phagocytosis.

Dendritic Network and Accessory Proteins

Downstream from the main signaling entities, nucleation promoting factors (NPFs) are used to facilitate the actin nucleation process. Cdc42 and Rac activate proteins of the WASP/SCAR/WAVE family which in turn activate the *Arp2/3 complex* (Fig. 1.7, 3), one of the main actin filament nucleators in the cell (Pollitt and Insall (2009)). In the lamellipodium, the Arp2/3 complex binds to the side of an existing filament and initiates nucleation and elongation of a new filament that branches from the first one (Fig. 1.7, 4). This process is called *dendritic nucleation*. The model was first introduced in Mullins et al. (1998) and extensively expanded since then (Nicholson-Dykstra et al. (2005), Higgs (2018)). The angle between the branches is around 70° (Vinzenz et al. (2012), Volkmann et al. (2001)). It is determined by the geometry of the Arp2/3 complex and location of the binding sites. Repetition of the branching process creates a dense "brushlike" network of short branched actin filaments that underlies the protrusion (Fig. 1.7 and 1.6, c)). The brushlike network is around $1\mu m$ thick (in the direction of motion) (Svitkina et al. (1997)). The other main nucleation promoting factor is formin (Breitsprecher and Goode (2013)). Unlike Arp2/3, formins promote formation of long un-

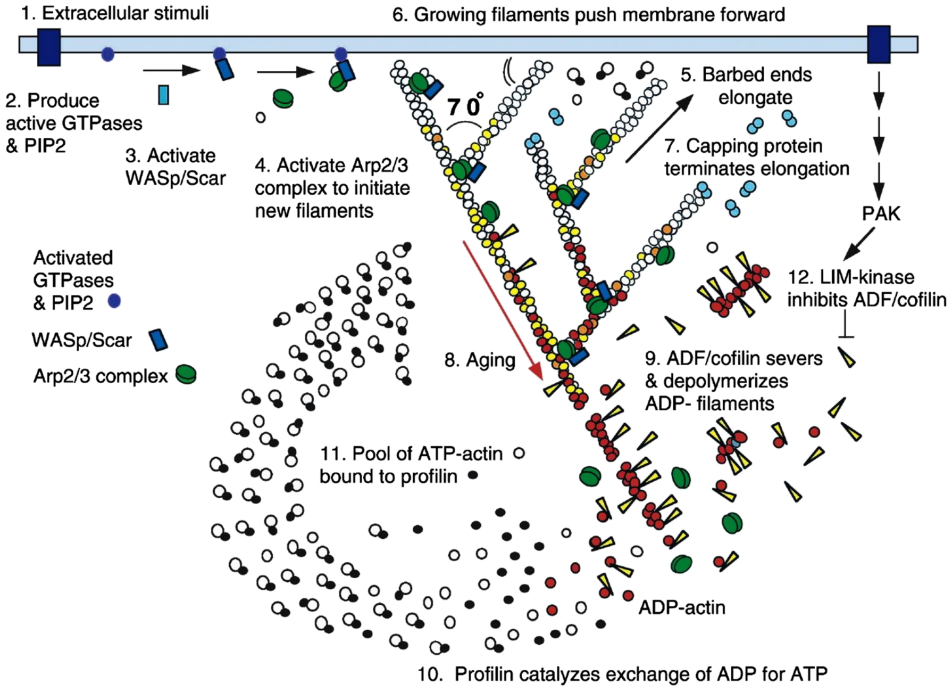

Figure 1.7 – Dendritic Nucleation model for leading edge protrusion and treadmilling. (1) Extracellular signals activate receptors. (2) The associated signal transduction pathways produce active Rho-family GTPases and PIP2 that (3) activate WASp/Scar proteins. (4) WASp/Scar proteins bring together Arp2/3 complex and an actin monomer on the side of a preexisting filament to form a branch. (5) Rapid growth at the barbed end of the new branch (6) pushes the membrane forward. (7) Capping protein terminates growth within a second or two. (8) Filaments age by hydrolysis of ATP bound to each actin subunit (white subunits turn yellow) followed by dissociation of the γ-phosphate (subunits turn red). (9) ADF/cofilin promotes phosphate dissociation, severs ADP-actin filaments and promotes dissociation of ADP-actin from filament ends. (10) Profilin catalyzes the exchange of ADP for ATP (turning the subunits white), returning subunits to (11) the pool of ATP-actin bound to profilin, ready to elongate barbed ends as they become available. (12) Rho-family GTPases also activate PAK and LIM kinase, which phosphorylates ADF/cofilin. This tends to slow down the turnover of the filaments. Taken from Pollard and Borisy (2003)

.

branched actin filaments. In particular, they are proposed to participate in the fomation of filopodia. There are two main models of filopodia formation (Yang and Svitkina (2011)). The *convergent elongation model* describes the formation of filopodia from an existing dendritic network. In this model, formin would only promote parallel elongation of existing filaments. In the *tip nucleation model* filaments are nucleated directly by a cluster of formins on the plasma membrane which readily produces a bundle of elongating actin filaments without involving any prior actin structure. However, these models are not mutually exclusive and there is experimental evidence for both. Formins are also involved in the formation of stress fibers (Hotulainen and Lappalainen (2006)).

Other regulatory proteins come into play (Fig. 1.7, 7-11). By stopping elongation of filament barbed ends, capping proteins increase the ratio of dissassembling pointed end with respect to assembling barbed ends and provide for fast elongation of the subset of barbed ends that are not capped. This process maintains network dendritic morphology and accelerates treadmilling (Svitkina et al. (2003), Shekhar and Carlier (2017)). Cofilin severs filaments and accelerates depolymerization of ADP-actin. This increases the steady state concentration of free actin monomers and filament turnover rate (Shekhar and Carlier (2016)). Profilin binds to actin monomers barbed ends preventing them to be added to filaments pointed end. This allows for high concentration of monomeric actin without increasing association at the pointed end. Profilin also catalyzes the exchange of ADP for ATP (Korenbaum et al. (1998), Selden et al. (1999), Wolven et al. (2000)). These proteins and many others orchestrate the growth and sustain the lamellipodial dendritic network (Carlier and Shekhar (2017)).

Different crosslinkers can bind actin and scaffold structures. Here are a few examples. Fascin is found at the cell leading edge where it bundles actin in filopodia (Yang and Svitkina (2011)). α-actinin is the primary crosslinking protein of stress fibers (Tojkander et al. (2012)) and can interact with cell-substrate adhesions (Sjöblom et al. (2008)). Filamin is a versatile crosslinker that scaffolds the actin in the lamellipodium, bundles filaments in stress fibers and anchors actin to transmembrane proteins (van der Flier and Sonnenberg (2001)). Various crosslinkers are not restricted to a unique purpose, they are often associated to multiple processes.

Stress Fibers

Away from edge of the cell, the network of actin filaments becomes smoother with longer filaments (Fig. 1.6, b and d). Filament orientation changes and they start forming bundles. Myosin concentration increases (Svitkina et al. (1997)). This part of the cell between the lamellipodium and the cell body has a distinct organization of actin network and is called the *lamellum*. On the way from lamellipodium to lamellum a part of actin filaments is dissassembled and the other part is reorganized (Ponti et al. (2004), Alexandrova et al. (2008)). Myosin II plays a major role in reorganization of the network. Forces generated by myosin filament clusters drive reorientation of actin filaments and produce contraction by sliding the actin filaments relative to one another (Schaub et al. (2007)). This mechanism promotes formation of antiparallel actin bundles (Verkhovsky et al. (1995)) which are further stabilized by crosslinker α-actinin. These bundles are called *stress fibers* (SF) and count tens to hundred actin filaments (Fig. 1.4). They are anchored to the ECM through *focal adhesions* (FA), integrin-based cell-substrate linkages regulated by the same GTPases families as stress fibers. Relative motion of actin filaments in the actomyosin complexes allows cells to exert forces on the ECM. In this way, stress fibers provide shape stability and drive cell migration.

Adhesions

Cell-substrate adhesions are protein complexes that connect the actin cytoskeleton to the extracellular matrix. Cytoskeleton and adhesion dynamics are closely related. On one hand, actin binding and forces generated in the cytoskeleton organize assembly, growth and turnover of cell-substrate contacts. On the other hand, adhesions promote actin polymerization and its organization into force-generating stress fibers. Other important cellular processes are associated with adhesions like cell migration, fate and even differentiation (Geiger et al. (2009), Engler et al. (2006)).

Adhesions are composed of a transmembrane protein called the *receptor* and a large variety of cytoplasmic proteins. In cell migration, *integrins* are the most common and best characterized receptors. The adhesion receptor binds ECM proteins like fibronectin. Inside the cell, large complexes of actin-associated proteins bind the receptor and provide a link to the cytoskeleton. Actin does not interact directly with the receptor. Protein complexes connecting actin to the receptor contain both versatile actin crosslinkers like α-actinin or filamin and other components specific to adhesions like talin and vinculin. Rather than just linking actin to integrins, these proteins play a crucial role in adhesion regulation. They include binding sites for promoters of actin polymerization. Binding of actin to talin promotes activity of the adhesion site by increasing the affinity of integrins to their ECM ligands (Ginsberg (2014)). Binding of vinculin to talin triggers the clustering of activated integrins (Humphries et al. (2007)) and strengthens the link between actin and integrin (Galbraith et al. (2002)). Adhesion proteins also bind to molecules promoting actin polymerization like small Rho GTPases and Arp2/3 (Parsons et al. (2010)). For example, focal adhesion kinase (FAK), one of these adhesion proteins, comes in the early stages of adhesion formation and binds to other components and signalling molecules helping their recruitment (Geiger et al. (2009)). The entire collection of molecules associated with integrin-based adhesions (or adhesome) is huge. It counts more than 180 identified components and more than 700 direct interactions between them (Geiger and Yamada (2011)).

Integrin-based adhesions, like the cytoskeleton, are highly dynamical structures regulated by chemical signalling and mechanical factors and in their turn they generate mechanical and chemical signals to the cytoskeleton (Roca-Cusachs et al. (2012)). Adhesions are formed in the lamellipodium close to the leading edge. Early or *nascent* adhesions are small dot-like structures which are dynamic. Early contacts are made of a limited number of molecules. These contacts can then rapidly turn over or mature into larger focal complexes. This happens further from the edge at the interface between lamellipodium and lamellum where actin rearranges and a lot of filaments are depolymerized (Alexandrova et al. (2008)). As they grow, focal complexes become more elongated. More actin filaments bind the adhesive site. Other components bundle the filaments and scaffold an increasing number of integrin molecules. Mature or *focal* adhesions are found in the lamellum at the tips of stress fibers (Geiger et al. (2009)).

Adhesions are mechanical and chemical signal transducers. They play a central role in a

variety of signalling cascades (Juliano (2002), Geiger et al. (2009)). Formation, maturing and dissassembly of adhesions strongly depends on mechanical stimuli. Cells cultured on stiffer substrate display larger adhesions than the ones plated on soft substrates (Guo et al. (2006)). Focal adhesions can form and grow only if they experience pulling forces through their actin connections (Geiger and Yamada (2011)). Adhesion formation is coupled to actin polymerization and myosin II contractility promotes their maturation (Parsons et al. (2010), Choi et al. (2008)). Formation of nascent adhesion does not require myosin II (Choi et al. (2008)). Actin pulls on adhesions via polymerization- and myosin-driven forces. These forces promote reorganization of scaffolding and signalling molecules composing the adhesions. Stretching of individual elements also induces important conformational changes. For example, talin can unfold under stress exposing otherwise inaccessible binding sites for vinculin (Martino et al. (2018)). This is the case of many components of the adhesome, including ECM ligands (Hu et al. (2017), Martino et al. (2018)). Finally, stress fibers and focal adhesions mutually contribute to their assembly and maturation. On one hand, focal adhesions lay a template for stress fibers formation by recruitment of Rho GTPases, myosin and α-actinin and on the other hand, force generated by stress fibers favors growth of focal adhesions (Burridge and Guilluy (2016)).

Actin Flow and Cell-Substrate Coupling

Despite the existence of mechanical connections between cellular matrix, adhesions and actin cytoskeleton, the parts of this system exhibit continuous relative motion as it was shown in Alexandrova et al. (2008). In non-motile cells, filamentous actin flows centripetally from the periphery towards the cell center. In migrating cells, it travels from the front to the back of the cell. This constant movement of F-actin is called *actin retrograde flow* (ARF). Adhesions also move with respect to the ECM but at lower velocity (Gupton and Waterman-Storer (2006)). Retrograde flow is due to pressure of the membrane and cellular cortex pushing against polymerizing actin, and myosin II mediated contractility. Forces generated in the cytoskeleton are transmitted to the extracellular matrix via dynamic interaction between flowing actin and integrin-based adhesions.

Motile cells also display anterograde actin flow (Vallotton et al. (2005)). Far from the leading edge, where the cell body is located, F-actin moves in the direction of motion (Vallotton et al. (2004)). This anterograde flow of actin is associated with the constant retraction of the trailing edge and is mediated by myosin II contractility that pulls on bundled actin filaments. The retrograde and anterograde flows meet in a *convergence region* with near zero actin flow (Vallotton et al. (2004)). It corresponds to a region of high concentration in myosin II and cell-substrate adhesions where the actin filaments composing the network are depolymerized or reorganized into bundles (Gupton and Waterman-Storer (2006)). Flow speed thus depends on the position in the cell, from the leading to the trailing edge. The lamellipodium is characterized by fast actin retrograde flow. Within the lamelliopodium, actin flows at a rate of a few micrometers per minute. Speed decreases in the lamellum. Adhesions slow down the flow until it stops in the convergence zone. Finally, it changes sign at the back of the cell (Ponti et al.

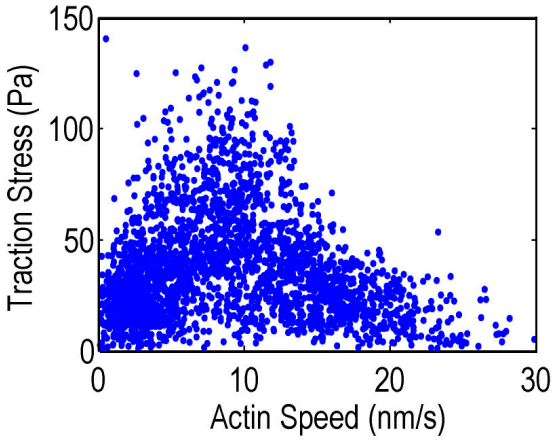

Figure 1.8 – Biphasic relationship between traction forces and actin retrograde flow rate. Stress correlates positively with actin speed for low velocities. It reaches a maximum around $10nm/s$ and decreases thereafter. Taken from Gardel et al. (2008)

(2004), Alexandrova et al. (2008), Vallotton et al. (2004)).

Flow speed also varies along the edge of the cell. For example, in locomoting keratocytes, flow was reported to be up to 4 times higher in the flanks than in the middle (Vallotton et al. (2005)). During migration, keratocytes keep their shape constant (Fig. 1.10). This implies protrusion rate is graded along the cell's leading edge (with the highest rate at the central part and diminishing towards the sides) (Lee et al. (1993)). This kinematic rule explaining conservation of keratocyte shape was called *graded radial extension*. Increased flow rate at the flanks contributes to slowing down of protrusion and maintenance of the shape of lamellipodia (Barnhart et al. (2011)). Variation of flow rate could also contribute to the variation of overall speed of the cell. Flow speed in the middle of the leading edge is negatively correlated with speed of the cell (Jurado et al. (2005)). The faster the cell, the slower the flow and vice versa. And accross cell types, retrograde flow is fast in stationary or slowly moving cells and slow in rapidly moving cells like keratocytes (Gardel et al. (2010)).

Given the existence of flow, the question arises how forces generated by the cytoskeleton are transmitted to the adhesions and ECM. The leading idea is that coupling between ECM and actin cytoskeleton could be locally variable and regulatable by a *molecular clutch*. When the clutch is engaged, interaction between actin and cell-substrate adhesions oppose to the flow. ARF is slowed down and the forces created by actomyosin contractility are transmitted to the substrate allowing the cell to grow a protrusion or exert traction. This hypothesis predicts that rapidly moving cells will exhibit slow flow and inversely as observed experimentally (Gardel et al. (2010)). There is lot of mutual interactions between the flow and adhesions. On one hand, it has been shown that adhesions slow actin flow and help remodelling the actin network, and on the other hand actin network moving with the retrograde flow reorients adhesions and reinforces the link between integrins and actin filaments through modifying tension-sensitive molecules like talin (Alexandrova et al. (2008), Yamashiro and Watanabe (2014), Swaminathan et al. (2017)). Diminishing actin flow via inhibition of actin polymerization or myosin II

contractility impairs focal adhesion formation (Swaminathan et al. (2017)).

Relationship between velocity of the flow and force transmitted to adhesions is not trivial. It was shown that traction forces are biphasically correlated with F-actin speed at adhesion sites (Fig. 1.8, Gardel et al. (2008)). For low velocities, stress grows with the flow rate until a critical value beyond which it decreases (Fig.1.8). Several models of the clutch mechanism were proposed to reproduce this biphasic behavior. We briefly present two different approaches: stochastic and mechanical. Theoretical work introduces integrin receptors on an actin moving at constant speed that can bind to ECM ligands in a stochastic model (Li et al. (2010)). The interaction is modelled in 4 steps: ligand-receptor complex forms, stretches, breaks and the free proteins relax to their equilibrium conformation. Two types of stretch-dependent binding kinetics are considered: *catch-bond* that strengthens with applied force until it reaches a certain value and weakens thereafter, and a *slip-bond* which lifetime simply decreases with applied force. These are two commonly used assumptions about the kinetics of the bond. The behavior of the two bonds were examined with a master equation and observables such as fraction of bound integrins as a function of the flow were measured. With a relevant choice of parameters, the catch-bond was found to display a robust biphasic behavior in the number of bound integrins and stress as a function of retrograde flow rate. Considering that any of the many protein–protein interactions between the substrate and actin filament network can break, a multiple layer version of the model was developed. This version, which was treated numerically, also gave results in good agreement with experimental results. Another stochastic model with a retrograde flow driven by a constant force but moving at a variable speed was proposed that also displays biphasicality (Sabass and Schwarz (2010)).

A different way of describing the mechanism is modeling actin as a gel. Authors of Craig et al. (2015), for example, modeled actin as a one-dimensional newtonian viscous fluid interacting with myosin and adhesions, with mechanical equations for the evolution of the system. The displacement of actin network at a distance x inward from the cell leading edge is described as

$$\mu \partial_x^2 V = T(x) - F_{myo}(x) \tag{1.1}$$

with μ the viscosity coefficient of the gel, V the flow speed, T the traction force and F_{myo} the actomyosin contractility mediated force. The traction force is proportional to the flow speed and the local density of adhesions $T = \zeta N_{adh} V$. The contractility generated force depends on the gradient of attached myosin $F_{myo} = f \partial_x M$. Myosin can attach to and detach from the actin network with rates m_{on} and m_{off} respectively. Attached myosin is transported by the flow in an advective manner, hence the equation for attached myosin density evolution

$$\partial_t M = m_{on} - m_{off} - \partial_x V M. \tag{1.2}$$

Regarding adhesion density, authors consider a model where adhesion are strengthened by myosin activity and weakened by actin flow. Assembly rate is proportional to F_{myo} and disassembly rate grows exponentially with V to account for strengthening of the adhesion with force reflects weakening of adhesions by fast flow. Results from this work include biphasic

behavior of the traction force with velocity of the flow. Interestingly, the spatial variable allows for a prediction of the flow, stress and adhesion density profiles match experimental results. However, the choice of

Life on a Flat Surface

The vast majority of cell biology experiments is performed using flat substrates. Cells are plated on coverslips coated with ECM proteins and immersed in culture media. They are observed outside of their normal living conditions in environments having flat topology. Historically, microscopy techniques allowed to image only thin and flat samples. Today, development of high resolution light sheet microscopes provides solutions for 3D imaging (Chen et al. (2014)). Moreover, emergence of two-photon microscopy allows now for *in vivo* imaging (Hierro-Bujalance et al. (2018)). Multicellular organisms live in a tri-dimensional environment embedded in a large system it would natural to analyse them in their native environment. However, these techniques produce overwhelming amounts of data, visualization and analysis of such data are difficult tasks. A 2D movie is generally understandable while 3D movies need more efforts. Also, huge amounts of data produced by these techniques as well as the complexity of observed behaviors require more automated analysis and modeling to grasp (Driscoll and Danuser (2015)). From the point of view of experimental procedure, manipulation of three-dimensional environments and cell culture is still challenging. Moreover, microscopy techniques created and improved for 2D substrates, like traction force microscopy (Holenstein et al. (2019)) or drug testing (Langhans (2018)) are still in early development in 3D. Mechanisms brought to light by 2D imaging (blebs, lamellipodia) are still reported in complex 3D environments (Blaser et al. (2006), Petrie and Yamada (2012)) and addessing non-trivial substrate topologies doesn't require full 3D matrices (Pieuchot et al. (2018), Kim et al. (2009)). Finally, significant part of animal organs and tissues are composed of folded two dimensional sheets of cells. Analyzing cell migration on two dimensional substrates is still valid. Most of the later discussed results including ours come from this type of experiments.

1.4 Patterns of Edge Activity in Actin Based Motility

Edge activity is characterized by various patterns of protrusion and retraction. Non-motile cells produce transient lamellipodia that form, extend and retract spontaneously in an oscillating pattern. Although it induces great shape changes, oscillating edge activity does not produce any cell displacement and leaves the cell isotropic on average. Organization of protrusion-retraction patterns eventually leads to the formation of a constantly protruding leading edge and retracting trailing edge. As a result, cells break their initial circular symmetry and develop a persistent front-back axis that allows them to migrate. Transition from an immobile to a motile phenotype is called *polarization*.

Prior to polarization, transient lamellipodia form in a seemingly random fashion. Moreover, prospective front and back of the moving cell are not distinguishable before the onset of directional motion. Polarization and persistent motion emerge from seemingly random

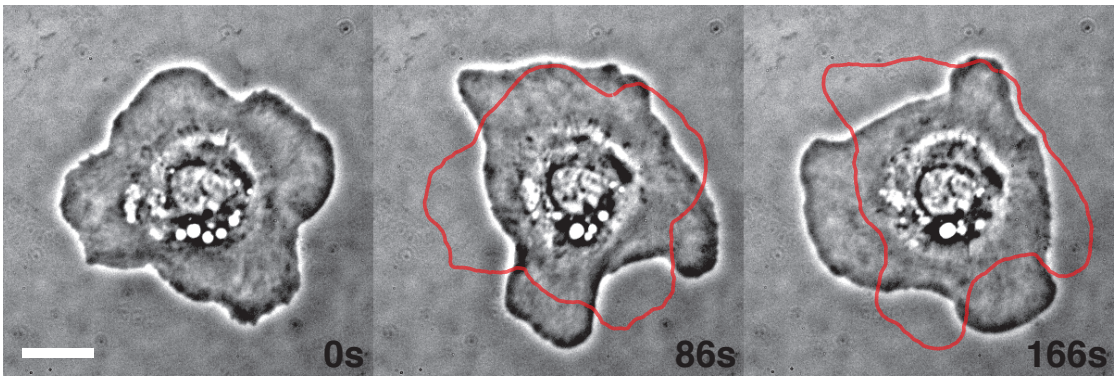

Figure 1.9 – Polarizing keratocyte. Time (in seconds) elapsed since the first snapshot shown at the bottom of each frame. Outline of the previous snapshot shown in red. Images are cropped from $133 \times 133 \mu m$ pictures. The region of interest is the same for the three snapshots to show there is no net displacement of the cell. Scale bar $20 \mu m$.

patterns. The processes that coordinate edge activity and orchestrate polarization still remain unclear (Verkhovsky (2015), Mogilner et al. (2012), Machacek and Danuser (2006)).

Polarization could happen in response to external chemical or mechanical cues but can also happen spontaneously (Verkhovsky (2015), Mogilner et al. (2012)). Polarization in response to attractive stimuli usually happens by forming protrusion at the prospective front of the cell (Parent (2004)). However, spontaneous polarization is believed to be initiated by retraction at the prospective cell rear (Mseka and Cramer (2011), Yam et al. (2007), Barnhart et al. (2015)). Recently, it has been reported that polarization in response to repellent also happens by retraction at the rear (Cramer et al. (2018)).

In non-polarized state, seemingly random protrusion-retraction behavior is observed in various types of cells, e.g. fibroblasts exploring their environment (Bear et al. (2002), Giannone et al. (2004), Machacek and Danuser (2006)) and dictyostelium in absence of chemical attractant (Arai et al. (2010)). One of the striking examples is the epidermal fish keratocyte (which is model system used in our studies) which exhibits large lamellipodial protrusions (Fig. 1.9). Spreading keratocytes display multiple lamellipodia holding 1/3 to 1/4 of the edge circumference. Generally, protrusions grow normal to the cell edge and retract toward the center of the cell in a movement reminiscent of breathing. The cycles can be asynchronous or propagate in a wave-like manner along the cell outline. More exotic rotating phenotypes can occur when several leading edges stabilize in two- or three-fold symmetric configuration (Fig. 1.11).

In contrast, polarized keratocytes display stable, fast and persistent motility with nearly constant shape (Fig. 1.10). Cells typically form a large crescent shaped lamellipodium at their front. Their body forms a v-shape trailing edge at their back. Cell speed is typically in the range of $10 \mu m/$ min (Wilson et al. (2010)) which means cells travel distances equivalent to their size in about a minute. The change of shape and behavior before and after polarization is drastic (Figure 1.12). Occasionally, keratocytes could display reversible switch between directional

motility and oscillatory activity (based on our own unpublished observations).

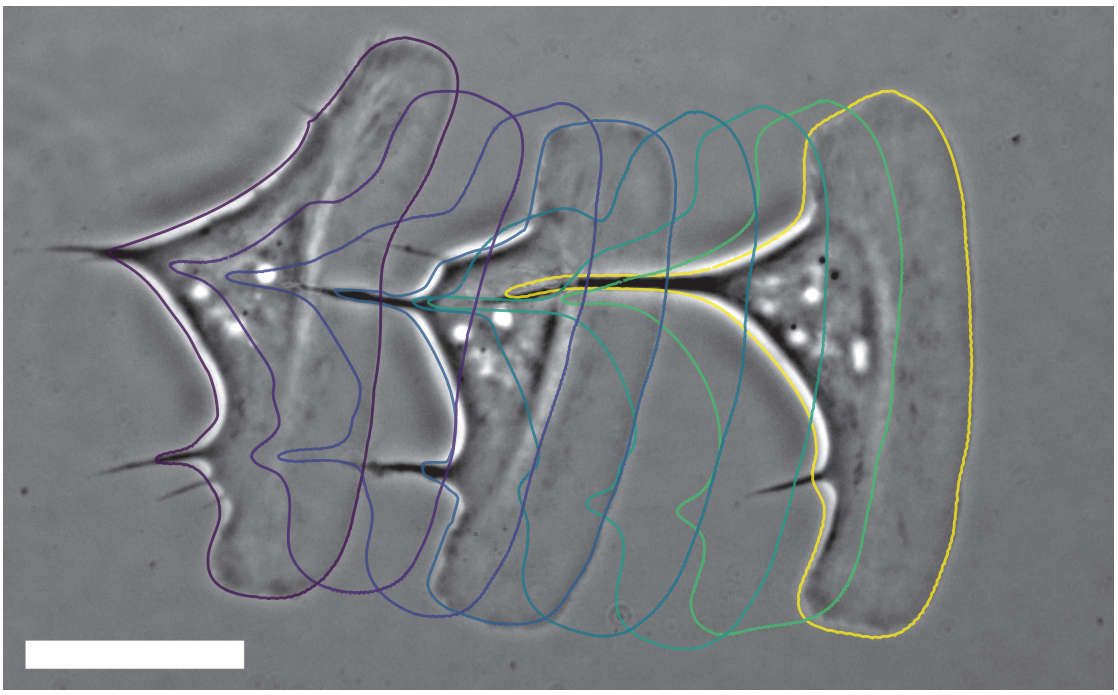

Figure 1.10 – Migrating keratocyte. There is a 40s time shift between every outline. Scale bar 20μm.

1.5 Mechnanisms of Cytoskeletal Activity and Cell Polarization

Motile machinery generates various patterns of edge activity. Organization and interactions between its biochemical components have been extensively described. However, connection between molecular constituents and behaviors observed at the cellular level remains unclear. A variety of models have emerged to explain cell polarization, patterns of cell edge activity and motility. Models generally rely on feedback mechanisms involving signaling networks and feedback mechanisms at the level of the cytoskeleton itself. Models consider self-sorting of signaling molecules, feedback between actin assembly and nucleation promoting factors (NPF), membrane shape and tension, actin flow and the cell-substrate coupling or mechanisms implying multiple sources.

Signaling networks

Self-organization of signaling molecules like Rho family GTPases and phosphoinositide lipids have been witnessed experimentally in polarizing and migrating cells following cues (Weiner et al. (2002), Wong et al. (2006)) and even in the absence of chemical attractant (chemoattractant) (Arai et al. (2010)). Molecules promoting actin polymerization like Rac or PIP_3 localize at the cell front and agents promoting contraction, Rho and myosin II are found in the back

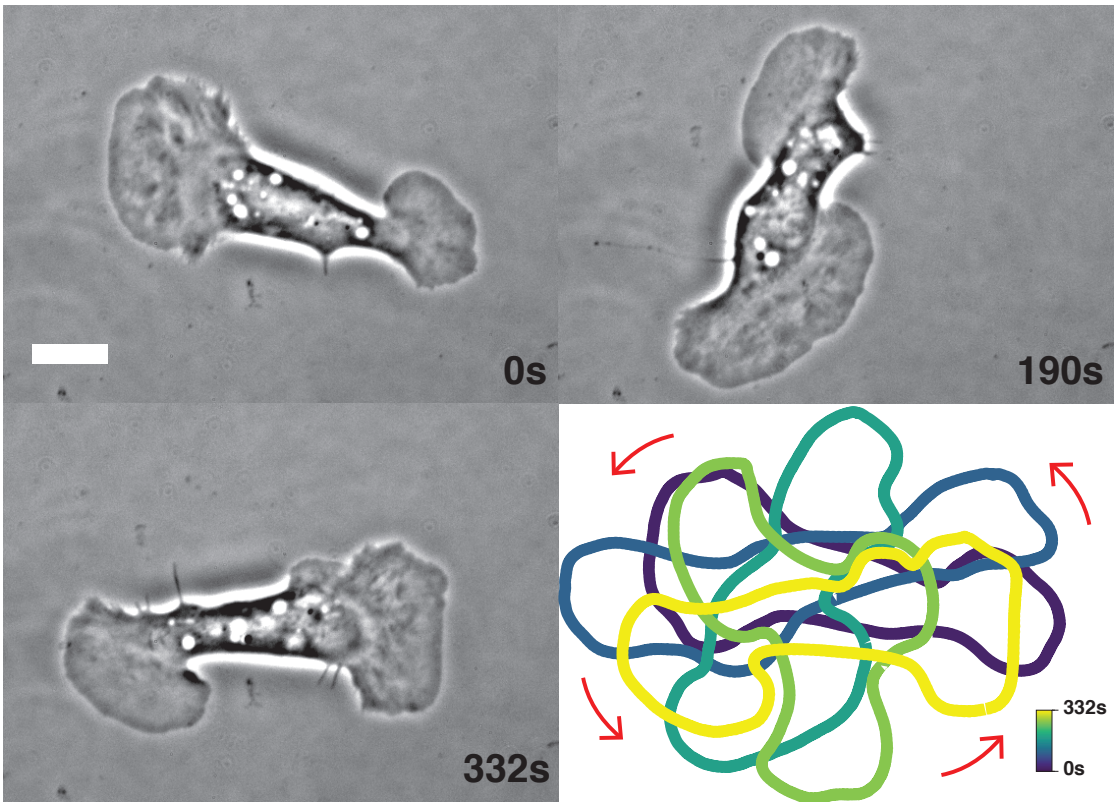

Figure 1.11 – Rotating keratocyte. Time (in seconds) elapsed since the first snapshot shown at the bottom of each frame. Images are cropped from $133 \times 133 \mu m$ pictures. The region of interest is the same for the three snapshots to show there is no net displacement of the cell. Scale bar $20 \mu m$.

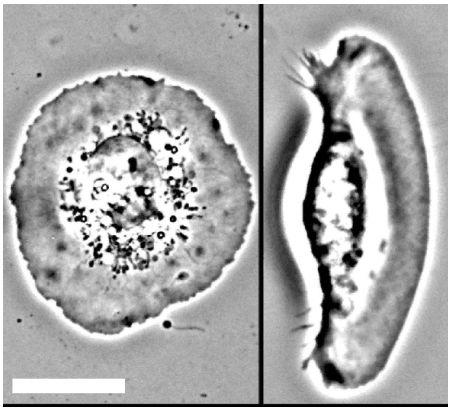

Figure 1.12 – Unpolarized (left) and polarized (right) fish epidermal keratocytes. Scale bar $20 \mu m$

(Narang (2006)). Models explaining self-sorting of chemical species date back to the works of Alan Turing (Turing (1952)). They rely activator-inhibitor substances with different diffusivity involved in coupled chemical reactions. The cornerstone of these models is to have

local self-enhancing activators and a global diffusive inhibitors. Many variations including different number of chemical species and types of reactions have been proposed (Jilkine and Edelstein-Keshet (2011)).

Actin Assembly

Formation of propagating actin waves has been observed in many different types of cells (Alt et al. (1995), Vicker (2002)). These waves correlate with protrusion and retraction of the cell-edge and localize at the leading edge of migrating cells. They also coincide with concentration waves of molecules involved in promotion of actin polymerization. In a seminal article, waves of membrane bound Hem-1, a component of the protein complex activating Arp2/3, followed by actin waves have been observed in Neutrophils (Weiner et al. (2007)). Waves initiate inside the cell and propagate outwards. Advance of the leading edge is strongly correlated with underlying waves. A distinct refractory region between wavefronts and the fact that colliding waves annihilated each-other indicated that actin inhibits Hem-1 and is required for wave formation indicating a *negative feedback loop* involving polymerization activator Hem-1 and filamentous actin (see Fig. 1.13 a). Freezing of Hem-1 waves and dramatic increase of lifetime membrane-associated Hem-1 in cells treated with depolymerizing drug latrunculin (that dirsupts actin filaments) confirmed negative feedback mechanism. Moreover, photobleaching assays determined that Hem-1 is recruited adjacent to existing membrane-bound Hem-1. Authors proposed that the system follows the dynamics of an *excitable medium*. Similar to action potential firing mechanism in neurons, excitable media (or systems) are support to propagating waves that undergo a refractory period after the passage of a wave in which no wave can pass for a certain amount of time. The heuristic model proposed by the authors is the following. Hem-1 has autocatalytic properties. It stimulates its own rectruitment and actin polymerization. Actin transiently inhibits Hem-1 and is finally broken down with its own depletion mechanism allowing Hem-1 to be recruited again. Mathematical simulations of this model reproduced, Hem-1 and actin waves with characteristic gap between waves, annihilation of colliding waves and freezing of the waves upon when actin polymerization is cut. Theoretical modeling of the phenomenon was proposed in Doubrovinski and Kruse (2008).

Similar mechanisms with autocatalytic actin activator and negative feedback of actin polymer generating actin waves have been discovered in other organisms (Allard and Mogilner (2013)). Theoretical models for spontaneous actin waves coinciding PIP_3 (Gerhardt et al. (2014)) or Arp2/3 (Ryan et al. (2012), Millius et al. (2009)) have been proposed. Actin was also reported to feed back on its own assembly without intervention of signaling molecules (Bretschneider et al. (2009)). Theoretical models for this type of mechanisms involve a diffusive activator that interacts with actin possibly involving other steps. They resemble "Turing-like" models but without a fast-diffusing global inhibitor. For example, authors of Ryan et al. (2012) proposed a one dimensional model for the concentration of filamentous actin along the leading edge. It features a diffusive self-recruiting activator A that generates free barbed ends B on which F-actin F can bind. Recruitment of the activator drops as actin reaches a critical

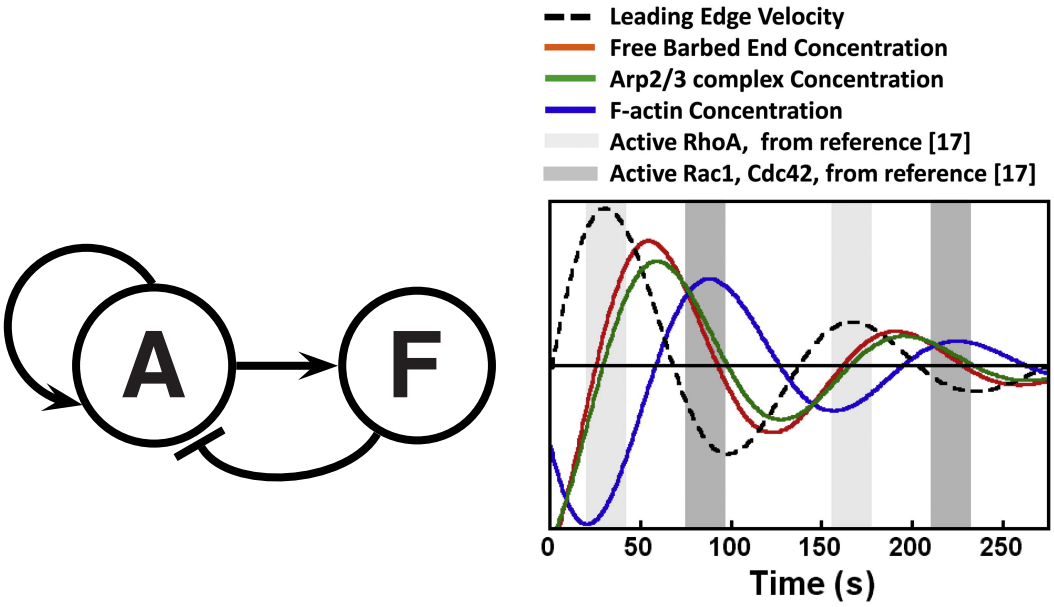

Figure 1.13 – (a) Sketch of a negative feedback mechanism, Activator A promotes itself and assembly of F which in turn inhibits A. (b) Timing of leading edge velocity and concentration wave patterns. Curves for F-actin and free barbed ends are simulated from the model found in Ryan et al. (2012). Velocity of the leading edge and Arp2/3 behavior come from experimental measurements. RhoA, Rac1 and Cdc42 come from Ji et al. (2008)

concentration F_S. Free barbed ends and actin both disassemble spontaneously. Equations governing the concentrations read

$$\partial_t A = (\rho_0 + \rho_2 A^2) e^{F/F_s} - k_A^- + D_A \nabla^2 A + \sigma \tag{1.3}$$

$$\partial_t B = k_B^+ A - k_B^- B \tag{1.4}$$

$$\partial_t F = k_F^+ B - k_F^- F \tag{1.5}$$

First term on the right hand side of equation 1.3 is the quadratic recruitment damped over a certain F-actin concentration, σ is a white noise. Simulation of this model produced oscillating patterns of spikes of actin (F) and free barbed ends (B) along the edge. Authors compared these results to wave patterns of Arp2/3 and actin in Xenopus cells and found similar correlations. Compiling results from the model for F-actin and free barbed end concentration with experimental measurements and results from the literature, they derived temporal coordination of promoting factors and F-actin concentrations spikes with velocity of the leading edge (Fig. 1.13 b).

Another way to model actin assembly is using a phase-field approach. For example, the model introduced in Dreher et al. (2014) generated spontaneous generation of complex patterns and cell polarization. Its basic ingredients are actin and NPFs interacting which interact in a negative feedback loop. NPFs promote nucleation of actin filaments which in turn inactivates NPFs. The cytoskeleton is considered to adhere tightly to the substrate. There is no

actin flux relative to substrate and molecular motors are absent. This model produces a variety of complex phenotypes. In addition to stable directed motility, unstable motion in which cells discontinuously change direction and spiral motion have been observed. Moreover, stationary states with appearing and vanishing blebs similar to protrusion retraction cycles occur.
Models based on feedback in actin polymerization are generally limited due to the fact that they do not consider many other mechanisms, e.g. molecular motors and adhesions. Even if cells display actin polymerization waves corresponding to edge activity, modulation of adhesion and cell contractility strongly affects protrusion-retraction cycles (Yam et al. (2007)), polarization (Barnhart et al. (2015)) and physical integrity during migration (Cai et al. (2010)) showing that they are an integral part of mediation of edge activity.

Membrane Shape and Tension

Cytoskeletal activity is a very important factor for generating shape and tension in the plasma membrane (PM). Interaction with the cytoskeleton and other associated proteins provides its shape. The cell membrane is not an ideal smooth surface. It is covered with folds, wrinkles and small protrusions sustained by actin (Gauthier et al. (2012)). On a larger scale, lamellipodia, or other protrusions fueled by actin polymerization, yield positive curvature (convexity) to the cell edge while retracting edge portions have negative curvature (concavity) (Fig. 1.12 right and 1.1 c). The membrane is also dynamic. The lipid bilayer is not elastic, it can stretch elastically until a 2 to 3% in area beyond which it breaks[5] (Morris and Homann (2001)). To prevent this, folds and wrinkles can be depleted to fulfill area requirements. On a longer time scale, membrane tension can be modulated via membrane trafficking. Increase in tension activates exocytosis (fusing of vesicles with the plasma membrane) and slows down endocytosis (vesicle formation), and the opposite for a tension decrease (Gauthier et al. (2012)). Conversely, tension in the membrane also depends on the cytoskeleton, impairing actin polymerization and myosinII activity causes drops in membrane tension (Lieber et al. (2013)).

The shape of the cell membrane could be involved in diverse mechanisms controlling edge activity. Membrane-bending proteins (e.g. BAR proteins) might be attracted by local membrane curvature due to actin protrusion (Mim and Unger (2012)). These membrane proteins recruit nucleation promoting factor thus forming a positive feedback loop (Suetsugu and Gautreau (2012)). Theoretical model of the cell membrane deploying this kind of mechanism was sufficient to produce oscillations (Peleg et al. (2011)). Interestingly, curvature sensing proteins interacting with actin filaments could also contribute to the flatness of the lamellipodium (Schmeiser and Winkler (2015)).

It has been shown experimentally that protrusion rate in the lamellipodium is very sensitive to external load and can be stalled even by small forces (Prass et al. (2006), Bohnet et al. (2006)). Interestingly, protrusion rate and actin density are similarly graded along the cell's leading edge. They are highest in the middle and go down towards the sides (Keren

[5] Notable anomaly, the red blood cells can undergo massive shape changes thanks to the absence of nucleus and special composition of their membrane.

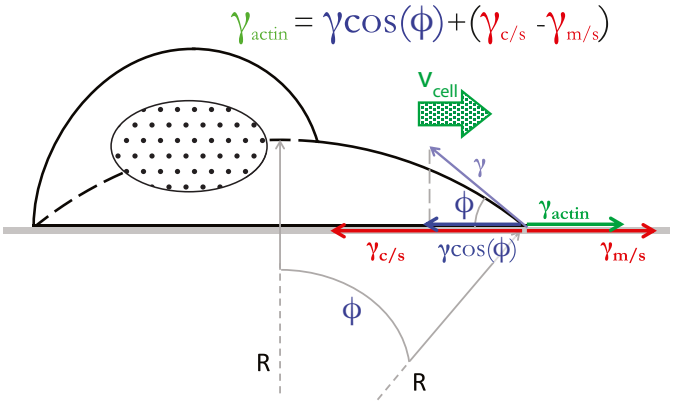

Figure 1.14 – Edge of a migrating cell can be considered a triple interface. Actin polymerization yields a force γ_{actin} at the leading edge in the direction of motion. On top of that, the three phases seek to minimize their surface of contact. This yields three forces: medium-substrate tension $\gamma_{m/s}$ in the direction of motion, cell-substrate tension $\gamma_{c/s}$ opposite to motion, and cell-medium tension γ along the cell membrane. Force balance in the plane of motion involves the contact angle at the leading edge ϕ. Considering the interfacial tensions depend on the composition of the phases they can taken as constant. Thus force balance is determined by protrusive forces and contact angle.

et al. (2008)). Assuming that membrane load is uniformly distributed among actin filaments, the load on single actin filaments is proportional to actin density. This explains why regions of lower actin density exhibit lower protusion rate. It has been proposed that actin density, protrusion rate and membrane shape could be integrated in a feedback loop. Shape depends on the protrusion rate and therefore on actin density, but actin density depends on shape because shape influences lateral drift of actin filament ends along the edge. This drift depletes filaments from the lateral sides of the leading edge, eventually generating graded actin distribution (Grimm et al. (2003), Adler and Givli (2013)). However, these models only describe already polarized and moving cells. They do not address the question of initial symmetry breaking. Another fully mechanical model based on feedback between actin polymerization and membrane tension described competition between two opposite sides of the cell resulting in one side winning and becoming permanent leading edge (Wang and Carlsson (2014)).

Tri-dimensional geometry of the leading edge could also play a role in the load exerted on polymerizing actin. When cells are plated on a flat surface interaction between cell membrane, substrate and culture medium could be understood in terms of a triple interface, a physical concept that describes the force balance at the edge of liquid droplets (Fig. 1.14). Following this framework, load on polymerizing actin should depend on the contact angle between the cell and the substrate at the leading edge. This was tested by experimentally swelling and flattening cells by changing the osmolarity of the medium and measuring their velocity (Gabella et al. (2014)). Swollen and flattened cells displayed higher, respectively lower speed than control cells. It was proposed that extension of the lamellipodium flattens the contact angle and increases the resistance to actin polymerization.

Feedback from Motion

The idea of a feedback mechanism based on motion was originally proposed in Verkhovsky et al. (1999). In this study, polarization of keratocyte cytoplasmic fragments were analyzed. Previously stationary cytoplasmic fragments were induced to move by a mechanical stimulus (stream of medium expelled from a micropipette positioned near the fragment edge). Fragments rapidly acquired crescent shape characteristic of migrating keratocytes and most fragments continued to move after withdrawal of the stimulus. Interestingly, polarized organization of the cytoskeleton did not arise immediately. Initially, pushed fragments generally retained typical cytoskeletal organization of stationary fragments with uniform distribution of actin and myosin II. But after the fragment moved approximately one length of its body, distribution of actin and myosin II became similar to locomoting fragments: actin at the front and myosin at the back. At this stage, actin organization also displayed distinctive features of migrating cells: brushlike network at the leading edge, gradual realignment of filaments along the front-back axis and bundles along the trailing edge. Authors proposed that motion favors polarity. As the cell moves, myosin II is transported towards the back of the cell by actin retrograde flow and accumulates at the cell rear. Increased concentration of myosin II favors continuous contraction at the back thus sustaining cell polarity. Incidentally, any factor promoting contraction or inhibiting polymerization transported by actin flow would reinforce cell polarity and persistence of motion. Since then, several theoretical models relying on feedback from motion were proposed (Du et al. (2012), Ziebert et al. (2012), Shao et al. (2012), Nishimura et al. (2009), Barnhart et al. (2015), Ruprecht et al. (2015)).

Experimental evidence for a feedback mechanism between motion and cell polarity mediated by actin flow was recently provided (Maiuri et al. (2015)). Authors observed a coupling between speed and persistence of motion over a wide range of cell types. Looking for the origin of this coupling, they studied influence of retrograde flow on migratory persistence of cells independently of the cell speed and observed that mean persistence time τ of cells in every tested experimental conditions was strongly correlated with the flow speed (in the reference frame of the moving cell) and could be fitted with an exponential

$$\tau = Ae^{\lambda V} \tag{1.6}$$

where $V > 0$ is the retrograde flow rate, while no correlation was found with the cell speed. Thus retrograde flow underlies the coupling. Authors proposed that actin flow drive asymmetry in the concentration of so-called *polarizing cue* which in turn provides persistence in motion. A polarizing cue could be for example an actin polymerization activator like Cdc42 or a molecular motor. This hypothesis was tested jointly with physical modeling and experiments. The model is one dimensional and features a molecule that can bind actin (binding rates k_{on}, k_{off}) and thus be advected by the flow (flow speed $-V$) or diffuse in the cytoplasm (diffusion coefficient D). Concentration dynamics for sufficiently fast binding kinetics read

$$\partial_t c(x,t) - \partial_x \tilde{V} c(x,t) = \tilde{D}\partial_x^2 c(x,t) + \sigma, \tag{1.7}$$

where $\tilde{V} = V k_{on}/(k_{on} + k_{off})$ and $\tilde{D} = k_{off}/(k_{on} + k_{off})$ denote effective coefficients and σ is Gaussian white noise. In the steady state, with constant flow rate, the concentration profile is an exponential which steepness depends on $\tilde{V}$ meaning that actin flow drives the concentration profiles of strong actin binders while leaving unchanged the distribution of molecules having low affinity to actin. This was tested experimentally measuring the distribution of molecules having different affinities to actin in motile cells. Myosin II was identified as a key molecular polarity cue: inhibition of myosin II mediated contractility with blebbistatin[6] led to decorrelation of flow speed and persistence in motion. The metric used to measure persistence is polarization lifetime. It is defined as the time during which the cell has a unique well-polarized lamellipodium.

Motility in Keratocytes : Bridging the Gap

Keratocytes display typical persistent motion with stable shape. Models describing migration in keratocytes generally rely on feedback from motion. Polarization and persistent motility is associated with the establishment and maintenance of gradients: laterally graded actin density and protrusion rate (Grimm et al. (2003), Adler and Givli (2013)) or front-back gradient of polarity factors such as myosin II that are sustained by actin flow (Verkhovsky et al. (1999), Ziebert and Aranson (2013), Maiuri et al. (2015)). However these models rely on already moving cells, strong preexisting asymmetries or very strong spatially and temporally correlated perturbations (Barnhart et al. (2015), Verkhovsky et al. (1999)). They do not address the initial break in symmetry. Moreover, fluctuations of the cells prior to polarization cannot be explained with this type of feedback. In a recent study combining experiments and modeling we proposed a novel unifying mechanism for organization of edge activity in fish epidermal keratocytes (Raynaud et al. (2016)). This model, based on a phenomenological rule in which local cell edge dynamics depend on the distance from the center, explains patterns of edge activity before and after polarization. Implementation of this rule in a stochastic model reproduced spontaneous polarization, persistent motion with stable cell shape and a range of cell-migration behaviors. Success of this model led us to look for a possible mechanism underlying the phenomenological rule. Traction force came as a natural candidate. While traction forces in motile keratocytes had been previously addressed (Oliver et al. (1999), Fournier et al. (2010)), stress exerted by fluctuating cells prior to polarization had not been studied in detail. Therefore, we chose to analyze the role of traction traction forces in cell edge activity during cell polarization. The next chapter describes immediate motivation for our study - the distance-sensing hypothesis.

[6] Blebbistatin is a specific inhibitor of myosin II that prevents ATP hydrolysis

2 The Distance Hypothesis

2.1 Distance Sensing Organizes Cell-Edge Activity

In our recent study combining experiments and modeling (Raynaud et al. (2016)), the shape and edge activity of fluctuating and migrating fish epidermal keratocytes were recorded. Analysis of the protrusion-retraction patterns led to the formulation of a phenomenological rule in which local cell-edge dynamics depend on the distance from the cell center. This principle was tested and validated by stochastic modeling. The model yielded spontaneous polarization, persistent motion and reproduced experimentally observed phenotypes.

Experiments were conducted with fish epidermal keratocytes. Cells were cultured on glass coverslips. Phase contrast microscopy sequences of polarizing and migrating cells were recorded. Their edge was segmented and tracked with high resolution using a tool that had been developed in the group (Ambühl et al. (2012)). In order to characterize edge activity a method was designed to find positions along the cell edge that switched from protrusion to retraction (PR) and from retraction to protrusion (RP). It appeared that switches from protrusion to retraction occurred preferentially at high distances from the cell center. During migration, onset of retraction happened almost exclusively in regions located in the flanks (Fig. 2.1 a). RP switches were also mostly found in the flanks. During spreading, PR switches were found at the tips of protrusions, respectively rotating segments of fluctuating and rotating cells (Fig. 2.1 b, c). In both non-motile phenotypes but most remarkably in rotating cells, switches formed circular patterns. Contrary to migrating cells, RP switches in spreading cells happened distinctively closer to the cell center than PR switches. Calculating the switch distribution as a function of the distance showed the probability to switch from protrusion to retraction grew with the local distance to the cell-center and peaked at highest distances (Fig. 2.1 d).

In migrating cells, regions of most probable switching corresponded at the same time to the maximal cell extension and to the parts of the cell edge displacing in a direction orthogonal to cell motion. Further experiments were performed to show that switches depended really on the distance and not on the orientation of the edge. In one of them, a pipette was placed on the path of a migrating cell. It was positioned slightly above the substrate in order to block the cell body but allowing the flatter lamellipodium to extend below it. In this experiment (further

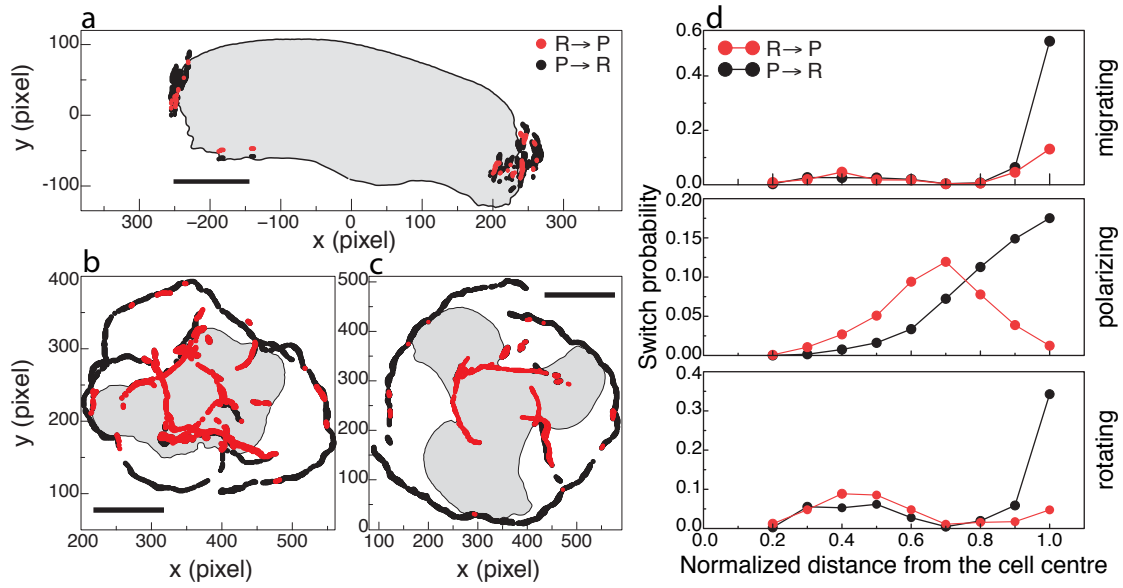

Figure 2.1 – Experimental results. (a-c) Snapshots of migrating (a), polarizing (b) and rotating (c) cells. Switches from protrusion to retraction are shown in black. Switches from retraction to protrusion are shown in red. Cell is depicted in light gray with black outline Scale bar is 6.45μm (migrating and polarizing) and 10.75μm (rotating). (d) Distribution of switches as function of the normalized distance from the cell center for the three corresponding phenotypes. Distances were normalized by the maximum distance from the cell center to aggregate data from cells of different size. Adapted from Raynaud et al. (2016).

pipette or *cell-body-blocking* experiment), the leading edge extended to a distance similar to the cell's maximal lateral extension fluctuated and retracted (Fig. 2.2).

The stochastic model used for validation of the distance rule represents the cell edge as a set of points (or nodes). Each point had two possible states : protrusion or retraction. At each time step, the state of the nodes was updated. A protruding point switched if it reached the maximal threshold distance r_{max}, and the same if a retracting point reached the minimal threshold r_{min}. The state also changed according to the state of the nodes in the neighborhood, like a Voter model. Probability to switch depended on the ratio of neighbors in the opposite state within a certain range of interaction. Altogether, the probability to switch read

$$\mathrm{P}_{P\to R} = \begin{cases} \tau\left(\mathcal{N} + (1-\mathcal{N}(r))\frac{n_i}{N}(r)\right) & \text{if } r < r_{max} \\ \tau & \text{if } r > r_{max} \end{cases} \tag{2.1}$$

$$\mathrm{P}_{R\to P} = \begin{cases} \tau\frac{n_i}{N} & \text{if } r > r_{min} \\ \tau & \text{if } r < r_{min} \end{cases} \tag{2.2}$$

where τ was an overall rate of transition. $\mathcal{N}(r)$ was a normally distributed probability with mean r_{max}. Tuning $\mathcal{N}$ variance allowed for tuning the level of noise in the threshold distance. n_i was the number of neighbors with opposite state and N the total number of neighbors

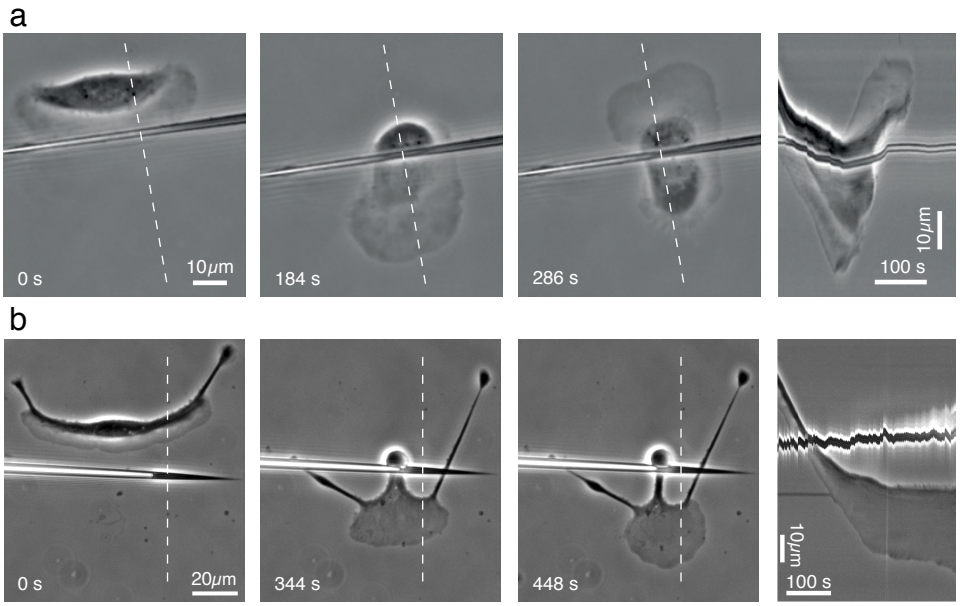

Figure 2.2 – Pipette experiment. A micropipette is held on the path of a migrating keratocyte just above the substrate such that the low leading edge can crawl under it but not the cell body. Last panel on the right is the kimograph of the whole experiment along the dashed line. (a) Control conditions, the leading edge extends until it reaches a distance similar to the cell's maximal lateral extension, fluctuates and retracts, implying a change in the direction of motion. (b) Treated with blebbistatin. Adapted from Raynaud et al. (2016).

within the range of interaction. After update on the states, node positions were incremented. Protruding nodes moved outward normally to the edge and retracting nodes moved towards the center. Finally, position of the cell center for next step was computed (for details see Raynaud et al. (2016)).

Simulations of the model produced spontaneous polarization of the system and persistent directional motion with stable shape from random initial node state and circular shape (Fig. 2.3 a, b). It also successfully reproduced the experimental distribution of switches as a function of the distance. Finally, simulations yielded stable rotating phenotypes (Fig. 2.3 c) and the pipette experiment was reproduced. The phenomenological distance-sensing property is sufficient to explain observed edge dynamics.

Other mechanisms of shape feedback were tested. The distance rule was replaced by a switching probability depending on cell area or overall ratio of protruding versus retracting points. But these alternative mechanisms did not lead to stable shape nor directional motion. A target area or a ratio impacts all nodes at once whereas distance-sensing affects edge dynamics locally. It relates overall cell behavior to local protrusion-retraction dynamics before and after polarization.

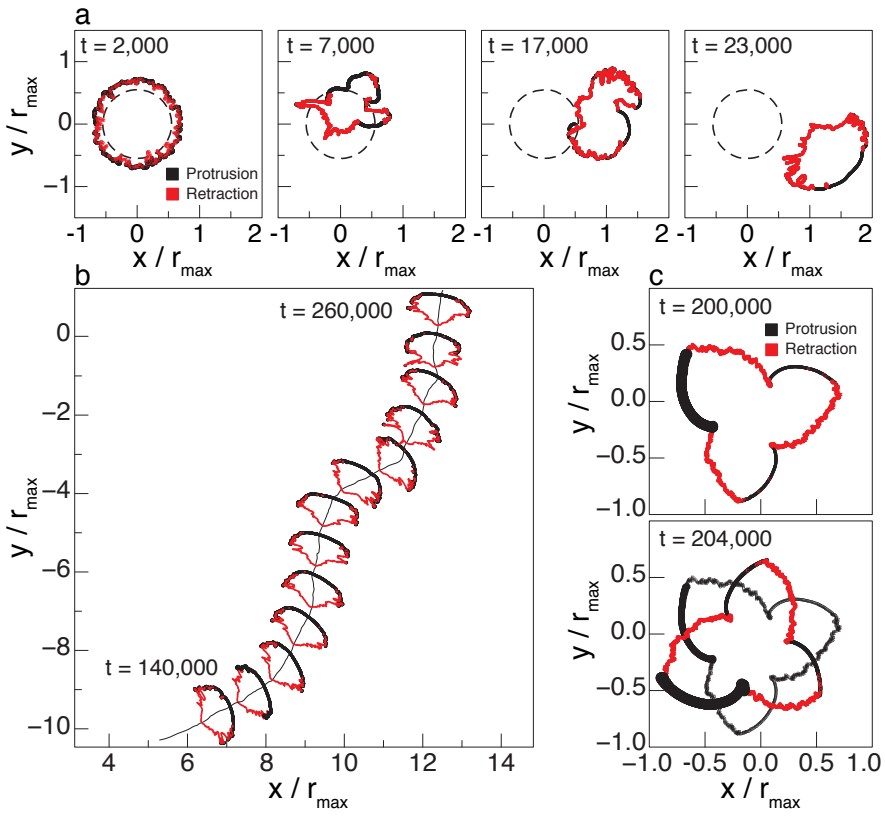

Figure 2.3 – Results of model simulations. Successive edge configurations during migration (a), migration (b, snapshots every 20000 time steps) and rotating phenotype (c). Protruding nodes are marked in black, retracting in red. (c) One of the lobes has thicker stroke to facilitate comparison of the two snapshots. Adapted from Raynaud et al. (2016).

2.2 Looking For an Underlying Mechanism

Success of the phenomenological distance rule suggests that cells might be capable of distance-sensing. We started looking for the mechanism underlying this property. Majority of models describing cell polarization and migration rely on the establishment of gradients in the direction of motion (Barnhart et al. (2015), Maiuri et al. (2015), Ziebert et al. (2012)). Moreover, in these models polarization often requires artificial addition of strong inhomogeneities (Barnhart et al. (2015)) or external stimuli (Narang (2006)). In our model, there is no initial cue, the distance rule is isotropic and organization of the cell-edge dynamics leading to polarization is spontaneous. Once directional motion is established, a gradient of switch probability arises. However, this gradient is not directed in the direction of motion as it is in many models for cell migration but rather oriented radially from the center to the edge of the cell. This does of course not exclude the formation of front-back gradients and regulatory processes that stabilize the cell motion (Maiuri et al. (2015)).

Several mechanisms are used in nature for distance sensing. For example, arthropod

embryo segmentation relies on a mechanism based on diffusible transcription factors that are expressed at one end of the organism. Each compartment is defined by a concentration of the different factors and allows for very precise compartmentalization (Myasnikova et al. (2001)). Likewise, gradient of protrusion promoting factors diffusing from the center of the cell could contribute to distance sensing. However, it is not known what these factors could be. Another component implicated in cell size control are microtubules (Martin (2009), Picone et al. (2010)). However, in our experiments, disassembly of microtubules did not affect cell size and edge dynamics (Raynaud et al. (2016)). Alternatively, switch to retraction could happen if retrograde flow rate increases with distance and eventually overcomes actin polymerization. Flow rate could be expected to scale with the size of the system, e.g. if retrograde flow is powered by contraction of multiple units connected in series. Another natural candidate for protrusion-retraction switch is traction force that could detach adhesions at the cell-edge thus initiating retraction. Interestingly, distance sensing is impaired by inhibition of cell contractility. Inhibiting myosin II contractility with blebbistatin increased cell maximal extension. Cell behavior in cell-body-blocking experiments changed. Cells extended their leading edge away from their body to which they remained attached by narrow stalks (Fig. 2.2 b) but did not reverse their motion like in control conditions. This result indicates the importance of myosin II contractility in controlling cell motility and preserving shape integrity (Cai et al. (2010), Raynaud et al. (2016)).

However, if traction forces play a role in distance sensing, their magnitude should scale with distance. Recently, several studies investigated the relationship between cell geometry and traction forces (Álvarez-González et al. (2015), Burnette et al. (2014), Fouchard et al. (2014)). Traction forces have been reported to correlate with static parameters such as cell area and local in-plane curvature of the edge or maximal extention (Oakes et al. (2014), Rape et al. (2011)). Magnitude of forces depends also on the stage in the cell cycle (Vianay et al. (2018)). In a study where traction forces were reconstructed from the patterns of actin retrograde flow, stress was found to increase during protrusion and reach maximum after the switch from protrusion to retraction but the forces were not measured directly (Ji et al. (2008)). In contrast, another study reported that forces drop prior to retraction (Barnhart et al. (2015)). Thus, precise coordination of traction forces and edge dynamics is still not well understood.

Methods Part II

3 Traction Force Microscopy

The idea of using soft and deformable substrates in order to visualise forces exerted by cells emerged in the early 1980s. The first attempts to visualize forces exerted by cells were performed on thin sheets of silicone rubber (Harris et al. (1980)). Cells growing on these substrates would deform them creating wrinkles visible under microscope (Fig. 3.1). This approach did not give any quantitative measure on the traction cells exerted on the substrate. Also, the location of large forces was not precise because wrinkles appeared *between* high tension sites. However, the general direction of the stress could be determined, the waves in the wrinkle patterns being perpendicular to it. The order of magnitude of the shear forces was measured with glass microneedles calibrated with paperweights, pushing on the substrate *until this surface is distorted to the same degree as it is by cells.*

Since then, new techniques have been developed. Modern ways of measuring traction forces now include deformable cell substrates that allow for quantitative and local measurment of the stress like micropillar arrays (Tan et al. (2003)) and, the method used in this work, tracking of the displacement of markers embedded in a thick substrate. The technique is called *traction force microscopy* (TFM). Another very promising method makes use of FRET sensors that allow both high accuracy and the possibility to create intracellular force sensors (Grashoff et al. (2010)).

In the present case, the deformable substrate is a polyacrylamide gel coated with extracellular matrix proteins and markers are fluorescent latex beads. The deformations caused by the stress exerted by the cell can be retrieved tracking the displacement of the embedded fluorescent beads. The following sections will describe its working principle, the protocols to follow to conduct such an experiment and the different experimental conditions. Simpler experiments, e.g. interference reflection microscopy (IRM) and fluorescent speckle microscopy (FSM), will be described at the end of the chapter.

Due to non-reducible incubation times, such an experiment takes 3 days to carry out, one for creating the gel, a second for transferring the cells and a third for acquiring image sequences. Also, implementation of the protocol is difficult, the two first steps in particular: gel preparation and transfer of the cells. There is a high chance that some of the attempts will fail. Thus we strongly advise to conduct a few experiments in parallel. During this study, we

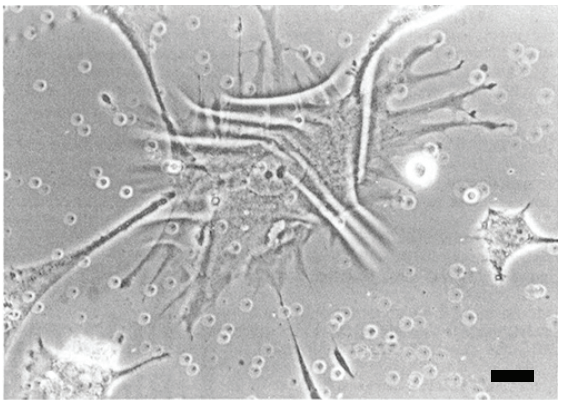

Figure 3.1 – Micrograph of wrinkles created by a fibroblast when plated on a silicone rubber substrate. Scalebar 10 μm. Taken from Harris et al. (1980)

always prepared at least 6 gels at a time.

3.1 Gel Preparation

The protocol for for the preparation of Polyacrylamide gels with tunable elastic modulus embedded fluorescent marker beads was elaborated by Alicia Bornert and broadly inspired by Tse and Engler (2010) and Plotnikov et al. (2014).

Material

- Deionised and distilled water
- 0.1M NaOH
- 3-Aminopropyltrimethoxysilane (3-APTMS) (Cat#281778, Sigma-Aldrich)
- Phosphate-buffered saline (PBS)
- 0.5% v/v glutaraldehyde (Cat#G5882, Sigma-Aldrich) in PBS
- 10% v/v SurfaSil (Cat#42800, PIERCE) in chloroform
- Rain-X (ITW Global Brands, available at hardware stores)
- 70% ethanol

- FluoSpheres (Cat#F8810, Invitrogen)
- Ammonium persulfate (APS) (Cat#A3678, Sigma-Aldrich)
- 40% Acrylamide (Cat#A1089, AppliChem)

- 2.5% Bis-Acrylamide (Cat#A4989, AppliChem)
- Tetramethylethylenediamine (TEMED) (Cat#A1148, AppliChem)
- Sulfo-SANPAH (Cat#22589, Thermo Scientific)
- Fibronectin (Cat#F0895, Sigma-Aldrich)

Equipment

- Nitrile gloves
- KimWipe tissues
- 25mm circular coverslips (1 per gel)
- Microscope slides (2 per gel)
- 6-well plate
- Glass pipette
- Glass Petri dish
- 35mm punched petri dish
- Parafilm
- Vacuum desiccator
- Vortex mixer
- Fume hood
- Oven
- Sprayer bottle (Cat#0343812A, Fisher Scientific)
- Ultraviolet lamp

Protocol

Coverslips Activation Place the 25mm coverslips into a glass petri dish and apply 400μL of 0.1 M NaOH for 5 min at room temperature (RT) making sure a maximal area of the glass surface is covered. Aspire the NaOH, place the coverslips under the fume hood. Using a glass pipette, apply 500μL of 3-APTMS for 10 min. Use imperatively nitrile gloves for this step. Rinse multiple times with ddH_2O, dry coverslips in oven at 37°C for 10 min and cool at RT. Transfer the coverslips to a 6-well plate, pipette 200μL 0.5% v/v glutaraldehyde on each coverslipand incubate at RT for 20 min. Rinse multiple times with distilled water and let dry at room temperature.

Activated coverslips were always freshly made on the same day the gels were prepared. However, according to Plotnikov et al. (2014) they can be stored for at least 2 weeks in a vacuum desiccator.

Hydrophobic slides Coat microscope slides (2 for each gel) with Rain-X using a KimWipe tissue. Let dry for 10 min at RT. Rinse thoroughly with deionised water and then several times with ethanol.

Hydrophobically treated slides can be stored in a vacuum desiccator for several months. Another technique using chlorinated silane is described in Tse and Engler (2010).

Gel Preparation Prepare 10% solution of APS in ddH_2O (10% APS solution can be stored at $-20^{\circ}C$ for a month). Prepare $5mL$ of working solution with proportions for the desired elastic modulus (See table 3.1). Pipette $200\mu L$ of working solution in 2 eppendorfs, one for each gel layer.

[1^{st} layer:] Add $300\mu L$ of distilled water in one of the eppendorf. Polymerize the solution by adding $0.75\mu L$ TEMED and $2.5\mu L$ APS. Quickly vortex and pipette $10\mu L$ of the solution onto a hydrophobically treated slide. Place a 25mm coverslip on top (treated side down) and allow 20-30 minutes to polymerize at RT.

[2^{nd} layer:] Add $290\mu L$ of distilled water and $7.5\mu L$ fluorescent beads to the second eppendorf. Vortex the fluorescent beads before pipetting. Peel off slowly the coverslip from the slide, a razor blade can be used to detach the coverslip from the slide. Put the coverslip treated face up in a petri dish and moisten the gel by spraying PBS horizontally above it with a sprayer bottle. Polymerize the acrylamide solution by adding $0.75\mu L$ TEMED and $2.5\mu L$ APS. Vortex quickly and pipette $5\mu L$ of the solution onto a hydrophobically treated slide. Place the coverslip on top (layered side down) and allow 20-30 minutes to polymerize at RT. Peel off the coverslip gently and immerse it in PBS.

After addition of the catalysts (TEMED, APS) to the working solution, pipetting and placing the coverslip must be performed rapidly to avoid premature gel polymerization. The status of polymerization can be monitored looking at leftover solution in the eppendorf, when the gel is polymerized in the eppendorf, the coverslip is ready to be detached. One must be extremely cautious when detaching the coverslip from the slide. There is a high chance of breaking during this phase.

ECM Coating Prepare fresh $1mg/mL$ Sulfo-SANPAH in ddH_{20}. Prepare $10\mu g/mL$ fibronectin in PBS. Aspire PBS around the gel, avoid drying the gel. Pipette $0.5mL$ Sulfo-SANPAH solution onto the gel surface. Put the gel at 7-8cm under the UV light and irradiate for 10 minutes. Wash the gel with PBS several times. Pipette $200\mu L$ of fibronectin solution. Incubate at $4^{\circ}C$ overnight. Wash several times with PBS. Keep the gels immerse in PBS before use.

Transfer to Dish Just before transferring the cells, take the coverslip out of PBS, dry the face not coated with gel and stick the coverslip onto a punched 35mm petri dish with DC4, a waterproofing silicone compound (this way punched petri dishes can be reused).

Table 3.1 – Working solution for gel preparation. Quantities are given for $5mL$. Reproduced from Tse and Engler (2010)

Modulus [kPa]	40% Acrylamide [mL]	2.5% Bis-Acrylamide [mL]	Water [mL]
1.67 ± 0.14	0.937	1.125	2.938
4.47 ± 1.19	1.560	0.750	2.690
16.7	3.125	0.750	1.125

3.2 Cells Transfer and Culture

Different types of cells have to be taken care of in distinct ways. Epidermal keratocytes unlike other widely used cell types do not proliferate in culture. For all experiments in this study (also IRM and FSM), keratocytes were cultures by extracting scales from living or recently sacrificed fish with tweezers and sticking it onto a coverslip. Fishes were black tetra (*Gymnocorymbus ternetzi*) from 3 months to 2 years old; male and female were used indifferently. The were kept in a fish tank in the lab. Work with fishes was performed according to the protocol approved in animal work license number 2505 from the Swiss Veterinary Office.

The most common cause of failure of such operation was the detachment of the scale upon culture medium addition. To prevent such unwanted events, scales were allowed 30 to 60 seconds to adhere while the excess water was removed with a KimWipe. Medium was then added cautiously to the dish wetting gently the scale. The culture medium was DMEM with HEPES modification and high glucose from Sigma-Aldrich (Cat#D1152) supplemented with 20% of foetal bovine serum (FBS), fungizone (Ampotericin B 250 $\mu g/mL$, Thermo Fisher, Cat#15290018), gentamicin (Thermo Fisher, Cat#15750060) and penicillin-streptomycin (100 units/mL, Thermo-Fisher, Cat#15140122). Finally cells were incubated overnight at 30°. The cells would migrate away from the scale forming a colony.

Cells were then isolated treating colonies with EDTA (85% PBS and 2.5 mM EDTA (Cat#E9884 Sigma-Aldrich), pH 7.4) for a few minutes until cells were visually separated. Medium was then washed and the petri dish was replenished with fresh medium for observation.

3.3 Experimental Conditions

TFM experiments were conducted with three different substrate rigidities, namely $1.67kPa$, $4.47kPa$ and $16.7kPa$. For experiments not requiring stress measurements (IRM, FSM), cells were plated on glass. As cells tended to move more and display most interesting phenotypes on stiffer substrates, the $16.7kPa$ gel was most extensively used. Other rigidities were only used in the supporting experiments comparing maximal edge extension to maximal stress exerted by the cell (Sec. 6.2). For the same experiment, effect of cytoskeletal perturbators was also tested. The role of contractility was assessed impairing it with Myosin II inhibitor blebbistatin ($100\mu M$ (-)-blebbistatin, Sigma-Aldrich, Cat#B0560) or promoting it with calyculin A ($25nM$, Sigma-Alrich, Cat#C5552).

3.4 Microscopy and Image Analysis

All microscopy assays were performed using a Nikon Eclipse Ti inverted microscope (Nikon Corporation, Minato, JP) equipped with an ORCA-flash 4.0 (Hamamatsu Photonics K. K., Hamamatsu City, JP) operated with VisiView software (Visitron Systems GmbH, Puchheim, GE). Fluorescent images were acquired using PhotoFluor (89 North Inc., Williston, VT, USA) as a light source.

Images sequences of isolated keratocytes were usually acquired during polarization without moving until the cell would leave the field of view (FOV). After the cell had left, a picture of the undeformed substrate (reference frame) was then taken to obtain reference positions of the fluorescent beads. Two channels were used: phase contrast to retrieve the shape of the cells and fluorescence to measure the marker bead displacements in the substrate.

For assays on glass substrate, cell outlines were obtained from phase contrast sequences using an image segmentation program based on level-set active contours, developed by a former member of our team (Ambühl et al. (2012)). However, application of this method on TFM images was not possible. Beads embedded in the substrate impaired segmentation. For these conditions, cells were outlined manually. Outlines included 1200 points for the level-set method and 600 for manual segmentation.

For traction force microscopy, image sequences were pretreated in ImageJ (IJ) with a median filter (native IJ) and a background subtractor (MOSAIC suite, https://mosaic.mpi-cbg.de). An IJ plugin (introduced by Tseng et al. (2012)) was used to track beads and extract stress maps from beads displacements. The tracking procedure is called particle image velocimetry, a tracking method based on cross-correlation of interrogation windows rather than tracking individual particles. For experimental conditions in which cells were particularly weak (treatment with cytochalisin D and calyculin A) and for sparser bead densities, beads displacements were measured with MOSAIC suite bead tracker, which tracks single particles. The algorithm used for traction force computation is called Fourier transform traction cytometry (FTTC) (Butler et al. (2002)). Other reconstruction methods like finite elements method (FEM) or boundary element method (BEM) exist and are well described in Schwarz and Soiné (2015). The choice of FTTC is motivated by the fact that former lab members had already worked with it but also and mostly by the convenience of the available IJ plugin. Next section derives the theoretical background for this method.

3.5 Rheologic Description of TFM

Forces, play a crucial role in the way things go. They simply govern the behaviour of any system in time and space. But forces, like an electrical or gravitational field, cannot be seen. Only their effect is visible. In other words, forces are not directly measurable, they need to be inferred from the motion they produce. For example, weight is usually measured observing the deformation of a spring. The relaxed and loaded states of the spring are recorded and the weight is retrieved using the well known law $F = k \cdot \Delta x$ linking the deformation of the

spring Δx to the intensity of the force F via the spring constant k. The latter must be itself determined by a calibration experiment. In the case of traction force microscopy, forces are retrieved from the deformation cells ply on their environment. Let us derive the formulas needed to reconstruct forces from displacements in the case of TFM. Consider a strained body, the PAA gel substrate in our case. Each point of the body is located by its original position $\mathbf{x}$ and its displaced position $\mathbf{x}'$. In the framework of the theory of elasticity Landau L.D. (1986), strain is usually described by the *strain tensor* ε which reads for any point of the body

$$\varepsilon_{ik} = \frac{1}{2}\left(\frac{\partial u_i}{\partial x_k} + \frac{\partial u_k}{\partial x_i} + \frac{\partial u_l}{\partial x_k}\frac{\partial u_l}{\partial x_i}\right) \tag{3.1}$$

where $u_i = x'_i - x_i$ are the displacements, components of vector $\mathbf{u}$, and the summation rule applies. Strain is dimensionless. In this study, strains are small. Maximal strain is typically in of the order of 10^{-3}. In this case, the second order term can be neglected. Else, another method that accounts for non-linearities, e.g. 3D-TFM, would need to be used. The linear tensor is simply given by

$$\varepsilon_{ik} = \frac{1}{2}\left(\frac{\partial u_i}{\partial x_k} + \frac{\partial u_k}{\partial x_i}\right) \tag{3.2}$$

In the same framework, the natural way to characterize forces applied to an elastic body is the *stress tensor* σ where each component σ_{ik} is the ith component of the force on unit area perpendicular to the x_k-axis. In the present work, components of the form σ_{ii} corresponding to forces normal to the surface are considered to be negligible. Thus only off-diagonal terms matching tangential forces are non-zero.

The last element needed to fully describe the system is a set of equilibrium equations. The force acting on a unit volume can be written in the following way

$$F_i = \frac{\partial \sigma_{ik}}{\partial x_k}. \tag{3.3}$$

At equilibrium, all the internal forces vanish thus the equations are

$$\frac{\partial \sigma_{ik}}{\partial x_k} = 0 \tag{3.4}$$

In order to derive formulas from first principles, further hypotheses must be made. The body is considered isotropic and it remains at the same temperature prior and after deformation. It was already mentioned that the strain is small. In this case, deformation is proportional to applied forces. It's Hooke's law

$$\sigma_{ik} = \frac{E}{1+\nu}\left(\varepsilon_{ik} + \frac{\nu}{1-2\nu}\varepsilon_{ll}\delta_{ik}\right) \tag{3.5}$$

where E is the material's Young modulus and ν its Poisson ratio. This last equation can be inverted to obtain strain as a function of stress

$$\varepsilon_{ik} = \frac{1}{E}\left((1+\nu)\sigma_{ik} - \nu\sigma_{ll}\delta_{ik}\right). \tag{3.6}$$

Substituting Hooke's law for stress (equation 3.5) in the equation for equilibrium (equation 3.4) gives

$$\frac{\partial \sigma_{ik}}{\partial x_k} = \frac{E}{1+\nu}\left(\frac{\partial \varepsilon_{ik}}{\partial x_k} + \frac{\nu}{1-2\nu}\frac{\partial \varepsilon_{ll}}{\partial x_i}\right) = 0. \tag{3.7}$$

Finally, using the expression of the strain tensor for small deformation (equation 3.2) yields

$$(1-2\nu)\frac{\partial^2 u_i}{\partial x_k^2} + \frac{\partial^2 u_l}{\partial x_i \partial x_l} = 0 \tag{3.8}$$

which in vector notation writes

$$(1-2\nu)\Delta \mathbf{u} + \nabla(\nabla \cdot \mathbf{u}) = 0. \tag{3.9}$$

For a distribution of point forces, the solution is generally written with the equation Green's function

$$\mathbf{u}(\mathbf{x}) = \mathbf{G}\mathbf{F}(\mathbf{x}) = \int \mathbf{G}(\mathbf{x},\mathbf{x}')\mathbf{F}(\mathbf{x}')\,d\mathbf{x}' \tag{3.10}$$

In the present case, many simplifications can be made on the set of equations. First, since the material is isotropic, the operator L of components $\mathrm{L}_{ik} = (1-2\nu)\frac{\partial^2}{\partial x_i^2}\delta_{ik} + \frac{\partial}{\partial x_i}\frac{\partial}{\partial x_k}$ describing the system has constant coefficients. Green's function thus depends only on the difference between the points of measures $\mathbf{G}(\mathbf{x},\mathbf{x}') = \mathbf{G}(\mathbf{x}-\mathbf{x}')$. Second, let us consider the system. The rigidity of the gels used in this study implies that substrate is large compared to the displacements caused by cellular traction and can be considered as an infinite half space. For intelligibility, let the free surface be the xy-plane with the inside of the medium in $z > 0$. The solution derived by J. Boussinesq detailed in Landau L.D. (1986) can be used. In this solution, the displacements in every direction depend on the three components of the force. However, when the material is nearly incompressible, i.e when its Poisson ratio $\nu \approx 0.5$, which is the case of polyacrilamide ($\nu \approx 0.45$), the term depending on the vertical force vanishes at the surface. This means that it is possible to reconstruct tangential forces applied to the substrate only with displacements measured at the surface. The tensor for in-plane displacements and forces finally reads

$$\mathbf{G}(\mathbf{x}) = \frac{1+\nu}{\pi E r^3}\begin{pmatrix} (1-\nu)r^2 + \nu x^2 & \nu xy \\ \nu xy + (1-\nu)r^2 + \nu y^2 & \end{pmatrix} \tag{3.11}$$

where $r = \sqrt{x^2+y^2}$.

3.6 Solving the Inverse Problem

The problem that was set in the previous section is formulated in the form causes → effects. The goal now is to invert the equation and obtain the forces as a function of the measured displacements. In order to do this, it is convenient to work in Fourier space because the

convolution in equation 3.10 becomes a mere multiplication

$$\tilde{\mathbf{u}}(\mathbf{k}) = \mathbf{G}(\mathbf{k})\tilde{\mathbf{F}}(\mathbf{k}) \tag{3.12}$$

where the tilde denotes a Fourier transform. The forces in real space simply follow

$$\mathbf{F}(\mathbf{x}) = \mathscr{F}^{-1}\left(\mathbf{G}^{-1}(\mathbf{k})\tilde{\mathbf{u}}(\mathbf{k})\right) \tag{3.13}$$

where $\mathscr{F}^{-1}$ is the inverse Fourier transform. The Fourier space matrix representation of Green's function reads

$$\mathbf{G}(\mathbf{k}) = \frac{2(1+\nu)}{Ek^3}\begin{pmatrix}(1-\nu)k^2+\nu k_x^2 & -\nu k_x k_y \\ -\nu k_x k_y & (1-\nu)k^2+\nu k_x^2\end{pmatrix} \tag{3.14}$$

with the symbol without subscript $k = \sqrt{k_x^2 + k_y^2}$.

In principle, forces can be reconstructed from measured displacements using equation 3.13. But this naive approach has a major flaw, it is severely affected by noise. The green function is long ranged, it decays in $\frac{1}{r}$. As equation 3.10 is a convolution product, the forward problem corresponds to a smoothing operation. Thus, the inverse problem will be highly sensitive to small deviations. Noise introduces small details in the displacement field that the algorithm will try to accommodate introducing artefactual forces acting against each other. In other words, in the presence of noise, the inverse problem is ill-posed (Schwarz et al. (2002)). In practice, noise can come from a diverse number of causes. To mention the most prominent ones, noise can come from inhomogeneities in the substrate, mistracked marker displacements, insufficient coupling between beads and substrate (Sabass et al. (2008)) or fault in the image acquisition such as shifting of the field of view and defocusing (likely due to thermal expansion during the conduct of the experiment). While the latter can be corrected to a certain extent with image processing techniques (alignment, filtering, etc.), the issue of noise must be adressed with *a priori* knowledge about the force field. Two reasonable hypotheses are made on the traction forces. First, they never become excessively large and second they change smoothly. Those two assumptions lead to use a regularization method, namely zeroth order Tikhonov regularization. A.N. Tikhonov pioneered the study of ill-posed problems and developed methods to solve them (Tikhonov and Arsenin (1977)). He introduced the notion of regularization, a method to build approximate solutions to such problems that are stable. The regularized formulation of equation 3.13 is the following,

$$\mathbf{F}(\mathbf{x}) = \mathscr{F}^{-1}\left((\mathbf{G}^T\mathbf{G} + \lambda\mathbb{1})^{-1}\mathbf{G}^T\tilde{\mathbf{u}}\right) \tag{3.15}$$

with λ the regularization parameter. Dependence in $\mathbf{k}$ in the right-hand side of the equation was omitted for legibility. The determination of the regularization parameter is crucial for the accuracy and correctness of the output solution. The impact of λ on the solution is best illustrated using the real space formulation of the regularized problem

$$\mathbf{F} = \min_{\mathbf{F}_e}\left(|\mathbf{u}_r - \mathbf{u}_m|^2 + \lambda^2|\mathbf{F}_e|^2\right) \tag{3.16}$$

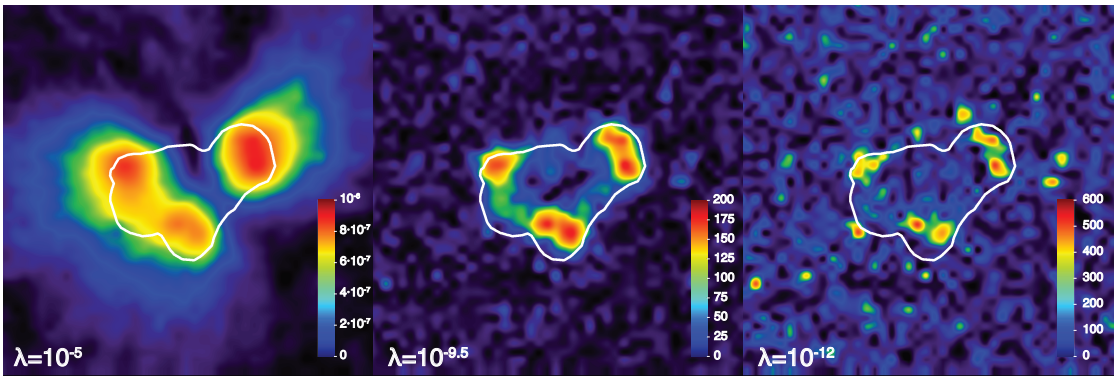

Figure 3.2 – Example of the effect of regularization parameter on the traction force map. The map in the middle was performed with the value of the parameter used for these experimental conditions. For the one on the left, (resp. right) a larger (smaller) value was used. The cell edge is shown in white. Value of the regularization parameter is given on the bottom left corner of each picture. The stress is given in Pascals.

where the symbol |.| denotes the L^2-norm. In this equation, $\mathbf{F}_e$ is the estimated force field, $\mathbf{u}_m$ is the experimentally measured displacement and $\mathbf{u}_r = \mathbf{G}\mathbf{F}_e$ is the reconstructed displacement obtained by the convolution defined in equation 3.10 of the estimated force and Green's tensor. The difference between the measured and reconstructed displacements is often referred as the residual norm $R = |\mathbf{u}_r - \mathbf{u}_m|$.

This formulation of the problem is computationally expensive to solve. However, it highlights the role of λ. The regularization parameter governs the relative importance of the two right-hand terms of equation 3.16. It will determine below which level small singular values for the displacement are filtered out of the solution. With a low λ, emphasis is put on the agreement between the estimated force field and the noisy measured displacements while a large value of the parameter will yield regularized and amplitude-constrained solutions losing high frequency contributions. A trade-off must be found between an undersized λ that will smooth out important features and yield poor spatial resolution and an undersized one that will leave artifacts, originating from noise, in place. Therefore, great care has to be taken on the choice of the regularization parameter. Figure 3.2 shows three stress maps reconstructed from the same displacement field for different values of λ. A high value, gives smooth force clusters with low magnitude and low noise. The traction force does not go beyond $10^{-6}Pa$. Also force clusters extend away from the cell boundaries, which makes no sense. For lower values of λ the force maxima grow and the range of force in the solution extends. Clusters are more distinguishable, there are more details to the organization of the stress. The background gets noisier until the noise gets as high as the signal. The picture in the middle was obtained with value of the parameter chosen in this work for the particular experimental conditions.

3.7 Determination of the Regularization Parameter

The regularization parameter must be consistent with the precision of the initial data. Moreover, it is advised to keep the value of λ fixed for comparing cells under similar experimental conditions (Plotnikov et al. (2014)). There are plenty of ways to determine the good regularization parameter for a set of experiments described in literature (Schwarz et al. (2002) Kulkarni et al. (2018)). One of the most popular criterion (Schwarz et al. (2002), Sabass et al. (2008), Stricker et al. (2010), Kulkarni et al. (2018)) is the L-curve featuring the two right-hand terms of equation 3.16. The magnitude of the estimated force field $\mathbf{F}_e$ is plotted as a function of the residual norm for different values of the regularization parameter. The value of the parameter corresponding to maximal positive curvature of this graph is chosen. However, in the case of this work, this criterion led to a large variety of prescribed values for the same experimental conditions. It was decided to used a signal to noise ratio of the TFM image as a criterion to select optimal regularization parameter. The latter was defined as the ratio between the maximal value recorded inside the cell and the maximal value outside. The mean signal to noise ratio was computed for each experiment for a range of regularization parameters $\lambda \in \left[10^{-11}, 10^{-7}\right]$ with an increment of $10^{0.1}$. The regularization parameters giving the highest signal to noise ratio were averaged and this value was used as the regularization parameter for the particular experimental condition. Some experiments did not display a clear maximum but rather a plateau value towards the small values of λ. Those experiments were not taken into account. The values of the regularization for different conditions were as follows: $1.67kPa$, $\lambda_{1.67} = 10^{-8.9}$; $4.5kPa$, $\lambda_{4.5} = 10^{-9.0}$; $16.7kPa$, $\lambda_{16.7} = 10^{-9.5}$; blebbistatin on $16.7kPa$, $\lambda_{blebb} = 10^{-9.4}$; cytochalasin-D on $16.7kPa$, $\lambda_{cytoD} = 10^{-9.0}$; calyculin-A on $16.7kPa$, $\lambda_{calyA} = 10^{-9.0}$.

4 Other Microscopy Techniques

4.1 Interference Reflection Microscopy

This technique provides a qualitative measure of the proximity of the cell to the substrate. In an interference reflection microscopy (IRM) image, the closer the cell is to the substrate, the darker it looks. The method makes use of thin-film interference. The light used for sample illumination travels three media with different refraction indices : glass ($n_g \approx 1.515$), culture medium ($n_m \approx 1.34$) and cell ($n_c \approx 1.37$ (Verschueren (1985)). At each interface, a fraction of the incoming light is reflected (Fig. 4.1 a). A first beam is reflected at the glass-culture medium interface and a second at the culture medium-cell one. The superposition of these reflected beams having different optical paths creates an interference image. Thus intensity of the interference depend on the spacing between the cell and its substrate. In addition to the different path lengths, the phase of reflected light can be shifted depending on the refractive indices of the media forming the interface. Reflected light is shifted of π at transition from lower to higher refractive index (like waves on a string attached to a fixed point on a wall, or a musical instrument). This is the case of the culture medium-cell transition. Thus interference is destructive when the cell is very close to its substrate. Indeed, in this case optical paths from the beam reflected on the glass-culture medium and the culture medium-cell one are almost identical, but since one is shifted and the other is not, interference is destructive. As the cell gets farther from the coverslip, difference between the two light paths changes, they become more in phase and image intensity increases. Using visible light illumination, the first intensity maximum is reached at a distance $d = \frac{\lambda}{4n_m} = \approx 100nm$[1], where λ is the light wavelength (Fig. 4.1 b). This range constitutes the first fringe of the interference pattern, also called *zero-order image*. Normally, an interference pattern is made of a succession of dark and bright fringes. Also, reflections from the upper cell-culture medium interface could contribute to the interference pattern yielding useless images. However, using high numerical aperture, higher order interference fringes cancel each other resulting in an uniform grey image (Verschueren (1985)). The interference image is thus constituted solely of the zero-order image carrying information about cell-substrate separations within the $0-100nm$ range. In this work, we illuminated samples with visible light using an oil immersion objective with 1.3

[1] We left out the dependence on incident angle for simplicity and because the principle is the same.

numerical aperture.

In the context of this work, IRM was used to analyse the position and movement of cell-substrate adhesions of spreading cells during protrusion-retraction cycles (Fig. 4.1). In general, adhesions are close to the substrate, generally not more than $15nm$. They will be the darkest spots in the IRM image (Barr and Bunnell (2009)). Also, even if the lamellipodium is flat and thin ($140-200nm$ (Laurent et al. (2005))), it is still too thick to interfere with the measure.

Interference reflection microscopy is a convenient technique for qualitative measurements of cell-substrate vicinity. It doesn't require any complex preparation of the sample. However, it includes some defects. Acquisition of accurate of IRM images requires strong sample illumination that can harm cells. Also, illumination is not uniform, thus sharpness of the image is spatially dependent: the closer to the center, the better. For this work, a tradeoff was found using strong illumination and placing cells slightly off the center of the field of view (Fig. 4.1 c). Non-uniformity of the background was further reduced by subtracting the background. However, this technique does not allow for precise location of the cell-substrate contact. This could be done by labeling of typical adhesion components such as integrin, or vinculin (Galbraith et al. (2002)). Moreover, information about contact spatial distribution and dynamics associated with traction force microscopy would allow for sharper traction force resolution (Schwarz et al. (2002), Plotnikov et al. (2014), Stricker et al. (2010)) and should be implemented in further studies.

4.2 Fluorescent Speckles Microscopy

Phalloidin is a toxin extracted from the infamous death cap mushroom (*Amanita phalloides*) which binds to F-actin. Associated with a fluorescent dye it can be used to selectively label F-actin. When small amounts of the drug are injected in the cell, phalloidin does not bind continuously to actin filaments but rather sparsely and it appears as little bright spots (speckles) on fluorescent microscopy images. Speckles of fluorescent dye in image sequences can be tracked to study local velocity of actin retrograde flow (Waterman-Storer et al. (1998)). This was done with particle image velocimetry using JPIV software (Venneman (2020)).

The advantage of this technique is that no genetic manipulation or overexpression is required but it also comes with a number of drawbacks. First about the drug, phalloidin binds slowly to filamentous actin (De La Cruz and Pollard (1996)), thus labelling is impaired near the edge of the cell where actin is polymerized. Also, even if small amounts of phalloidin do not kill cells, it hinders actin depolymerization - this is the reason why it is toxic at larger doses - so actin turnover and retrograde flow rates must be slightly different from their unperturbed levels. Moreover about the technical procedure, cells have to be injected with the drug one at a time, limiting drastically experimental throughput. Finally, it is not compatible with TFM. Other methods including the use of membrane permeable dyes or gene manipulation could improve experimental results.

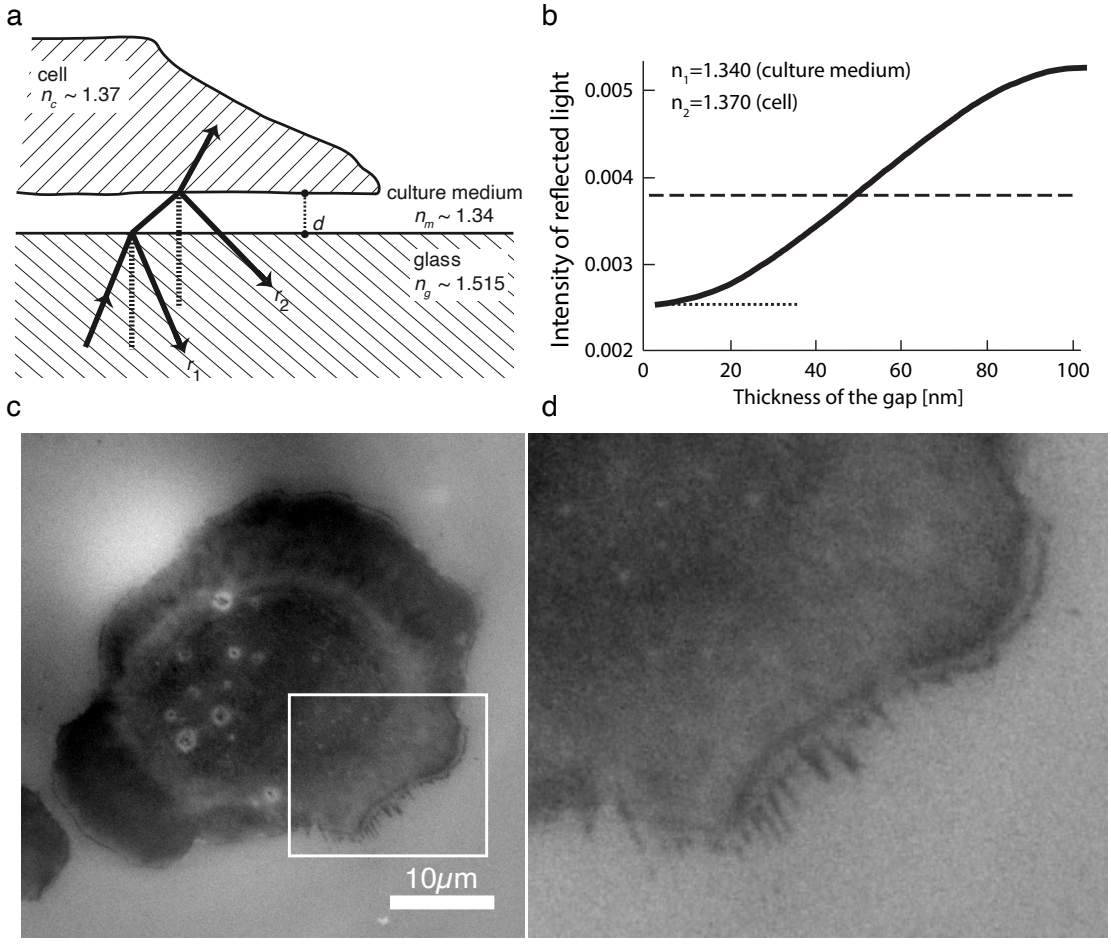

Figure 4.1 – Interference reflection microscopy. (a) Sketch of the situation, illumination light is reflected at the glass-culture medium and culture medium-cell interfaces. Refraction indices of the different media and thickness d of the culture medium film between glass and cell are indicated. (from Barr and Bunnell (2009)) (b) Intensity of reflected light as a function of distance d in nanometers from theoretical computation. Only zero-order image is shown. Values are normalized by intensity of the incoming light. Dashed line indicates background reflectivity baseline (redrawn from Curtis (1964)). (c) Typical IRM image. Bright spot on the top left is the center of the original image. The spot is due to non-uniformity of strong illumination. Scale bar 10μm. (d) Detail of IRM image (c). Darker region is visible just behind the cell-edge indicating zone of closer cell-substrate proximity.

Results and Discussion Part III

5 Phenomenology

Traction forces microscopy (TFM) is a technique that allows to measure the stress exerted by a cell on its substrate. Phase contrast microscopy makes it possible to retrieve the shape of the cell. Those two methods were used together in our experiments to image isolated cells to obtain sequences of pictures with both features. This chapter is a first glance at experimental results that can be acquired with this technology, a phenomenological description of cell polarization. Cells were usually selected during EDTA treatment (isolation and isotropization of cells, see part II) and imaged from the early stages of spreading until they polarized and left the field of view (FOV). Since TFM needs picture of the unstrained substrate (i.e. without the cell) to use as reference, moving the FOV to follow cells was not possible in those experiments. However, sequences of polarized cells passing through were also recorded. A detailed description of the conduct of TFM experiments can be found at chapter 3.

5.1 Traction forces during cell polarization

Fish epidermal keratocytes natively form bilayers at the base of scales. When a scale is extracted from the fish and stuck to a coverslip, the cell layers on the scale start spreading on the newly available substrate. Cells migrate together away from the scale forming a colony on the ECM-coated gel. The movement of the colony is very smooth. This changes when cells are individualized. Isolated keratocytes are remarkably active. Just after isolation, cells are rather round but they rapidly start fluctuating vigorously. They spread, dance around, and eventually polarize and become motile. In our experiments, we measured a mean velocity of the cell center of $19.10 \mu m \cdot \mathrm{min}^{-1}$ with a standard deviation of $5.66 \mu m \cdot \mathrm{min}^{-1}$ ($n = 5$ cells). Before polarization, the cell edge fluctuates in cycles of protrusion and retraction (Fig. 5.1 a, top). During this phase, changes in cell shape are accompanied by highly dynamical stress patterns (Fig. 5.1 a, bottom).

Stress exerted by cell is generally oriented towards the center of the cell (Fig. 5.1 c). Distribution of stress is correlated with movements of the edge (Fig. 5.1 a). Forming an almost continuous ring at the cell periphery in the early stages of spreading when the cell is round, regions of high stress then split into foci that follow the tips of extending regions of the cell (Fig. 5.1 a, 0s). During protrusion-retraction cycles, stress foci are constantly rearranging. They

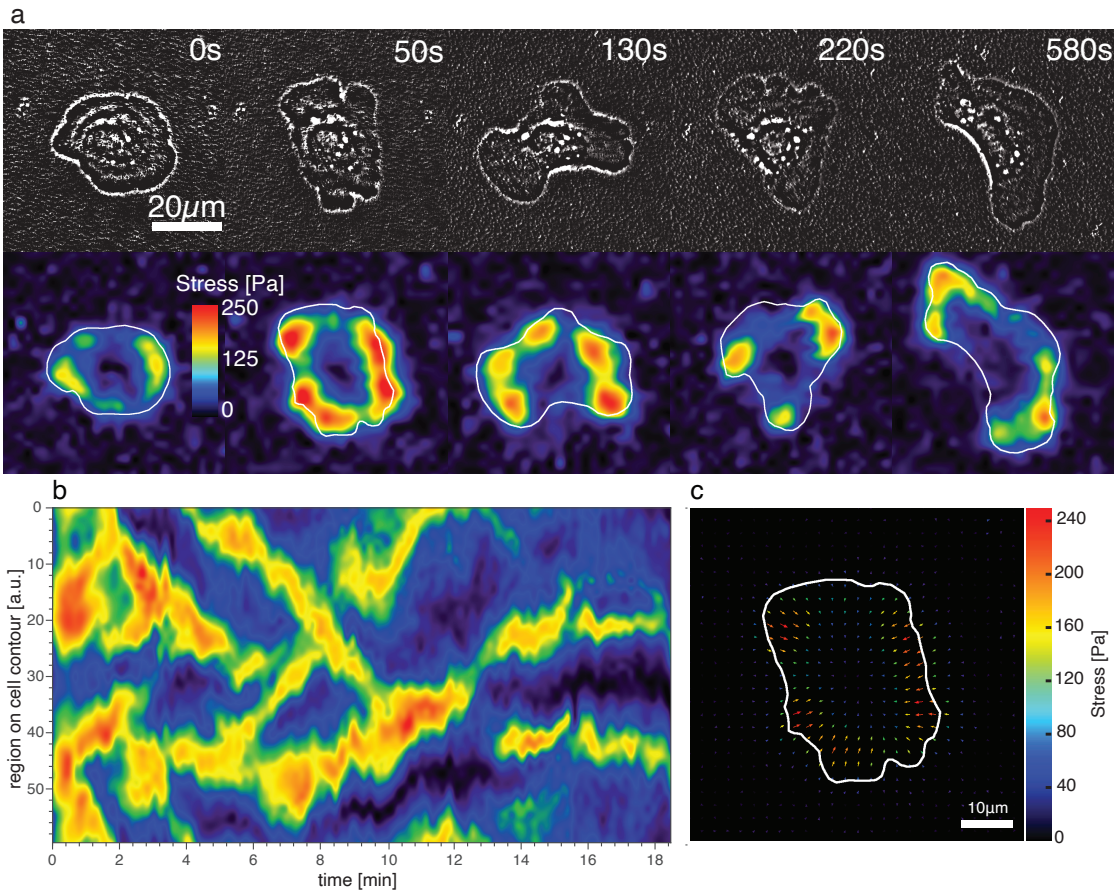

Figure 5.1 – Different representations of traction forces of a Keratocyte spreading in control conditions. (a)Timelapse of a cell spreading until polarization on PAA gel prepared for TFM. Top, phase contrast images, processed to highlight the cell edge. Bottom, corresponding shear stress maps. Stress amplitude is color coded and cell outline is shown in white. Scale bar $20\mu m$. (b) Stress along the cell edge. Stress is measured in a ring wrapping the cell outline and results from successive snapshots are aligned, like a curved kimograph. x-axis is time in minutes and y-axis the position along the cell outline (unit is arbitrary). Different phases of spreading are visible. In the beginning (0 – 2 min) a large portion of the edge displays high stress. Then, when the cell starts fluctuating (2 – 13 min), few spots appear that move diagonally indicating force foci move along the edge. Note that different foci move in opposite directions along the edge. Finally, as the cell polarizes (13 min to the end, only two regions of high stress remain and stabilize. (c) Vectorial map of the stress exerted by a spreading cell. Stress is oriented radially towards the cell center. Scale bar is $10\mu m$. Snapshot corresponds to second snapshot of (a) ($50s$). (a-c) Data from the same experiment and stress color coding is the same.

form, grow, move, split, merge and disappear concomitantly with changes in the cell geometry. Following protrusions, they move radially as well as in the direction tangential to the edge (Fig. 5.1 b). As the cell polarizes, foci are located at the two lateral extremities (Fig. 5.1 a, 580s). Regions of high stress no longer move in the reference frame of the cell. It is also possible to visualize the different behaviors of stress foci - continuous ring, moving around and fixed -

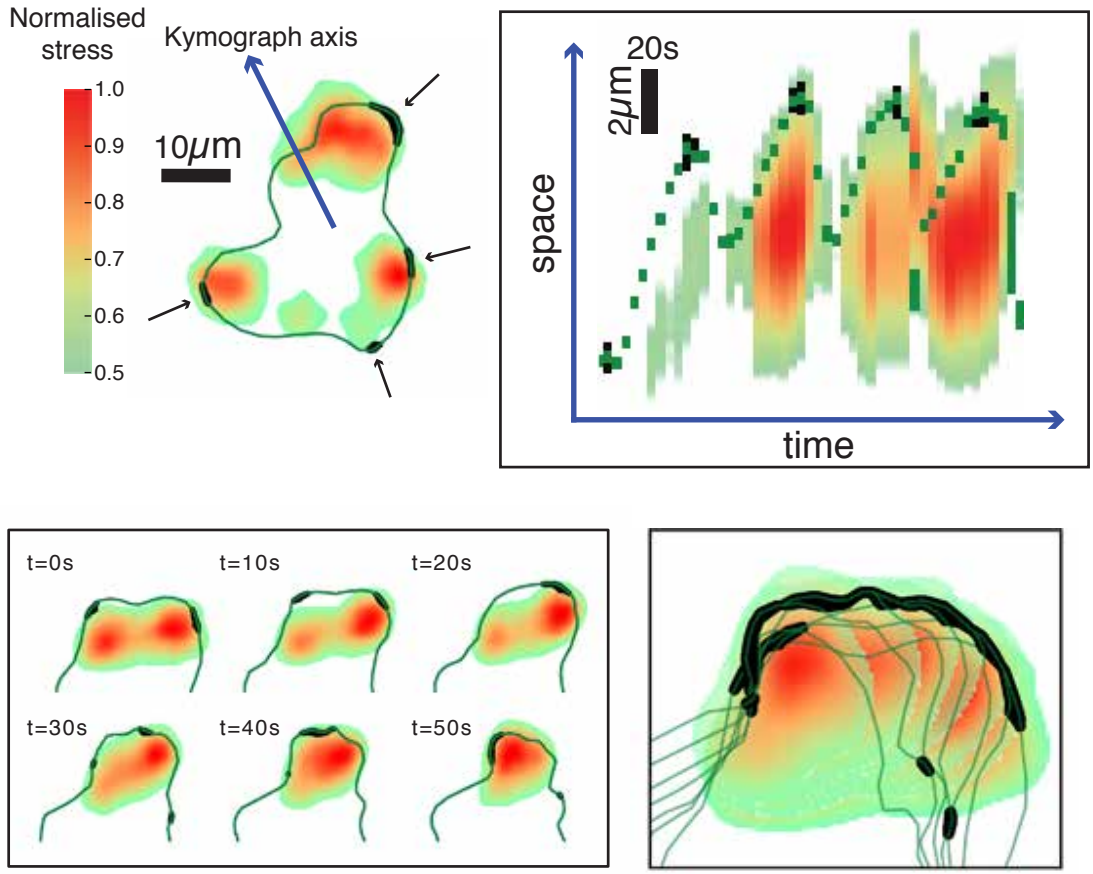

Figure 5.2 – Evolution of traction force foci during protrusion-retraction cycle. Traction forces are normalized to maximal stress in the sequence. Regions of the edge switching from protrusion to retraction are highlighted in black. Top: Kimograph along a radial axis. Scale bar on the kimograph gives both unit of time and space. Bottom: Evolution of foci during retraction of the edge.

with an angular stress map over time (Fig. 5.1 b).

High stress regions are universally found away from the cell center. A kimograph of stress along a radial axis during multiple protrusion retraction cycles shows that force foci follow the edge during the whole cycle (Fig. 5.2 top). The radial distance between the point of maximal stress and the edge remains constant during spreading (Fig. 5.3 a). As the cell area increases, the distance between cell center and position of maximal stress grows but the distance between maximal stress and cell edge stays fixed at $3.54 \pm 1.52 \mu m$. This result is consistent with the fact that strong focal adhesions are found away from the cell edge (Parsons et al. (2010)). It suggests coordinated reorganization of branched actin into force bearing stress fibers, stacking of myosin and growth of focal takes place within a specific region close to the cell edge which size does not depend on cell area.

An important observation about the location of force foci is their proximity to regions of the edge undergoing a switch from protrusion to retraction. Switch regions are located in

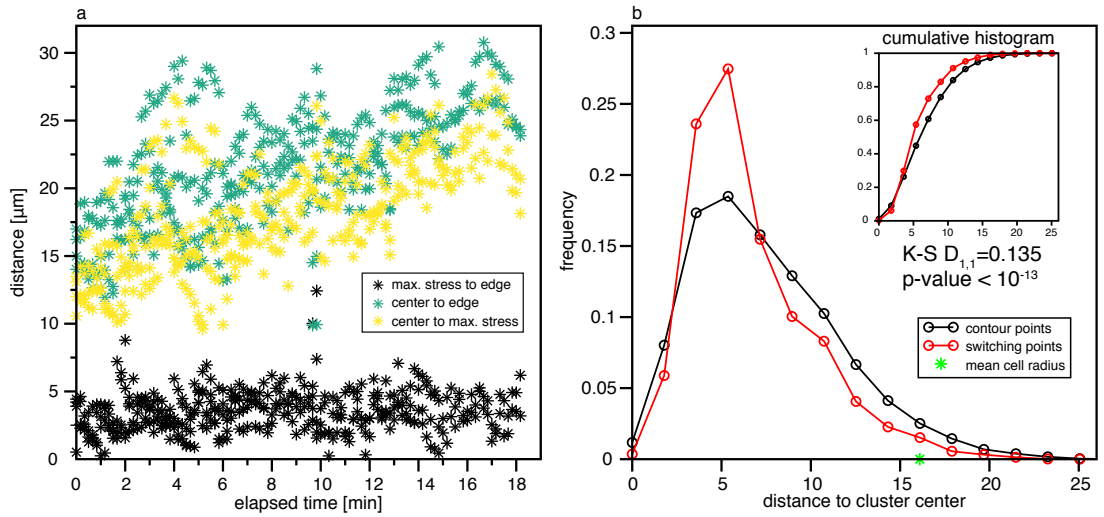

Figure 5.3 – Stress foci follow the cell edge and are correlated with switch from protrusion to retraction. (a) Maximal force found at fixed distance from edge. Plot of radial distances in the cell. Center to edge distance in green, center to max. stress in yellow and radial distance from max. stress to edge in black. x-axis denotes time in minutes and y-axis distance in μm. Data: 4 cells in control conditions. (b) Distribution of the distances from points on the cell outline to the center of force clusters. In red, regions undergoing a switch from protrusion to retraction, in black any point on the cell outline. Kolmogorov-Smirnov statistic was computed $D_{1,1} = 0.135$ with a p-value $< 10^{-13}$, indicating that the two distributions are different. The mean cell radius is indicated by a green star. Data: 3 cells in control conditions.

protruded regions around force clusters (Fig. 5.1). The center of stress clusters are close to switching regions of the cell edge. The distribution of distances from the center of force clusters to switching regions of the edge was measured and compared to distribution of distances to random any point of the edge (Fig. 5.3 b). While they both peak at about 1/3 of the mean cell radius, the two distributions are statistically different. Distribution of distances to arbitrary points on the cell edge is more spread out towards larger values. A Kolomogorv-Smirnov test confirmed significance of the difference ($D_{1,1} = 0.135$, p-value $< 10^{-13}$). Most switches from protrusion to retraction were reported to appear at maximal extensions (Raynaud et al. (2016)) while traction force foci are located near extending edges. Now we showed that their relative location is not random. While previous findings showed that geometry of the cell dictates the position of traction forces, this last observation draws attention to the fact that traction forces might in turn play a role in the regulation of the cell shape and edge motion.

5.2 Impaired contractility

Behavior of cells changes upon contractility impairment. Migrating keratocytes extend further (Okimura et al. (2018)) and distance sensing is partially inhibited (Raynaud et al. (2016)). Cell spreading is also strongly affected by contractility inhibitor blebbistatin (Fig. 5.4 a).

Fluctuations of the edge are gone. No more dancing keratocyte, they stand still. The drug also drastically reduces the stress intensity and dynamics. Stress is typically an order of magnitude lower than in control conditions. A contractile ring can still be seen at the beginning of spreading but it never breaks into clusters. Stress foci are gone. No dynamic rearrangement of the stress is observed. The only visible feature is a dim ring of stress at the cell periphery. Cells exhibit heavily reduced to no protrusion-retraction cycles at all. Cells in such conditions do nevertheless polarize. A large unbalanced edge retraction usually sets off motility. At this point (Fig. 5.4 a, $t = 880s$), stress is so low that it is not possible to distinguish from background with this substrate rigidity ($16.7kPa$).

The fact that cells polarize under such conditions indicates that myosin II is not required for breaking symmetry, but blebbistatin treated cells polarize abnormally. Keratocytes tend to split by elongating uncontrollably until they tear or by having multiple protrusions going in different directions. Figure 5.4 b shows a blebbistatin treated keratocyte splitting upon polarization. Collisions with obstacles or cells are particularly impressive. If the cell is not completely blocked, parts that are not obstructed might continue crawling until rupture. These behaviors are regrettably difficult to lay out on a still image.

Cells treated with blebbistatin however display force-induced local retraction of their edge. In the experiment shown in figure 5.4 c, a pipette is used to pull on the substrate next to the cell. This results in retraction of the edge next to the place where the substrate is strained. The incurred retraction is dramatic. The cell polarizes and its sides elongate as it usually does in such conditions. For this experiment, the solution is so much saturated with blebbistatin that it is possible to see undissolved crystals floating around the cell. It is also important to stress the fact that the pipette never touches the cell and merely pulls the substrate horizontally away from the cell inducing strain in the substrate below the cell.

This experiment shows how an external force can induce edge retraction, even when the cell is not capable of building stress itself. Experiments with a blebbistatin saturated medium highlight the important role that traction forces play in the ability of the cells to retract their edge and maintain physical integrity.

In general, the location and behavior of force during polarization: contiguous movement of cell edge and stress foci, proximity of high stress and switch regions and apparent necessity of traction forces for normal polarization, indicate interplay of stress and edge dynamics. In the following chapters we are going to investigate quantitatively the mutual impact of these two processes.

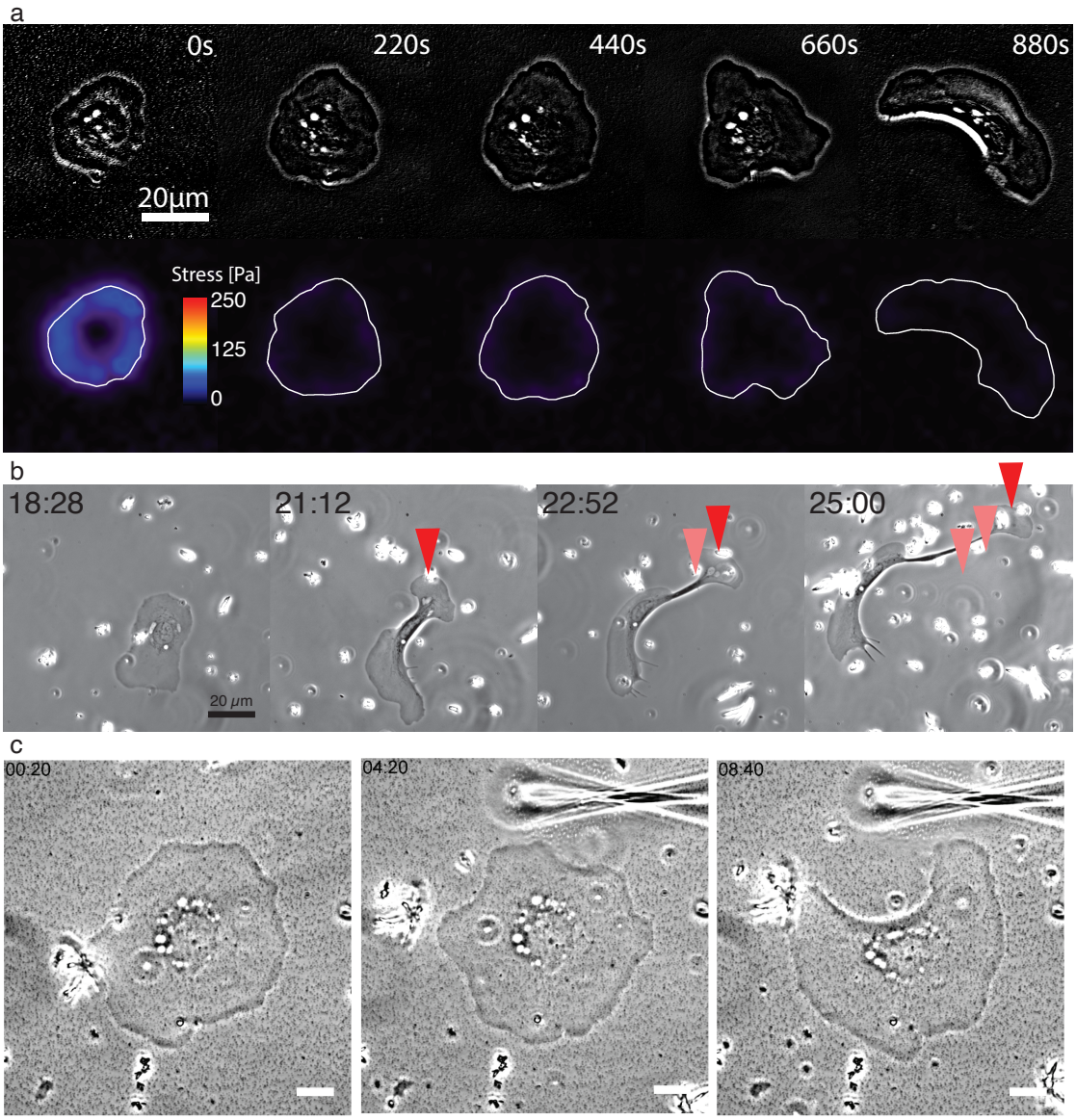

Figure 5.4 – Experiments with impaired contractility. (a) Sequence of snapshots of a Keratocyte spreading in presence of $100\mu M$ (-)-blebbistatin. Top, phase contrast images, processed to highlight the cell edge. Bottom, corresponding shear stress maps. Stress amplitude is color coded and cell outline is shown in white. Color scale for stress amplitude is identical to the scale used for control conditions (Fig. 5.1) to allow for comparison. Scale bar $20\mu m$. (b) Sequence of a blebbistatin treated cell undergoing polarization on glass. The cell body divides in two distinct polarized parts that travel in different directions. The smaller fragment indicated by red arrows travels towards the top right corner while the rest of the body goes to the left. Lighter red arrows indicate the former position of the small fragment. The field of view is fixed for the whole sequence. The start of the sequence is not shown. Time (format min:sec) is indicated on the top left of each pannel. Scalebar is $20\mu m$. The solution contains $100\mu M$ of blebbistatin. (c) A blebbistatin treated keratocyte's edge retracts when the substrate next to it is pulled on with a micropipette. The solution contains $100\mu M$ of blebbistatin. Time (format min:sec) is indicated on the top left of each pannel. Scalebar is $30\mu m$. (b-c) Bright debris are undissolved crystals of blebbistatin indicating solution is saturated. (c)

6 The Force-Distance Relationship

In (Raynaud et al. (2016)), it had been shown that the switches from protrusion to retraction appear most likely at the longest distance from the cell center. We have just shown that high stress areas are found in protruding regions of the cell and close to switches from protrusion to retraction during cell spreading. During migration, traction force is high at the sides of the cell where most of the switches were recorded. After phenomenological considerations we are now going to get more quantitative and gather evidence that traction forces can underlie the distance rule.

6.1 Force meets distance

Probability for a switch from protrusion to retraction to occur strongly depends on distance from the center of the cell. Then, if traction forces play a role in the organization of cell edge dynamics, they should also be related to distance. We first investigated how force is related with distance. Using traction force microscopy images, stress inside cell area was measured and a force-distance relationship was established (Fig. 6.1 a). Indeed, stress correlates with distance to cell center. Spearman test yields a value of $\rho_S = 0.67$ with p-value $p < 10^{-3}$. In order to compare data from every cells in control conditions during whole sequences from spreading to after polarization, both stress and distance were normalized at each frame by the maximal value in the frame. Different cells exhibit various stress intensities and extension ranges. Also, as they spread, cell maximal extension increases and stress generally decreases (Fig. 6.1, b). Nevertheless, considering short time intervals, positive correlation between stress and distance is still evident even without normalization.

The same data was used to test whether distance is the real geometrical parameter governing stress and cell-edge dynamics. Maximal stress has been suggested to depend on the longest cell dimension Rape et al. (2011). Another study Oakes et al. (2014) has reported that total stress depends on cell's total spread area and that local stress depends on the local curvature of the edge. Therefore, we analyzed the relationship between stress and local edge curvature as we did for distance. This time, no correlation was found between the two parameters (Fig. 6.1 c). Spearman's rank correlation coefficient $\rho_S = 0.11$ (again with $p < 10^{-3}$). We also investigated correlation between curvature, distance and switches from protrusion to

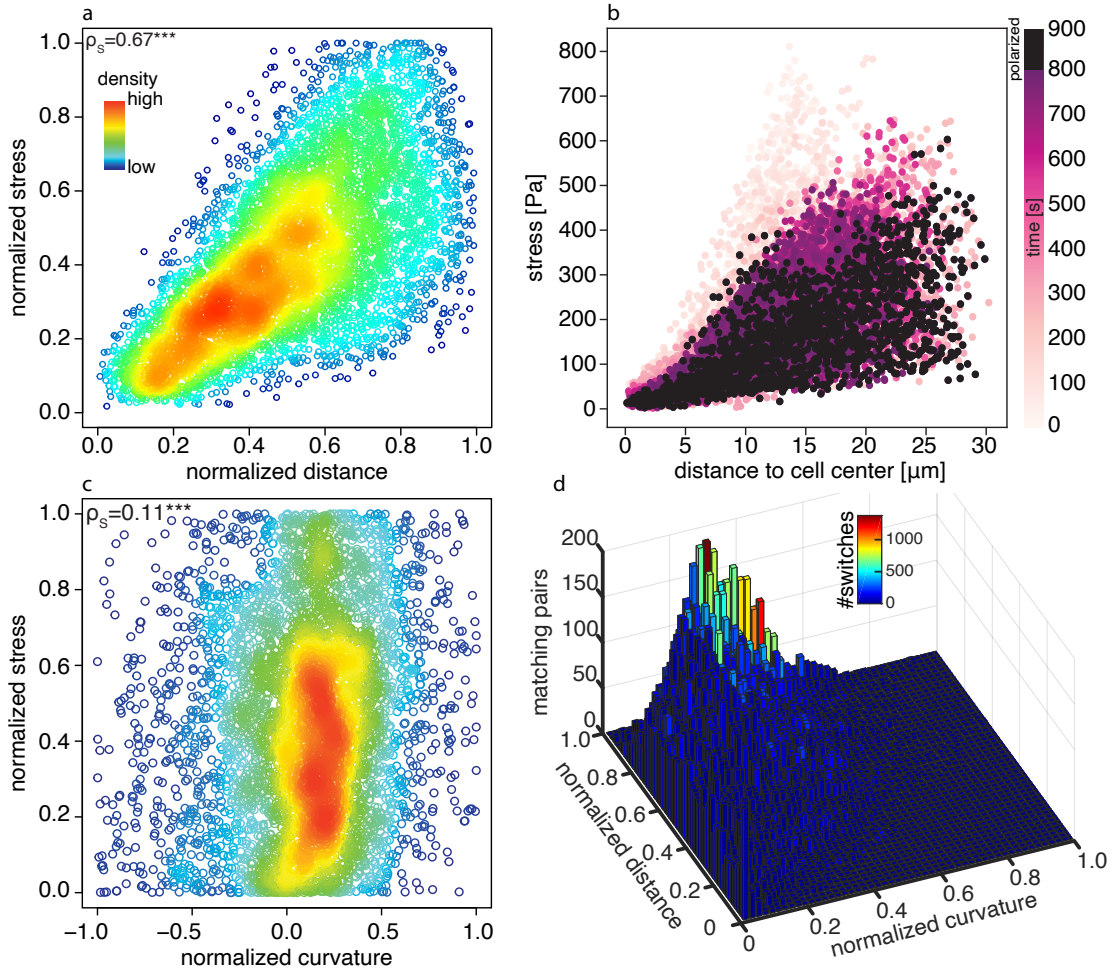

Figure 6.1 – Stress relationships. (a) Stress-distance relationship. Plot of normalized stress inside the cell as a function of normalized distance to the cell center. (a,c) Value of Spearman's rank coefficient ρ_S is indicated and the three stars (***) indicate a p-value $p < 10^{-3}$. Color codes for spatial density of data points. For clarity, only 3% of the data is shown. (b) Non-normalized stress-distance relationship. Plot of stress in the cell area as a function of distance to the center of the cell. Stress is measured in Pascals and distance in μm. The complete sequence of a traction force microscopy assay for one cell was used, from the early stages of spreading until the cell left the field of view. Time is color-coded. Black data points indicate the cell frames after polarization. (c) Stress-curvature relationship. Plot of normalized stress as a function of normalized local edge curvature. (d) Distribution of distance-curvature pairs and number of protrusion-retraction switches. Height indicates the frequency of distance-curvature pairs. Color codes for the number of switches recorded force each specific distance-curvature doublet. (a,c,d) Data comes from 306 frames of traction force microscopy assays from 3 different cells in control conditions plated on $16.7 kPa$ PAA gel. Distance and stress were normalized by their maximal value in each frame, for curvature maximal absolute value was used.

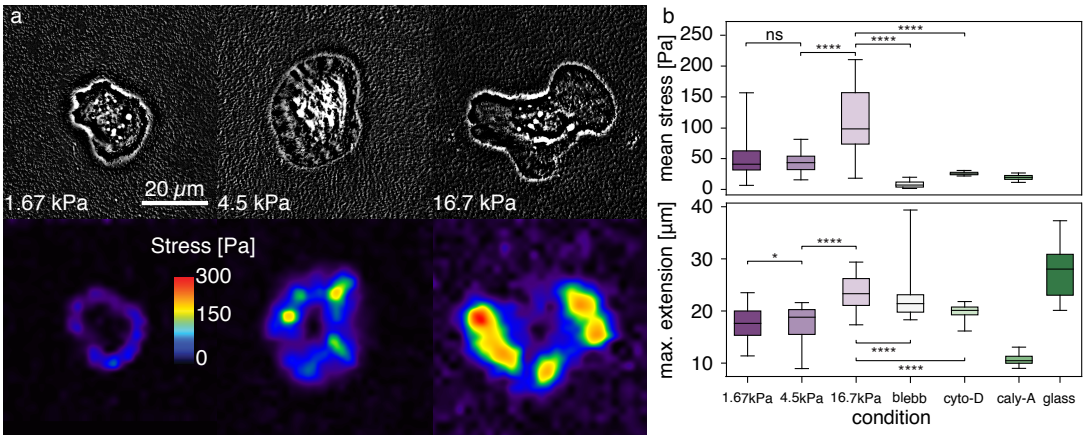

Figure 6.2 – Mean stress and maximal extension of cells in different experimental conditions.

retraction. For each point on the cell outline, distance to the cell center and local curvature were measured. Distribution of the distance-curvature pairs was computed. On top of that, we counted the number of switches occurring for each distance-curvature doublet[1] (Fig. 6.1 d). It appears, that distance and curvature are indeed not independent. Short distance is associated was low curvature and longer distances with high curvature. However, the vast majority of switches happen at highest distances while they appear in a wide range of curvatures. We found that both stress and tendency to initiate retraction grow with distance and that in-plane curvature does not come into play.

Our results differ from Oakes et al. (2014). The reason for this might come from the fact that they studied different cells. While we analyzed fast migrating and shape-changing epidermal keratocytes, authors of Oakes et al. (2014) studied slow, strong-pulling 3T3 fibroblasts. Organization of stress fibers in those cells is different.

6.2 Changing Experimental Conditions

Different experimental conditions can lead to drastic changes in the behavior of the cell. As mentioned in the previous chapter, blebbistatin significantly reduces stress exerted by cells and hinders polarization while cell extension can get huge. In this case, relationship between force and distance is certainly distinctive from control conditions. To get more insight on the robustness of the relationship, we conducted TFM assays under different conditions changing the substrate stiffness or adding a drug to the media.

We tested 3 different rigidities 1.5, 4.5 and 16.7kPa. Cell spreading and traction forces depend on substrate stiffness. Maximal edge extension and mean stress were significantly lower on 1.5 or 4.5kPa gels than on the most rigid one (Fig. 6.2). This result is consistent with previous findings about adhesion reinforcement by substrate rigidity (Yip et al. (2013), Panzetta et al. (2019), Bangasser et al. (2013)). Edge fluctuations were also strongly diminished

[1] This was actually the first analysis performed in the context of this thesis.

on soft substrates (Fig. 6.2). Cells did not exhibit the breathing phenotype observed on glass and high rigidity gels (see Fig. 1.9 and 5.1). Cells also polarized faster on softer gels. In general, polarization was triggered by a single retraction at the prospective rear or formation of an unbalanced protrusion (Bornert (2016)), as also reported in (Cramer et al. (2018), Barnhart et al. (2015)). Faster polarization is consistent with reported coupling between retrograde flow and persistence of motion (Maiuri et al. (2015)). Indeed, retrograde flow was reported to be negatively correlated with substrate stiffness (Barnhart et al. (2011)).

As a matter of fact, substrate stiffness of $16.7kPa$ was chosen for control conditions and the vast majority of experiment were performed with this rigidity. It is a good tradeoff. It was stiff enough for cells to display large protrusion retraction cycles like they do when plated on glass coverslips. It also allowed for accurate traction force measurements. Softer gels were so weak that cells were sometimes able to deform them plastically making stress reconstruction impossible. Stiffer gels were dismissed because bead displacements were too small to allow for precise stress measurements.

In addition to changing substrate stiffness, the system was perturbed using drugs known to interfere was cytoskeletal dynamics. Blebbistatin and two other drugs were used: calyculin A, a toxin that increases myosin activity (MacKintosh and MacKintosh (1994)) and cytochalasin D which inhibits actin polymerization. For these experiments, cells were cultured in stiff gels ($16.7kPa$). Traction forces exerted by the cells were strongly reduced in all three conditions (Fig. 6.2 b) blebb, cyto-D and caly-A conditions). Edge fluctuations were also diminished. Cytochalasin D and calyculin A induced cells to retract. These cells did not polarize and some cells treated with calyculin A were so contracted that they detached from the substrate. Regarding blebbistatin, as already mentioned, edge extension and fluctuations were also reduced during polarization (see Fig. 5.4) but cells extended much more once polarized, sometimes until rupture. This is reflected in the asymmetric extension distribution with large number of very high extension values.

In all these conditions, except for migrating cells under blebbistatin conditions that extended uncontrollably, changes in cell extension and traction forces were parallel. Decreased cell extension was accompanied by low traction forces. Cells extended to different distances and retracted at different stress values, but in general stress-distance relationship was preserved. These results also suggest that control of edge activity and traction forces depend on the balance of multiple factors such as myosin contractility, actin polymerization and adhesion strength. The fact that calyculin A, an activator of cell contractility, decreases cell extention and traction forces could be explained by an increased cytoskeletal contraction that is not balanced by an increase in adhesion thus leading to retraction instead of traction force enhancement. Uncontrollable extension of polarized cells under blebbistatin also indicate that balance between actin polymerization and contractility is essential for regulation of edge activity and physical integrity.

7 Force-distance relationship as an emergent property of the actomyosin network

In a recent work, it was reported that elastic fiber networks can amplify contractile stress (Ronceray et al. (2016)). It was shown that local active contractile units (force dipoles) embedded in an elastic fiber network can yield forces on the boundary of the network larger than the actual force of the unit. Following this idea, we asked ourselves whether distance dependence of stress observed in our experiments could arise from such a mechanism. In particular, we wanted to know if the force-distance relationship could be an intrinsic property of contractile fiber networks or if a broader picture involving cytoskeletal and adhesion dynamics would be needed. To test this hypothesis, we developed a mechanical model of actin, myosin and adhesions.

7.1 Model Description

The model features a network of elastic filaments depicting actin with attractive force dipoles inserted between network nodes portraying myosin and fixed anchors emulating cell-substrate adhesions (Fig. 7.1 a). The network is made of repeating units (or bonds) on a hexagonal lattice with some depleted bonds. A unit is made of two rigid segments. This allows filaments to bend and buckle under load (7.3). Each bond includes three nodes, two on the lattice (lattice nodes) that can be shared by several bonds (up to 6) and one in the middle (midpoint node) (Fig. 7.3 a). Midpoints are introduced for computational purposes and to help visualization of bent filaments in the system (Fig. 7.3 b). Force dipoles are defined as pairs of neighboring lattice nodes attracting each other. Dipoles do not need to be supported by a bond, any pair of direct neighboring lattice nodes can form a dipole. Anchors are immobile lattice nodes.

The network is initialized with random distributions of its different components. A numerical optimization method is used to find a minimum energy configuration and the resulting state is analyzed. During energy minimization, the system can be deformed. Apart from fixed anchors, nodes can move freely. Filaments can be stretched, compressed, bent and buckled (Fig. 7.1 b) with a defined energy cost.

We consider nearly inextensible fibers but that are quite easy to bend. This provides asym-

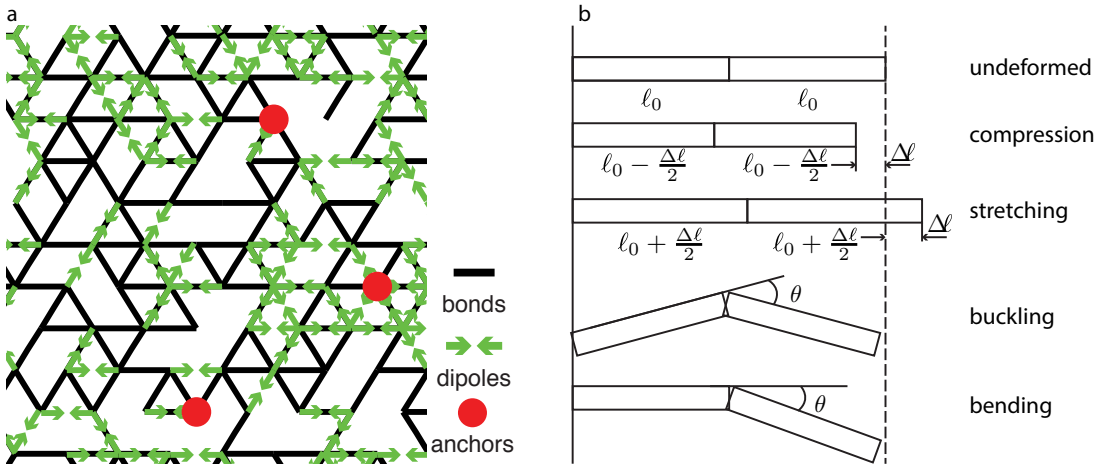

Figure 7.1 – Description of the mechanical model. (a) Sketch of the network and its components. Black segments are elastic bonds. Green arrows depict force dipoles. Red dots are fixed nodes (anchors). It is possible to see that not all dipoles are supported by a bond. (b) Different modes of deformation of the elastic bonds.

metry and non-linearity to the system. Apart from the asymmetric behavior of the filaments, non-linearity is also introduced by geometry. A system with purely elastic constituents can have a non-linear response (Fig. 7.2).

7.1.1 Network Initialization, Model parameters and Energy Considerations

Compared to previous studies using simple geometries, we generated the system inside realistic shapes extracted from real polarizing cell outlines. The network is first initialized by filling the whole hexagonal lattice inside the shape with bonds. Bonds are then depleted with probability $1-\rho$. This probability defines the first model parameter, bond density ρ. A regular, fully populated lattice corresponds to $\rho = 1$. Subsequently, anchors are distributed randomly in the system. Probability for a lattice node to be fixed is determined by anchor density ρ_a. Finally, dipoles are allocated on pairs of lattice nodes with probability ρ_d. Nodes forming a dipole do not need to be linked by an elastic bond. Any pair of nodes separated by a distance smaller than threshold $d_t = 2\ell_0$ can be picked. Dipoles are placed randomly in the network and multiple dipoles can be associated with the same pair of nodes. The last two parameters are the force dipole magnitude M and the spring constant of elastic bonds μ. It is very likely that the energy of the randomly initialized system is not the minimal one. Therefore, we let the system evolve toward a new configuration of lower energy using the Broyden-Fletcher-Goldfarb-Shanno (BFGS) optimization method to find a minimum of energy.

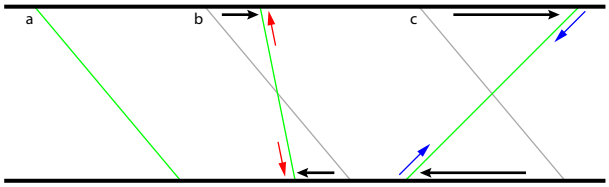

Figure 7.2 – Example of non-linear response originating from geometry. An elastic element (spring), represented in green is attached to horizontal boundaries (black). (a) Spring is at rest. (b-c) Spring is sheared. (b) For small strain, the element is compressed. It will exert a pushing force on the boundaries (indicated by red arrows). (c) For higher strain as the vertical axis is crossed, it will be stretched. Force exerted by the spring will change direction. The element will exert a pulling force on the boundaries (indicated by blue arrows). (b-c) Rest state of the filaments is represented in light gray. Bold black arrows indicate the amount of shear. Adapted from Ronceray (2016)

7.1.2 Energy in the Model

Energy in the system comes from three different sources: dipole energy E_d, bending energy E_B and elastic energy E_S. In general, dipole force is attractive and constant with value F. The energy of a dipole is just

$$E_d(\ell) = F \cdot \ell \tag{7.1}$$

where ℓ is the distance between the nodes forming the dipole.

Following Ronceray et al. (2016), we use the Worm-Like Chain (WLC) model to describe actin filaments. This model was introduced in Kratky and Porod (1949) and is well suited to model biopolymers at the subcellular scale (Broedersz and MacKintosh (2014)). It describes a chain inextensible elastic segments. Orientation of consecutive segments can change with a finite energy cost. Bending energy associated with orientation change reads

$$E_B = \frac{\kappa}{2} \int ds \left| \frac{d\vec{t}}{ds} \right|^2 \tag{7.2}$$

where κ is the *bending modulus*, the intrinsic rigidity of the chain. In the integral, $\vec{t}$ is the unit tangent vector and s the (contour) length along the chain (Fig. 7.4). The term $\left| \frac{d\vec{t}}{ds} \right|$ is the local curvature (or inverse of the radius of curvature) of the chain. Considering a segment of length $2\ell_0$ bent uniformly with curvature radius R, the bending energy will thus be

$$E_B = \frac{\kappa \ell_0}{R^2}. \tag{7.3}$$

Due to thermal fluctuations, orientation of the segments changes along the chain. The *persistence length* of segment orientations along the chain is $\ell_p = 2\kappa / k_B T$ (Broedersz and MacKintosh (2014)). The bending energy can be rewritten

$$E_B = \frac{k_B T \ell_p \ell_0}{2R^2}. \tag{7.4}$$

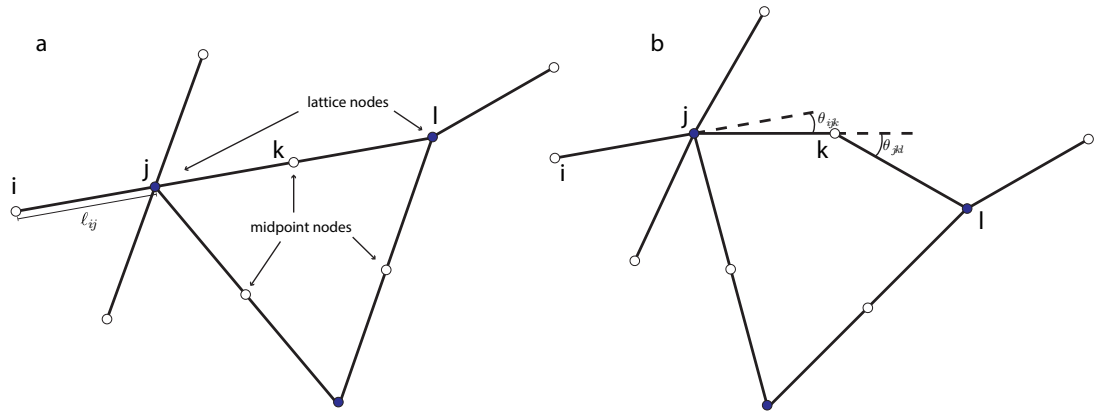

Figure 7.3 – Sketch of the lattice. Blue dots represent lattice nodes and white dots are midpoints. (a) Undeformed network, rest length ℓ_0 of bond segment is indicated. Note that even if nodes i, j and k are node part of the same bond, they are consecutive and aligned in the initial configuration. There will therefore be a cost for bending. (b) Deformed network with deflection angles.

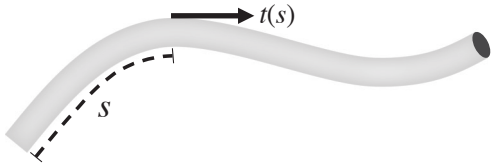

Figure 7.4 – Parametrization of the fiber in the worm-like chain model. s is the length and $\vec{t}$ the unit tangent vector along the chain

Assuming bending is spread uniformly along the element[1] the radius of curvature can be expressed as a function of the angle θ between the segments forming the hinge

$$R(\theta) = \frac{\ell_0}{2\sin(\theta/2)} \tag{7.5}$$

and the bending energy as a function of the angle is thus

$$E_B(\theta) = \frac{k_B T \ell_p \xi}{2\frac{\ell_0^2}{4\sin^2(\theta/2)}} = \frac{k_B T \ell_p}{\ell_0} \times 2\sin^2\left(\frac{\theta}{2}\right). \tag{7.6}$$

Segments in the chain are inextensible but as it is subject to brownian motion the fiber is never exactly straight. Straightening the chain requires energy which can be seen as an effective elastic energy. In the linear regime, for a segment of length ℓ_0 (Broedersz and MacKintosh (2014))

$$E_S(\ell) = \frac{90 k_B T \ell_p^2}{\ell_0^4} \frac{\Delta\ell^2}{2} \tag{7.7}$$

[1] For free hinges, curvature could be distributed along the whole unit meaning the bending energy for them will be slightly overestimated. However, their impact on the system is marginal.

where $\Delta\ell$ the elongation of the segment. If ℓ is the length of the elastic segment, elongation of the spring is $\Delta\ell = (\ell - \ell_0)$ and the elastic energy is

$$E_S(\ell) = \frac{90 k_B T \ell_p^2}{\ell_0^4} \frac{(\ell-\ell_0)^2}{2} = \frac{k_B T \ell_p}{\ell_0} \times \frac{90\ell_p}{\ell_0} \times \frac{1}{2}\left(\frac{\ell}{\ell_0} - 1\right)^2. \tag{7.8}$$

The full Hamiltonian of the system reads

$$\mathscr{H} = \frac{k_B T \ell_p}{\ell_0}\left[\sum_{edges\,(i,j)} \frac{90\ell_p}{\ell_0} \times \frac{1}{2}\left(\frac{\ell_{ij}}{\ell_0} - 1\right)^2 + \sum_{hinges\,(ijk)} 2\sin^2\left(\frac{\theta_{ijk}}{2}\right) + \sum_{dipoles\,i} \frac{F\ell_0^2}{k_B T \ell_p}\frac{\ell_i}{\ell_0}\right] \tag{7.9}$$

where the sum on edges runs on all rigid segments of the system. ℓ_{ij} is the distance between nodes i and j. Hinges denote all sets of three consecutive nodes that were aligned in the network initial configuration (even if they are not part of the same bond) and θ_{ijk} is the angle between the segments in the hinge (Fig. 7.3). Finally, in the sum on dipoles, ℓ_i is the distance between the two nodes forming the dipole.

We define an adimensional spring constant

$$\mu = \frac{90\ell_p}{\ell_0}, \tag{7.10}$$

an adimensional dipole magnitude

$$M = \frac{F\ell_0^2}{k_B T \ell_p} \tag{7.11}$$

and we set the energy scale

$$\frac{k_B T \ell_p}{\ell_0} = 1. \tag{7.12}$$

Finally, we define our springs to have a rest length $\ell_0 = 1$. With these definitions and conventions, the Hamiltonian reads

$$\mathscr{H} = \sum_{edges\,(i,j)} \frac{\mu}{2}\left(\ell_{ij} - 1\right)^2 + \sum_{hinges\,(ijk)} 2\sin^2\left(\frac{\theta_{ijk}}{2}\right) + \sum_{dipoles\,i} M\ell_i \tag{7.13}$$

7.1.3 Biologically Relevant Parameter Ranges

Actin filaments have a typical persistence length in the range of $\ell_p \sim 10\mu m$ (Gittes et al. (1993)). Mesh size defines how much coarse grained our model is. We are not willing to simulate every actin filament but we still want some degree of precision so we chose $\ell_0 \sim 0.1 - 1\mu m$, one to two orders of magnitude smaller than the typical cell radius. The adimensional spring constant is thus in the range

$$\mu \sim 10^2 - 10^3. \tag{7.14}$$

Energy cost is thus much larger for stretching than for bending. This comes from the fact that the length scale of our segments is much smaller than the persistence length of the actin

Table 7.1 – Model parameters. Parameters indicated with a star were never changed.

Symbol	Description	Range
ρ	network density	$0.5 - 1.0$
ρ_d	dipole density	$0.1 - 1.0$
ρ_a	anchor density	$10^{-2} - 10^{-1}$
μ	spring constant	$10^2 - 10^3$
M	force dipole magnitude	$0.1 - 10$
ℓ_0	network segment rest length	$1.0^\star$
d_t	dipole distance threshold	$2.0^\star$
ℓ_c	dipole cutoff distance	$10^{-4\star}$

filaments.

To set the range of the dipole magnitude, we use the critical buckling force. To estimate the critical buckling force, we compare the work of the dipole force F on the hinge to the bending energy for small deformations. The work as a function of the angle reads

$$W(\theta) = 4\ell_0 sin^2\left(\frac{\theta}{4}\right) \times F \tag{7.15}$$

Comparing this equation with the bending energy (eq. 7.6) for small angles yields a critical force

$$F_b = \frac{2k_B T \ell_p}{\ell_0^2}. \tag{7.16}$$

With our energy and length conventions (eqs. 7.12 and $\ell_0 = 1$), the adimensional buckling force is $M_b = 2$. We chose to take the adimensional dipole magnitude in a broad range around this value

$$M \sim 0.1 - 10. \tag{7.17}$$

In order to test the relevance of the critical buckling force, we can compare the order of magnitude of the buckling force of actin filaments predicted by our development to the force exerted by myosin during the power stroke. At room temperature, $k_B T \sim 4 \cdot 10^{-21} J$. This yields a critical force $F_b \sim 0.2 - 20 pN$ for a single actin filament. During the power stroke, a single myosin II exerts a force of about $4pN$ (Piazzesi et al. (2007)) which is in the middle of the computed range of critical buckling force.

Network density has great incidence on the rigidity of the system. Under a critical density $\rho \approx 0.45$, the system is disconnected and can be sheared without any cost (Broedersz et al. (2011)). We disregarded values of the network density under 0.5. Anchor density was kept low. A wide range of dipole densities was considered. Table 7.1 summarizes all parameters and the considered ranges.

7.1.4 Implementation and Simulations

The model was implemented in an original C++ program. The optimization scheme used to minimize energy in the system is (following Ronceray (2016)) the GNU scientific library (GSL) implementation of the Broyden-Fletcher-Goldfarb-Shanno (BFGS) algorithm. The program can be found on a GitHub repository (Messi et al. (2020)).

Simulations were conducted as follows. The system was initialized following the description given at section 7.1.1. An energy minimum was then found using the BFGS algorithm and the final configuration was recorded for analysis. In particular, force exerted on the anchors was measured.

For numerical stability, dipole force was chosen to vanish at short distances. For a distance ℓ between dipole nodes, force reads

$$F_d(\ell) = \begin{cases} M & if\ \ell > \ell_c \\ M\left(\frac{2\ell}{\ell_c} - 1\right) & if\ \frac{\ell_c}{2} < \ell < \ell_c \\ 0 & if\ \ell < \frac{\ell_c}{2} \end{cases} \tag{7.18}$$

with M the force dipole magnitude and $\ell_c = 10^{-4}$ the cutoff distance. Dipole energy is thus

$$E_d(\ell) = \begin{cases} M(\ell - \ell_c) + \frac{M\ell_c}{4} & if\ \ell > \ell_c \\ \frac{M}{\ell_c}\ell^2 - F\ell + \frac{M\ell_c}{4} & if\ \frac{\ell_c}{2} < \ell < \ell_c \\ 0 & if\ l < \frac{\ell_c}{2} \end{cases} \tag{7.19}$$

7.2 Results

After minimization, network area is smaller than in the initial state. Holes have formed in the bulk and fibers are clustered. At the periphery, fibers and dipoles align in what could be considered as rudimentary actomyosin bundles (Fig. 7.5 a). This can be highlighted in dense networks with high values of dipole force magnitude and/or dipole density. In very dense networks, fiber bundles form arcs between anchor points reminiscent of structures found in strong pulling cells like fibroblasts (7.5 c).

Averaging the force measured at anchors we created force maps similar to experimental stress maps (Fig. 7.5 b). High stress clusters form at the periphery of the system. The main purpose of this model was to assess the possibility to obtain force-distance relationships similar to our experimental results with a simple and fully mechanical description of the actin-myosin network and cell-substrate adhesions. In fact, simulations performed on a wide range of parameters yielded a force on anchors growing with distance. As observed in experiments, forces increase with distance from the center of the shape (Fig. 7.6 a).

The trend is robust. We investigated correlation between force and distance for several initial shapes and varying the model parameters. Correlation increases with dipole density (ρ_d) and magnitude of single force dipole (Figs. 7.6 b, 7.7). We also analyzed the relationship

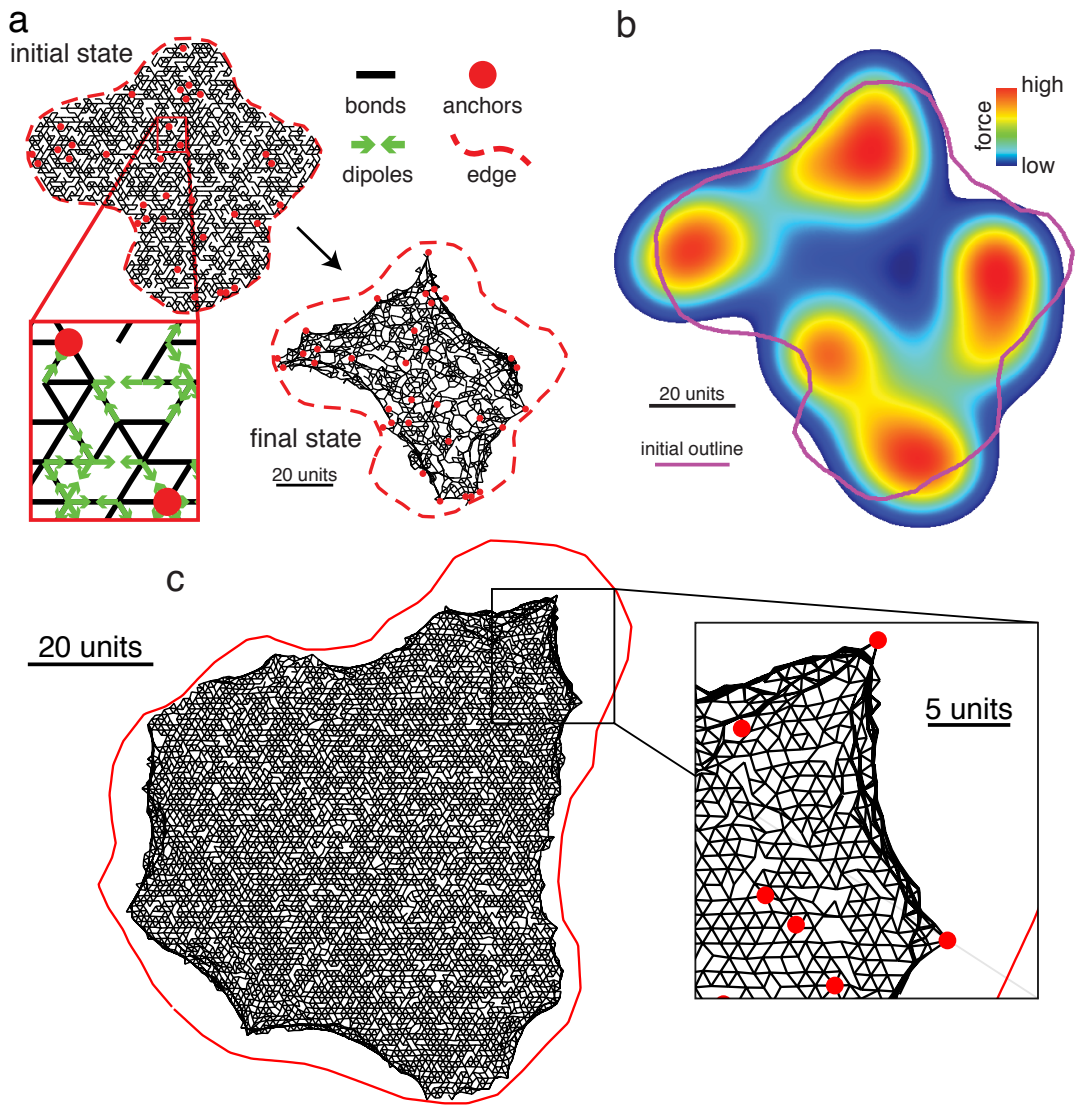

Figure 7.5 – Typical model simulation and stress map. (a) Initial and final state of a typical simulation. Black lines represent filaments and red circles the anchor points. Force dipoles (green arrows) are shown in a zoomed portion of the network (inset). Dashed red line is the initial outline of the system. (b) Reconstituted force map. Pink line shows initial system outline. To create force map, the system final state was mapped to a 2,048 by 2,048 pixel image with pixel values corresponding to the force magnitudes at anchor points, and the image was blurred and color coded (color scale is logarithmic). Parameters are network density $\rho = 0.6$, dipole density $\rho_d = 0.3$, anchors density $\rho_a = 0.2$, links spring constant $\mu = 512$, and magnitude of the dipole force $M = 4$. (a-b) Scale bar is 20 model-length units (5 times the length of a network hinge). (c) Formation of bundle-like arcs between anchors at the system periphery. Initial outline is shown in red. Parameters are $\rho = 0.9$, $\rho_d = 0.3$, $\rho_a = 0.2$, $\mu = 512$ and $M = 4$. Inset shows zoom on dense structure. Scale bar is 20 units for whole system and 5 for inset.

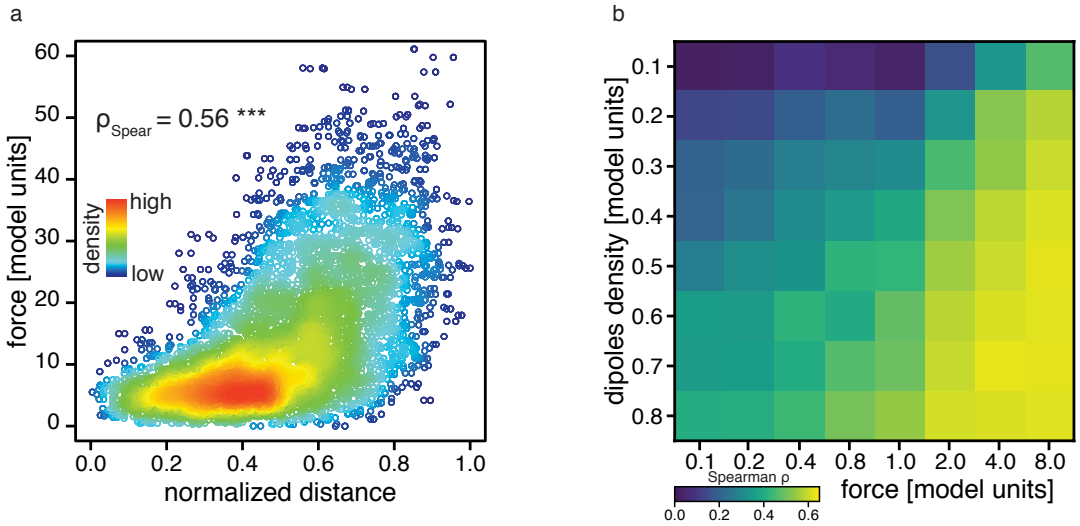

Figure 7.6 – Force-distance relationship. (a) Density plot of the force distance relationship (parameters $\rho = 0.7$, $\rho_d = 0.3$,$\rho_a = 0.02$, $\mu = 256$ and $M = 4$) for 11 different initial outlines (8 realizations for each outline). Distance to the system centroid after minimization was normalized by the maximal distance in each realization. Each data point corresponds to the force measured on a single anchor. Spearman rank correlation coefficient $\rho_{Spearman} = 0.56$, p-value $p < 10^{-3}$. (b) Mean Spearman rank correlation coefficient for force-distance relationships for different values of the parameters ρ_d and M. Other parameters are $\rho = 0.6$, $\rho_a = 0.02$ and $\mu = 512$. At least 10 realizations on one initial outline were averaged for each set of parameters.

with force normalized by force dipole magnitude. Interestingly, at a given distance, normalized force still grows for increasing values of M indicating force does not depend linearly on the dipole magnitude (Fig. 7.7, a).

Similarly to experimental results, force was generally oriented towards the system center. Absolute value of tangential component of the force also grew with distance but in a lesser significant way. There was no preferred direction; clockwise and counter clockwise components of the tangential force were fairly identical (Fig. 7.8, a). Mean force per anchor increased with the dipole force magnitude and decreased with the number of anchors in the system (Fig. 7.8 b).

To get more insight on the influence of the network density on the force the system could build, we analyzed the total force in the system normalized by the dipole magnitude for different network densities. Normalized total force displayed a biphasic relationship with the network density. Under the critical threshold network density ($rho_c \sim 0.45$), total normalized force in the system was generally low and does not scale with the increasing values of the dipole magnitude. As the network became denser, total force first increased, reached a maximal value or a plateau and decreased again for higher values of ρ (Fig. 7.8 c). Higher values of the dipole magnitude led to greater total force and network density yielding maximal force depended on the dipole magnitude. This results indicates there is an optimal network density for creating

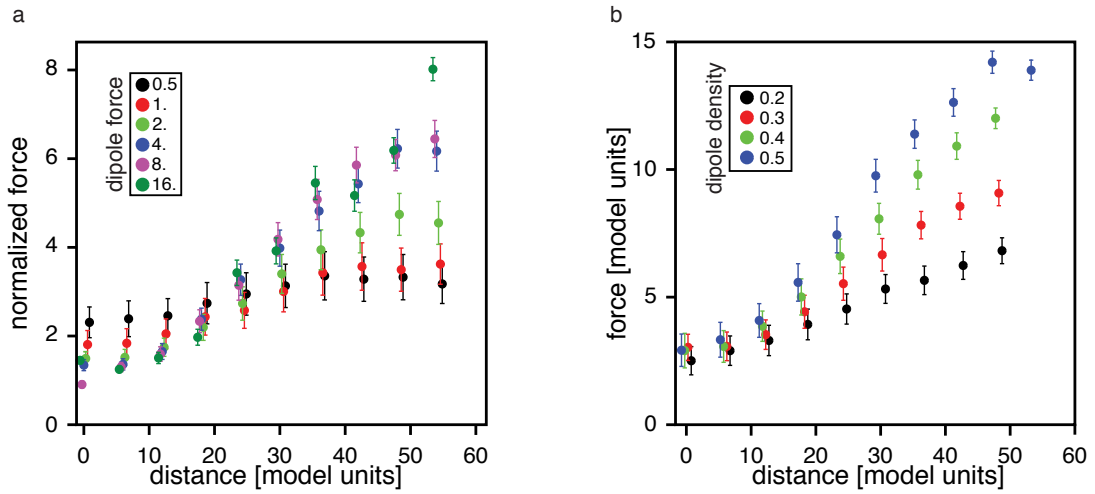

Figure 7.7 – Effect of model parameters of force-distance relationship. (a) Mean force at the anchors versus distance from the system centroid for different parameter values. Each data point is the average from 44 simulations (4 simulations made on each of 11 different initial outlines taken from experimental images). Parameters are network density $\rho = 0.6$, anchors density $\rho_a = 0.02$, and spring constant $\mu = 256$. (a) Dipole density is fixed at $\rho_d = 0.3$ and dipole force is varied. Force is normalized by magnitude of the force of one dipole M. (b) Magnitude of force dipoles is fixed at $M = 2$, and dipole density is varied.

forces in the network that depends on the force of active pullers.

Growth of force with distance from the center of the system could come from multiple sources. A rather simplistic consideration is that force is not balanced near the cell edge. In the bulk, force dipoles can be present on either sides of the anchors thus possibly compensating each other's contribution (Fig. 7.9 a). This geometrical argument would work even without any network deformation. However, network deformation could also play a role in building large forces. Formation of bundles of negatively curved aligned fibers (see Fig. 7.5 c) amplifies this geometrical factor and induces parallel stacking of many fibers and therefore to summation of the force exerted by active pullers (7.9, c).

In the cell, organization of the cytoskeleton, myosin and adhesions distributions are not random. Moreover contractile network and cell-substrate contacts constantly rearrange following intricate dynamics. Multiple mechanisms involving mechanical and chemical feedback control their spatial and temporal architecture. Yet, a simple elastic model featuring energy minimization in a homogeneous elastic network with random fixed points and dipoles was sufficient to reproduce experimental results. The model in this form does not take into account temporal dimension or preexisting inhomogeneity, yet force-distance relationship was observed for a wide range of model parameters. This result suggest that distance dependence of stress is an emergent property of such networks independent of network history. Nevertheless, we do not claim this model completely grasps the mechanism of force building in the cell. Other processes must affect the stress exerted by the cell on its substrate. In particular, the dynamics have until now been only skimmed. In section 5.1, we have seen that force clusters

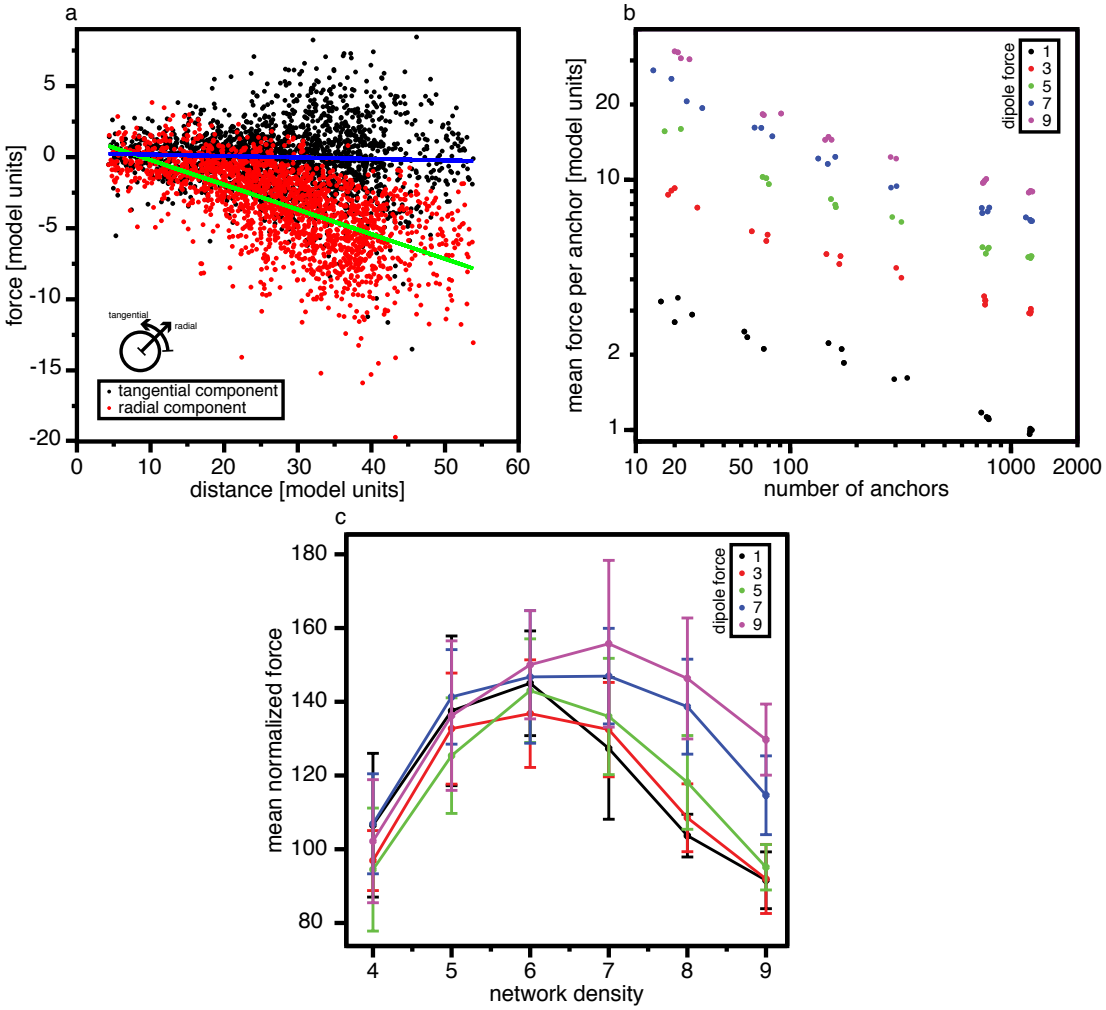

Figure 7.8 – Force-distance plots. (a) Radial component of the force is positive towards the exterior of the system, tangential component is positive in the counterclockwise direction. Negative radial force indicates force is directed towards the center of the system. Radial component and absolute value of tangential component of the force grow with distance from outline centroid. Tangential component is symmetrical at all distances. Parameters are $\rho = 0.9$, $\rho_d = 0.3$, $\rho_a = 0.02$, $\mu = 128$ and $M = 4$. Data aggregated from 8 simulations on a single shape. (b) Mean force per anchors as a function of the number of anchors for different values of the dipole magnitude. Parameters are $\rho = 0.6$, $\rho_d = 0.3$ and $\mu = 1024$. (c) Total force in the system normalized by dipole magnitude for different network densities. Parameters are $\rho_d = 0.3$, $\rho_a = 0.05$.

move during polarization and follow the cell edge. In the following chapter, we are going to leave the static picture. We will discuss parallel activity of the edge and traction forces.

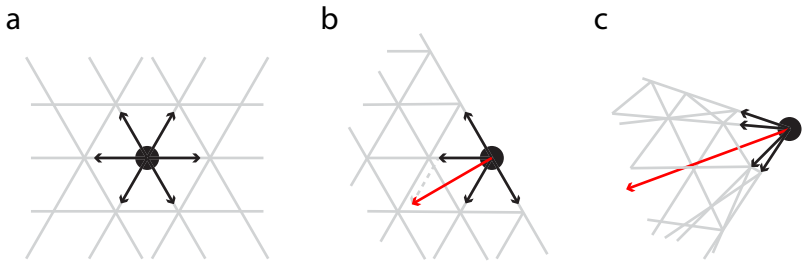

Figure 7.9 – Intuitive picture of growth of force. (a) In the bulk forces coming from every direction compensate each other. (b) Near the edge, there is only inward directed forces, so the resulting force is higher than for the bulk. (c) When the system deforms, alignment of fibers increases force amplification.

8 Dynamics

We have seen in the previous sections that stress exerted by cells grows with distance. Also, phenomenological results (Sec. 5.1) show that stress forms high level clusters located near the edge of protruding regions of the cell (Fig. 5.2 and 5.3). We have witnessed that these clusters form, grow and decline together with protrusion and retraction of the edge. These results suggest traction forces and edge activity are correlated. However, we have not yet assessed precise timing of stress increase and drop during the protrusion-retraction cycle. To get more insight into this correlation, we followed their evolution during multiple cycles and studied the dynamics of stress and edge position in time and space.

8.1 Stress During the Cycle

8.1.1 Stress Profiles

We measured stress in spreading cells during protrusion-retraction cycles. For this we used Traction force microscopy (TFM) sequences. To follow evolution of stress during the cycle, we first selected points on the cell outline that were constantly protruding for at least 1 minute and constantly retracting after the switch for at least 1 minute as well. From selected events, we extracted stress profiles on a ray (half line) originating from the center of the outline and passing by the outline point at the onset of retraction. We aligned events, with respect to the time of switch from protrusion to retraction and aligned profile origins. Finally, we averaged data for each time shift creating averaged stress profiles (Fig. 8.1 a). As the edge advances, stress grows and its maximum moves away from the cell center following the protruding edge. During retraction, stress goes down and maximum moves back inward. Interestingly, maximal stress is measured after onset of retraction. This behavior could be explained by the assembly of new adhesions during the edge advance and sliding of adhesions during its retreat. An interference reflection microscopy image of the edge during the cycle shows that close contacts between cell and substrate are maintained during edge retraction. During protrusion, a dark gray area follows behind the protruding edge and as retraction sets on, the area concentrates into darker foci that slide back with the edge (Fig. 8.1 b). This does not coincide with previous finding that edge retraction is preceded by decrease of traction stress

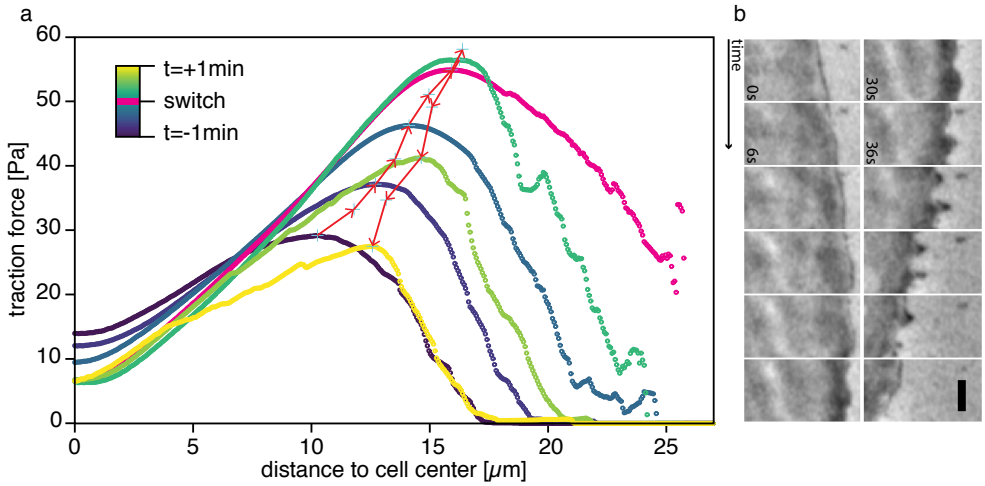

Figure 8.1 – Stress profiles and adhesions during protrusion-retraction cycle. (a) Mean radial stress as a function of the distance to the center of the cell. Profile corresponding to the first frame in retraction is shown in pink. Red arrows indicate stress maxima in each profile. Time interval between consecutive profiles $20s$. (b) Interference reflection microscopy of a cell region undergoing protrusion-retraction event. Dark parts corresponds to regions where cell is close to the substrate. Column on the right shows protrusion until onset of retraction, column on the left shows edge retraction. Scale bar $2mm$; time interval between frames $6s$

exerted by the cell (Barnhart et al. (2015)). Contrary to the idea that weakening of adhesion triggers the switch, this result suggest that adhesions persist and still transmit stress during the early stages of edge retraction. Later in the retraction phase, we have observed that stress does decrease, suggesting that adhesions are eventually released but not prior to the onset of retraction.

8.1.2 Stress and Edge Velocity

To obtain a more precise picture of the relationship between stress and edge dynamics, we studied their joint evolution in time and space. We analyzed the correlation between stress variation and movement of the edge. We used TFM assay data with cell outlines extracted from phase contrast images. It was done as follows. Let $\vec{x}(t)$ be a point on the cell outline at time t and $n(t)$ the normal to the edge at position $\vec{x}(t)$. We define a second point $\vec{x}(t+1)$ as the intersection n and the outline at time $t+1$. Edge displacement at time t is the difference between the two positions projected on the normal

$$\Delta x(t) = (\vec{x}(t+1) - \vec{x}(t)) \cdot \vec{n}, \tag{8.1}$$

where $\vec{n}$ is a unit vector along $n(t)$ directed outwards. Thus, positive variation means edge is protruding and negative that it is retracting. Stress is measured in an elongated rectangular window centered on $x(t)$. The long axis of the reference window is aligned with $n(t)$. Stress variation $\Delta\sigma(t)$ is defined as the difference in stress in the reference window between time t

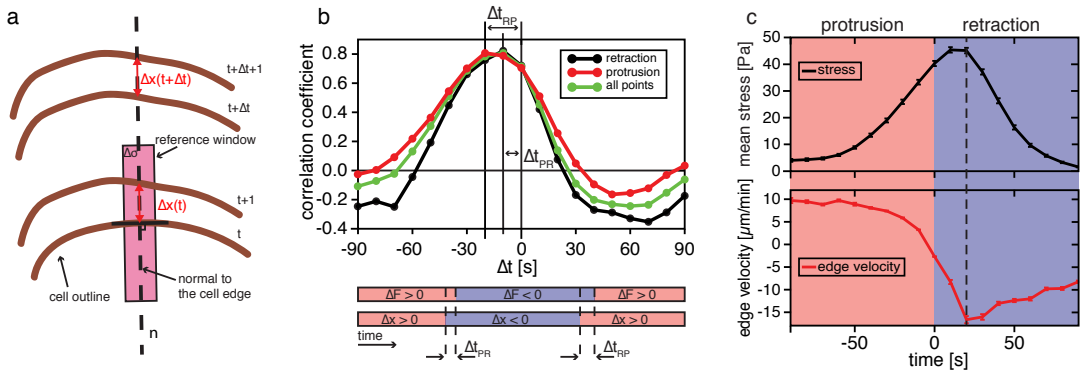

Figure 8.2 – Stress variation and edge velocity. (a) Sketch of Stress variation $\Delta\sigma$ is measured in the reference window (in red) between time t and $t+1$. Edge position variation Δx is measured between time $t+\Delta t$ and $t+\Delta t+1$.

and $t+1$. Finally, we define two other points $x(t+\Delta t)$ and $x(t+\Delta t+1)$ as the intersection $n(t)$ and the outline at time $t+\Delta t$ and $t+\Delta t+1$ respectively. Edge displacement at time $t+\Delta t$ is thus

$$\Delta x(t+\Delta t) = (\vec{x}(t+\Delta t+1) - \vec{x}(t+\Delta t)) \cdot \vec{n}. \tag{8.2}$$

An explanatory sketch can be found at Fig. 8.2 a. This procedure was repeated for all stress-displacement pairs for multiple sequences. With this, we defined a correlation function

$$C(\Delta t) = \frac{1}{N_{pair}} \sum_{N_{pair}} \frac{\Delta\sigma(t) \cdot \Delta x(t+\Delta t)}{|\Delta\sigma(t) \cdot \Delta x(t+\Delta t)|}. \tag{8.3}$$

In the sum, numerator is positive if stress increases at time t and edge is protruding at time $t+\Delta t$ or stress is decreasing and edge is retracting. Otherwise, contribution is negative. It emerged that this correlation peaks at $\Delta t = -10s$ (Fig. 8.2 b, top). The same correlation was computed distinguishing protrusion and retraction. We found that a time shift $\Delta t_{PR} = -20s$ gives the best correlation for protruding nodes and $\Delta t_{RP} = -10s$ for retraction. These results show that in general edge motion and stress variation are highly correlated. However, the small time shift indicates another interesting fact: when stress is increasing (resp. decreasing), it is likely that the edge was locally protruding (resp. retracting) a little while ago. More precisely, onset of protrusion (resp. retraction) precedes the change in stress. In particular, starts increasing 10 seconds after onset of protrusion and is still increasing 20 seconds after the switch from protrusion to retraction (Fig. 8.2 b, bottom).

Finally, we analyzed concurrent evolution of stress and edge velocity during the protrusion-retraction cycle. In a way similar to section 8.1.1, we selected protrusion-retraction events with $90s$ constant protrusion, followed by $90s$ constant retraction. We measured stress in a window as defined earlier. To compute edge velocity we used the definition of displacement given at equation 8.1 dividing it by the time $\delta t = 10s$ between two consecutive frames of the image sequence

$$v(t) = \frac{(\vec{x}(t+1) - \vec{x}(t))}{\delta t} \cdot \vec{n}. \tag{8.4}$$

The full protrusion-retraction cycle was analyzed (8.2 c). It followed that at the onset of protrusion, stress was generally low and protrusion rate was high. Then during protrusion, traction forces gradually increased while edge velocity decreased. At the onset of edge retraction, stress was still growing, consistent with our previous results. Interestingly, maximal stress and retraction speed were reached at the same time. After that, stress rapidly decreased and retraction speed as well.

Generally, our results show that stress follows precise dynamics during the protrusion-retraction cycle strongly correlated with movements of the cell edge. Timing between onset of retraction and drop in stress together with apparent sliding of cell-substrate contacts suggest that edge retraction is triggered by increase of traction force which causes adhesions to slide and eventually to detach. High stress foci near the tips of protrusions could originate from an intrinsic property of active contraction in fiber networks (Chapter 7, Ronceray (2016)) or from viscous friction between retracting cell structures and the extracellular matrix consistent with the molecular clutch picture (Bangasser et al. (2013)).

Sliding of adhesions likely destabilizes the surrounding actin network, including its parts distal from the adhesion, causing network to collapse and retraction of the whole edge. The fact that adhesions continue to transmit force at the onset of sliding is potentially significant because it means that the actin network remains under tension. This could facilitate building and stabilization of cytoskeletal structures, such as transverse actin arcs (Giannone et al. (2004), Burnette et al. (2011)). It might also promote formation of highly curved plasma membrane sites contributing to re-initiation of protrusion (Begemann et al. (2019)).

Our results match observations reported in a previous study where force dynamics during the protrusion-retraction cycles in fibroblasts were deduced from the patterns of actin flow (Ji et al. (2008)). Yet, it does not coincide with the idea that retraction is triggered by weakening of the adhesions at the cell edge (Barnhart et al. (2015)). However, it is important to note that there are significant differences in experimental procedures and observed cell behaviors between the latter work and our study. Indeed Barnhart et al. (2015) considered discoid cells on very compliant substrates ($1.5kPa$) that did not fluctuate prior to polarization. Polarization was triggered by a single retraction at the prospective rear. Fluctuating cells were excluded from analysis. In contrast, as described in chapter 5, our analysis was focused on rigid substrates ($16.7kPa$) with cells exhibiting protrusion-retraction fluctuations, which did not result immediately in polarization. On compliant substrates ($1.5kPa$ and $4.5kPa$) and in the presence of blebbistatin, we observed behaviors consistent with Barnhart et al. (2015). However, in addition to polarization with retraction at the rear, we also witnessed polarization by non-uniform protrusion at the front as reported in (Cramer et al. (2018)).

Traction-force induced retraction is likely not the only mechanism governing edge dynamics. Other mechanisms featuring signaling networks, actin assembly or membrane shape and tension might also play a role (Xiong et al. (2010), Dreher et al. (2014), Peleg et al. (2011)). For example, in blebbistatin-treated cells, edge retraction is likely caused by membrane tension (Fournier et al. (2010)). However, elongation and fragmentation of the cells in the presence of blebbistatin suggests that traction forces are necessary to confer distance sensitivity to the

retraction process, helping the cell to keep integrity and stable shape.

Our analysis was focused on fluctuating cells. However, lateral flanks of migrating keratocytes have a lot in common with protruding regions of fluctuating non-polarized cells. They have the same edge shape and dynamics. Sides of moving cells are curved regions furthest from the cell center where the vast majority of transition from protrusion to retraction are observed (Chapter 2, Raynaud et al. (2016)). Moreover, traction forces are similar. Large adhesion sites that correspond to highest traction stress regions (Fig. 5.1, Fournier et al. (2010), Oliver et al. (1999)) and that were reported to slide (Fournier et al. (2010)) are found in the flanks. Our analysis suggests that protruding segments in fluctuating cells and lateral flanks of migrating cells are analogous and that the mechanism governing local cell-edge dynamics based on traction force is the same during polarization and migration.

8.2 Actin Flow Does Not Follow the Same Dynamics as the Traction Force

After traction forces, behavior of actin flow during the protrusion retraction cycle drew our interest. In order to visualize the flow, we acquired sequences of polarizing cells injected with small amounts fluorescent phalloidin, a toxin that binds filamentous actin. Phalloidin sparsely binds F-actin creating traceable fluorescent speckles (Fig. 8.3 a). This technique is called *fluorescent speckle microscopy* (FSM). We analysed the sequences and, using a particle image velocimetry software (Venneman (2020)), we extracted flow velocity maps and analyzed them (Fig. 8.3 b, see also FSM description insection 4.2). As we did with traction forces we created kymographs of actin flow (Fig. 8.3 c). Consistent with previous reports, flow velocity was higher during retraction than during protrusion. But, it appeared that contrary to traction forces, flow rate did not depend on distance to the cell center nor change in time during protrusion. From the generated velocity maps we assessed distance dependence of the flow. We plotted flow velocity profiles from the center to the edge of the cell during protrusion, retraction and at the onset of retraction averaged from multiple protrusion-retraction cycles (Fig. 8.3 d). This analysis confirmed that retrograde flow speed was nearly constant and independent of distance to the cell center during protrusion and just after onset of retraction. During retraction, flow rate increased with distance just as traction forces suggesting that retraction happens by telescopic contraction of multiple units connected in series.

Traction forces are generated by actin network and could therefore be expected to depend on its motion. However, our results suggest that increase of traction forces with distance in the protrusion phase of the cycle is independent of the network motion. This provides further support to our elastic modeling approach described in the previous chapter. The ways actin network transmits stresses to the environment could be different between protrusion and retraction with retraction dominated by frictional slipping and protrusion - by elastic gripping. It has been reported that modes of force transmission may vary in different part of the cell (Fournier et al. (2010), Jurado et al. (2005), Gardel et al. (2008)) but the transition from one mode to the other was not investigated. Setting up an experiment allowing simultaneous

analysis of traction forces and actin flow would help addressing this question.

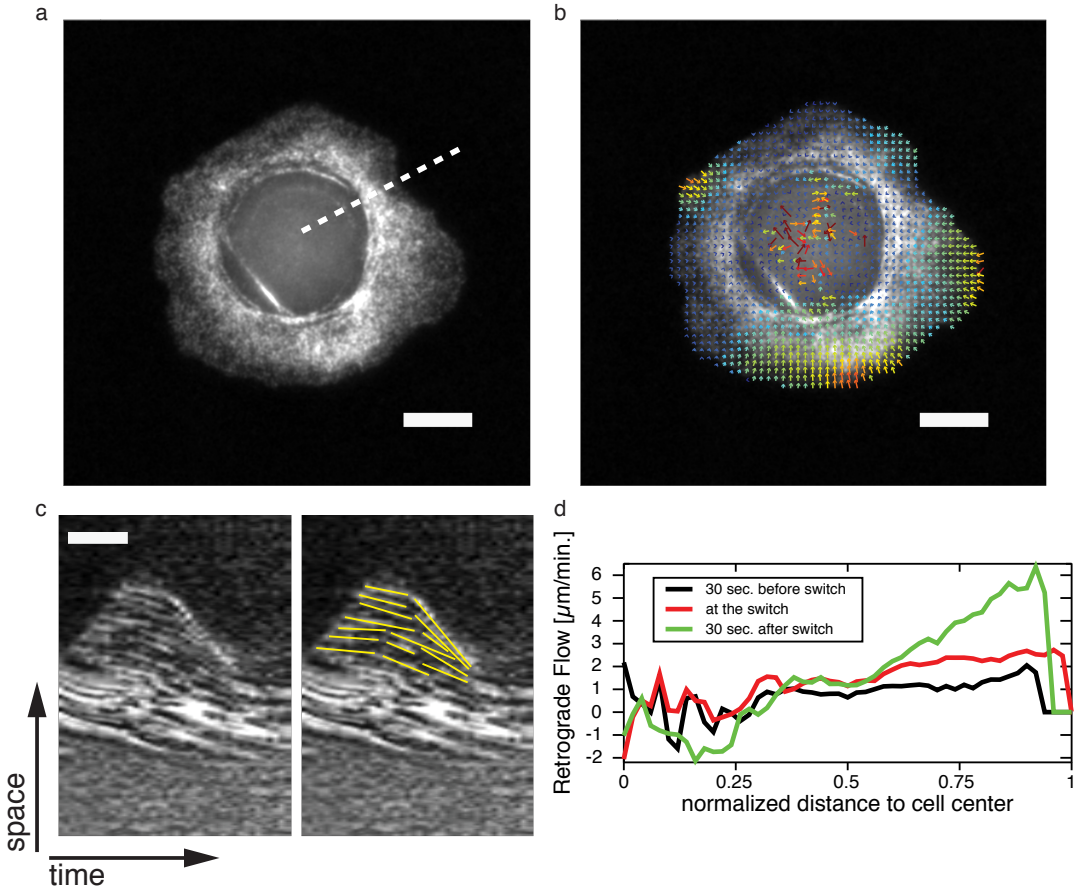

Figure 8.3 – Retrograde flow and edge velocity. (a) Fluorescent speckle microscopy image of a polarizing cell injected with Alexa-phalloidin. (b) Flow velocity map superimposed on the image. (c) Kymograph along the dashed line in (a). Actin speckle trajectories are marked in yellow in the image on the right to highlight the flow. Scale bar, $2\mu m$ and $50s$. (d) Mean actin flow velocity versus distance to the cell center at different times relative to the time of the switch from protrusion to retraction. The data are aggregated from 40 velocity maps. Scale bars, $20\mu m$ in (a and b).

9 Extension of the Model

In the previous chapters, we showed that a phenomenological rule based on distance can explain patterns of cell edge activity and is sufficient to reproduce spontaneous polarization. We also showed that stress increases with distance and initiates retraction suggesting that stress is the mediator of this distance-sensing mechanism. Finally, we reproduced stress dependence on distance with fully mechanical model. Next, we wanted to test if this model could be extended to reproduce self-organization of edge activity and polarization. In order to do this it is necessary to introduce dynamics in the model. We decided to extend the model by adding rules that simulate turnover of the cytoskeleton. Evolution of the system was achieved by performing consecutive steps of minimization and creation of new network. First a system was created and a minimal energy configuration was found. Then several nodes, bonds, dipoles and anchors were depleted and new network was added to the system. This was followed by a new energy minimization and the same procedure was repeated. Within the framework of energy minimization, it is not obvious how one can incorporate the notion of viscosity. For a sake of simplicity, we did not to introduce viscosity to the system and tested whether a fully elastic description with turnover could suffice to reproduce patterns of edge activity.

9.1 Moving Step by Step

As a proof of concept, we first only considered a part of the cell. The system was initially created in a circular sector. To coincide with the symmetry of the lattice we chose a central angle $\theta = \pi/3$ (i.e. a sextant). Let S denote the sector. Elastic fibers, anchors and dipoles were randomly created and distributed as previously described. In addition, anchors were placed on the two external radii of the sector. Those anchors were fixed and could not be removed. They were introduced to mimic attachment of the network, in the sector, to the cytoskeleton of the rest of the cell that was not simulated. These simulations started in the same way as in the static version of the model: the system was initialized inside the sector and a configuration of minimal energy was found using the optimization algorithm (Fig. 9.1 a, b).

After minimization, a depletion procedure was performed. Anchors subject to a force higher than a threshold F_{max} were removed (except for fixed anchors). F_{max} is a variable

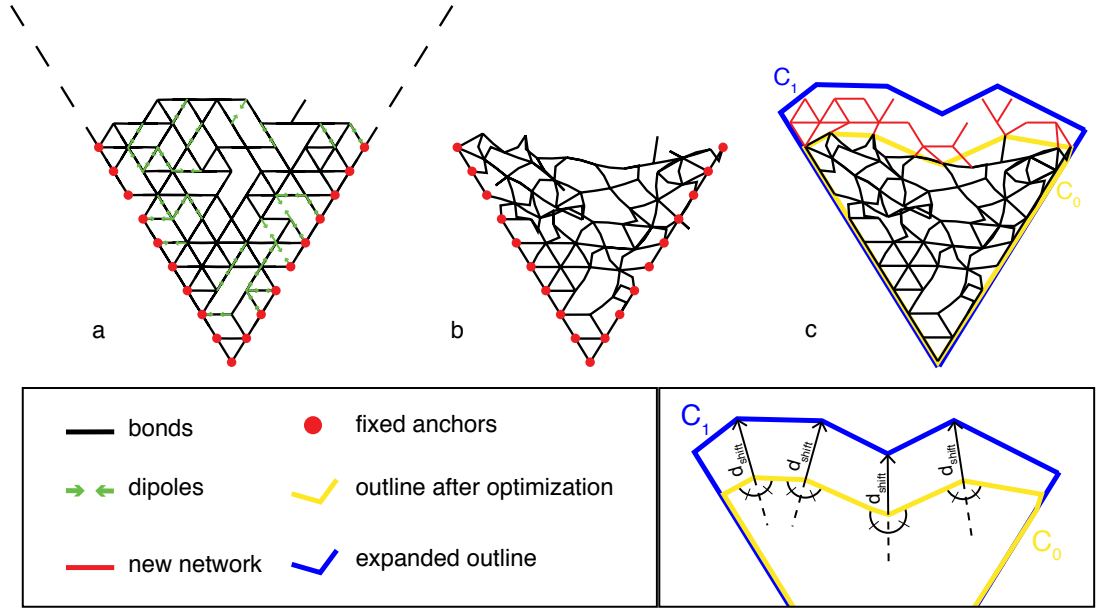

Figure 9.1 – Conduct of a step. (a) The system is initialized inside the sector S. Sector boundary is shown with a dashed black line. Fixed anchors (in red) are created on the radii of the sector. Other anchors are not shown. Dipoles are shown as pairs of green arrows (b) Configuration of minimal energy (c) Highly bent bonds are depleted and overlapping nodes are merged. Outline of the system C_0 is estimated (in yellow) and expanded in the direction of the sector C_1 (in blue). New network is created between the two outlines and attached to the existing one (in red). Inset shows expansion of the outline C_0 into C_1. Nodes are shifted of d_{shift} in the direction of the of the angle between two bonds.

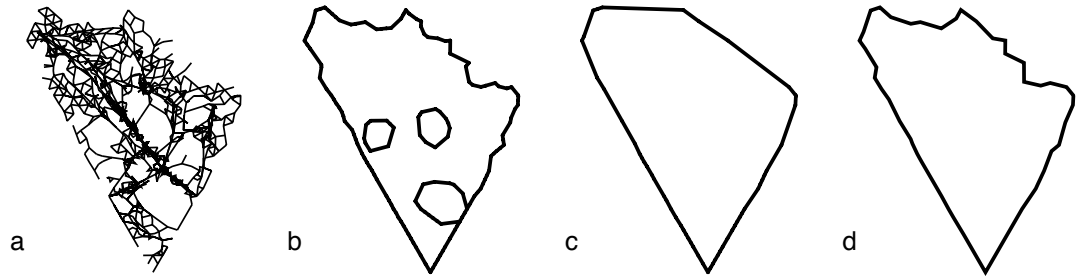

Figure 9.2 – Comparison of different outline segmentation methods. Finding the outline of a set of points is a good example of an intuitive task that is difficult to perform on a computer. (a) Final state of a system. Note that holes are present in the network bulk. (b) Segmentation with an alpha-shape, value of parameter $\alpha = 6.25$ which corresponds to a circle of diameter 5. Note that holes are present in the segmentation. (c) Segmentation with a convex hull. (d) Segmentation with the chosen method and parameter $T_d = 5$.

parameter of the extended model. Additionally, depletion of nodes, bonds and dipoles was set up to create turnover in the system. Highly bent bonds were deleted and overlapping nodes

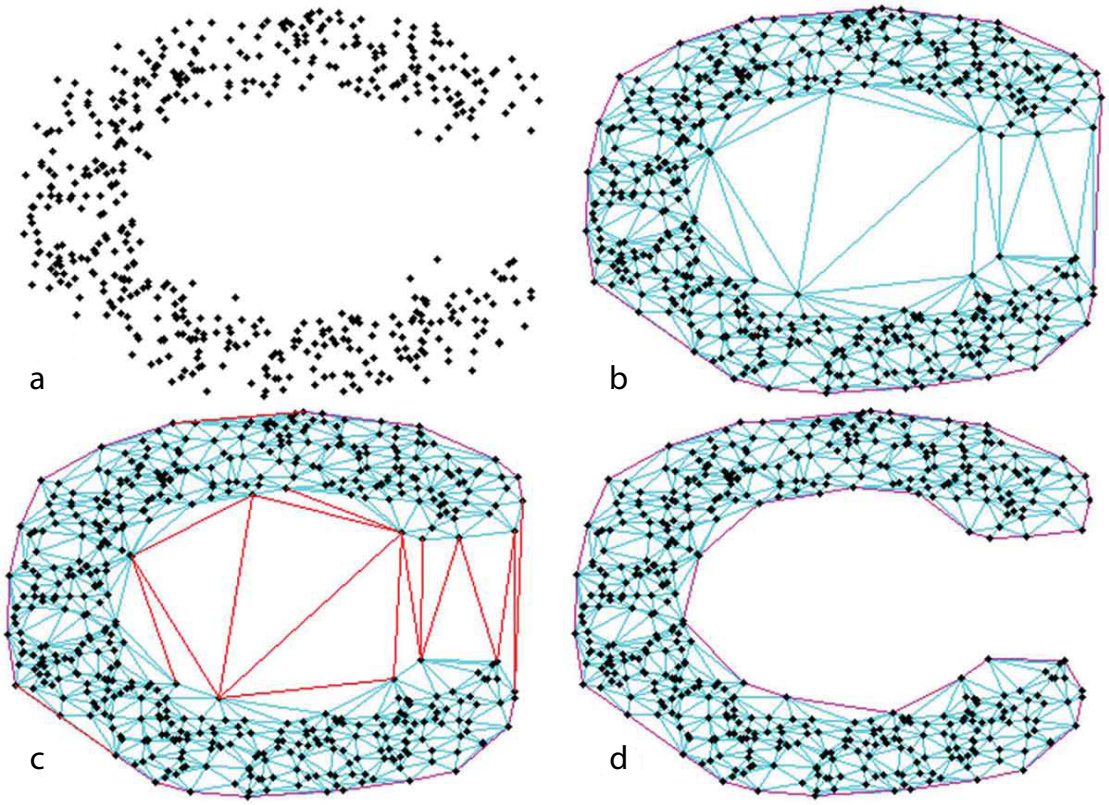

Figure 9.3 – Segmentation of the outline. (a) Set of points with concavities. (b) Delaunay triangulation is computed (in blue) and initial boundary is found by taking edges belonging to only one triangle (in red). Note that it correspons to the convex hull of the set. (c) Boundary edges longer than T_d are iteratively removed allowing concavities in the extracted shape. (d) Final outline. Picture taken from Awrangjeb (2016)

Table 9.1 – Additional model parameters. Parameters indicated with a star were never changed.

Symbol	Description	Range
F_{max}	anchors removal threshold force	$10-160$
θ	circular sector central angle	$\pi/3^\star$
N_b	maximal bonds for a node	$10^\star$
N_d	Fraction of displaced dipoles	$10\%^\star$ of the dipoles
d_{merge}	threshold distance for merging overlapping nodes	$10^{-3\star}$
$\theta_{deplete}$	threshold angle for depletion of bent bonds	$4\pi/5^\star$
T_d	Maximal length of a segment of the outline polygon	$\max(2d_{max},5)^\star$
d_{shift}	Shift of the outline	$4^\star$

were merged. Bonds were deleted if the angle between the two units exceeded $\theta_{deplete}$ and nodes were merged if they were closer than threshold distance d_{merge}. If deleted nodes were part of a dipole, those dipoles were also deleted. Nodes resulting from a merge kept dipoles from both "mother" nodes. In addition, if a node had more than a threshold number of bonds

N_b attached to it, bonds were randomly depleted until only N_b remained. In general, we set $N_b = 10$. Finally, N_d dipoles were randomly destroyed and recreated somewhere else in the system. We chose to set N_d as a fraction (10%) of the dipoles present in the system. Thus dynamic version of the model has several additional parameters associated with turnover of the system. Out of these parameters, we focused on the effect of F_{max} in the behavior of the system while keeping other parameters constant (Tab. 9.1).

Subsequent to depletion procedure, the outline of the minimal energy configuration was estimated. Let us call this outline C_0. Finding the outline of a set of points is a good example of an intuitive task that is difficult to perform on a computer. Anybody could find an outline for a given set of points. However, asking several people to complete this task would lead to slightly different outllines. A standard way of univoquely defining an outline for a set of points is by using methods based on Delaunay triangulation of the set. In general, the convex hull or an alpha shape is taken as the outline of the set. The term triangulation generally refers the decomposition of a polygon into a set of non-overlapping triangles. The triangulation of a set of point P is the decomposition of the convex hull of the set. Delaunay triangulation is a particular triangulation method of point sets defined such that for any triangle T of the triangulation DT of the set P, no point of P is in the circumcircle of T. It is frequently used in computational geometry because it has interesting properties and contains information about the set such as the position of nearest neighbours. In our case, neither the convex hull nor an alpha shaoe was optimal. Convex hulls do not account for concavities and alpha shapes could exclude holes in the bulk of the system (Fig. 9.2, 9.3). Instead, we used a method described in Awrangjeb (2016). We considered the system nodes as a set of points. First, Delaunay triangulation of the set is computed. Triangulation was performed with the computational geometry library CGAL (The CGAL Project (2020)). Every edge of a triangle inside a Delaunay triangulation is associated with exactly two neighbouring triangles except for triangles at the periphery of the set. For those, one edge is only associated with one triangle. The initial boundary is the set of edges that are associated with only one triangle. This happens to be the convex hull of the set. Second, for every point in the set, the distance to the nearest neighbor is measured. Let d_{max} be the maximal distance to the closest neighbor in the set[1]. This means, there is at least one point within a distance d_{max} of every point in the set. We set a threshold length $T_d \geq 2d_{max}$. To refine the segmentation and find concavities, edges of the boundary that are longer than T_d are removed iteratively from the outline (Fig. 9.3 c) and the final boundary with concavities is retrieved (Fig. 9.3 d). To avoid having a noisy outline, we generally used $T_d = \max(2d_{max}, 5)$. By construction, vertices of the outline C_0 are system nodes. (Tab. 9.1).

Outline C_0 was expanded into outline C_1. This was done by shifting outline vertices of a distance d_{shift} in the direction of the bisector of the angle between two bonds (Fig. 9.1 c inset). A new network of elastic fibers was created between the minimal energy configuration outline and the expanded outline inside the sector. In other words, the new network was created in $(C_1 - C_0) \cap S$. The new fibers were linked to the already existing network forming an

[1] N.B. d_{max} is not a model parameter, it is measured at the end of energy minimization.

expanded network. Note that the bonds between the old and new network may have initial length different from the normal bond length. To avoid any prestress, we set the rest length of these bonds to their initial length. After that, dipoles and anchors were added to the system in order to keep their density constant. Finally, the expanded network served as a new initial configuration for the energy minimization procedure (Fig. 9.1 c). A list summarizing all new model parameters and their values can be found at table 9.1.

9.2 Results

9.2.1 Phenomenological Description

Simulations of about 100 steps were run starting with a system initialized in sector of radius 20. For a wide range of values of dipole magnitude M and anchor removal threshold force F_{max}, after a fast and isotropic system expansion in the early steps (about 10), growth slowed down and the systems started displaying alternative growth and shrinking similar to protrusion-retraction cycles (Fig. 9.4 a). Expansions and size reductions could be isotropic or not (Fig. 9.4 a, e). In figure 9.4 a, the system had grown in all directions within the sector with nearly the same speed until $t = 29$, then, the right part of the system collapsed while the left part continued growing ($t = 41$). At t=60, the collapsed part had regrown and the system reached its maximal extension before rapidly shrinking isotropically ($t = 64, 71$). Finally a new growth phase started. A plot of maximal extension in different regions of the system suggests that the second retraction started from the left of the system before spreading to the whole system (9.4 e). Retraction on the left side of the system also set on before maximal extension was reached but it accelerates dramatically when the whole system started to collapse (between $t = 64$ and $t = 71$). For low value of dipole force ($M \sim 1-2$) the system grew steadily (Fig. 9.4 b, f). In this case, no significant retraction of the full system was observed.

During simulations, the network displayed important reorganization (Fig. 9.4 a-d). Nodes were observed moving generally from the sides towards the center of the system and from the top towards the bottom (Fig. 9.4 d) except for the part located in the initial sector that remained fixed throughout the runs (Fig. 9.4 a inset). Dense and elongated fiber structures formed away from the edge accross the system (Fig. 9.4 c, d). These structures were oriented either tangentially (Fig. 9.4 c) or radially (Fig. 9.4 d) similar to actin transverse arcs and stress fibers. Radial fiber structures were mostly observed with strongly pulling dipoles ($M \geq 6$). Bundle-like structures were stable for several steps (Fig. 9.4 c, d) . They attracted surrounding nodes and moved like single nodes but more slowly. Some of them merged. In general, they eventually collapsed concurrently to large system retractions (Fig. 9.4 d).

Addition of a turnover mechanism to our mechanical model produces oscillating systems.

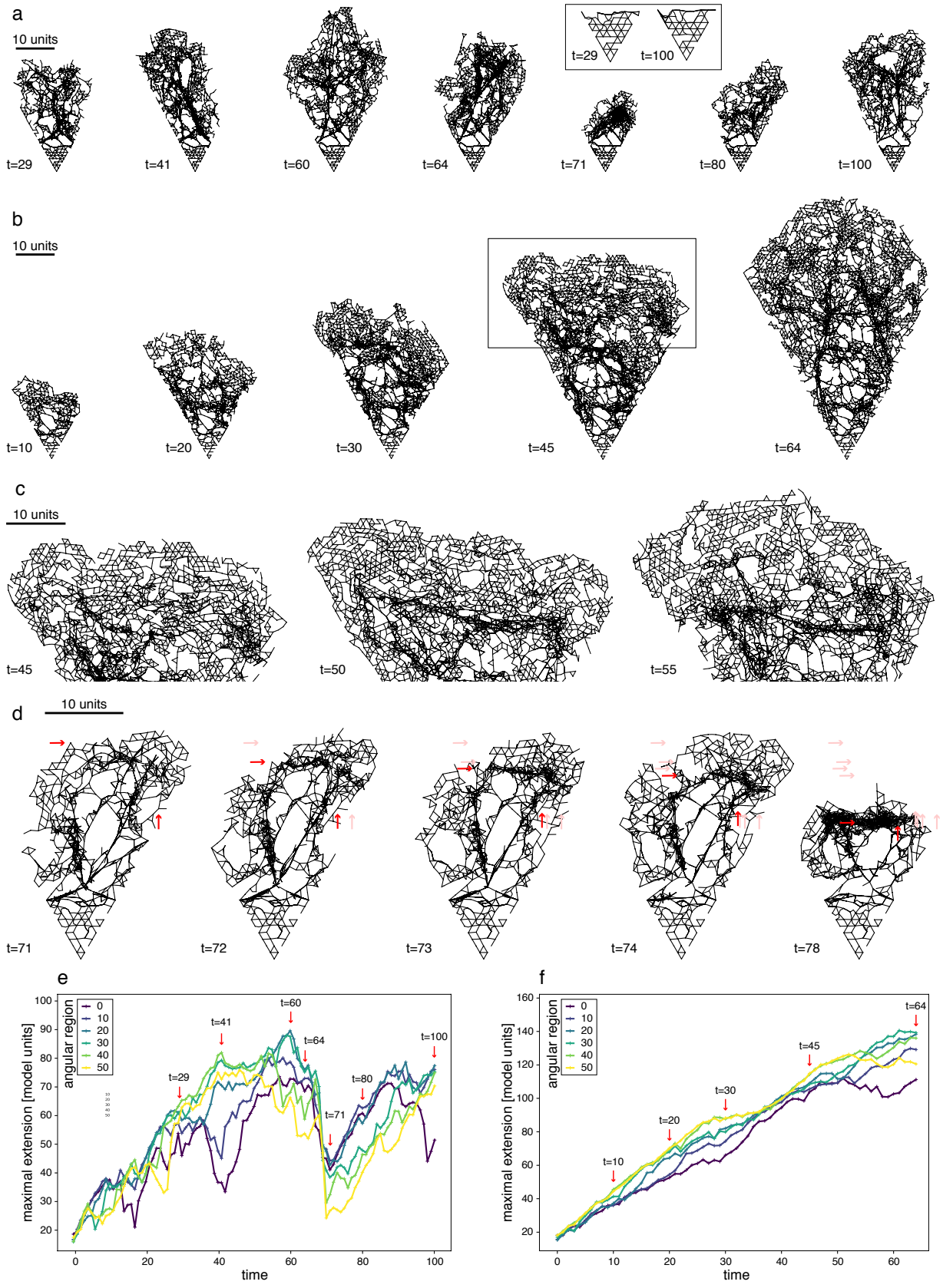

Figure 9.4 – System evolution during simulations. Legend on the next page.

Figure 9.4 – System evolution during simulations. (a-d) Snapshots from simulations. Unchanged model parameters are $\rho = 0.7$, $\rho_d = 0.2$, $\rho_a = 0.02$, $\mu = 1024$. Scalebar indicates 10 model units of length. Time step is indicated on the bottom left for system configuration. (a) Growth and shrinking of the system. The system grows isotropically until step $t = 29$. Then the right part collapse while the rest of the system continues to grow ($t = 41$). At $t = 50$, the system reaches its maximal extension and starts shrinking ($t = 64, 71$) and starts growing again. Inset shows a comparison of the bottom of the system for the first and the last displayed snapshots. Dipole force is $M = 3$ and anchor removal threshold force is $F_{max} = 20$. (b) For small values of dipole magnitude, the system grows steadily. Dipole force is $M = 1.5$ and anchor removal threshold force is $F_{max} = 20$. Rectangle at $t = 45$ indicates the zone shown in (c). (c-d) Dense actin structures form away from the edge resembling transverse arcs and stress fibers. (c) For low dipole forces, dense fiber structures are mostly tangential. Snapshots are taken from the same simulation as (b). (d) With high dipole force ($M = 6$), radial structures form. Red and light red arrows indicate respectively current and previous position of two nodes, one on the top of the system travelling from the top to the bottom of the system and one on side travelling towards the interior of the system. Anchor removal threshold force is $F_{max} = 40$. (e-f) Maximal extension as a function of steps. Extension was measured in 6 non-overlapping sectors of 10°. Time steps used for the snapshots in (a) and (e) are indicated with labeled red arrows (e) Corresponds to the same sequence as (a). Between $t = 29$ and $t = 41$, first collapse of the right side of the system and concurrent growth of the rest of the system is visible. Between $t = 60$ and $t = 71$ second isotropic retraction of the system is visible followed by regrowth of the system. (f) Corresponds to the same sequence as (b). The system grows steadily.

9.2.2 Analysis

To get more insight into the extended model, we analyzed characteristics of the system that are translatable to real cells. We first tested whether the new model still displayed distance dependence of the force as observed in experiments and in the static form of the model. Then, we assessed the range of parameters in which oscillations appeared and the effect of parameters on the size of the system. Finally, we addressed the movement of nodes and lifetime of anchors to compare them respectively with actin retrograde flow and adhesion turnover. For these analyses, we focused on the effects of dipole magnitude M and anchor removal threshold force F_{max}. We considered $M = 1 - 12$ and $F_{max} = 10 - 160$.

Depletion of parts of the system and addition of new network did not impair the force-distance relationship. As for the static version of the model, the new version displayed correlation between force and distance from the origin of the sector (Fig. 9.5 a). Strength of the correlation depended on the dipole magnitude. For low dipole magnitude, force did not depend on the distance. With growing magnitudes, steepness and intercept of the relationship increased until the mean force on anchors was above threshold for all anchors outside of the initial sector (Fig. 9.5 a). Interestingly, at fixed dipole magnitude, systems with higher value of anchor removal threshold also displayed steeper force-distance relationships (Fig. 9.5 b). This result could be related to the fact that cells with stable substrate adhesions like fibroblasts generate stronger forces than cells with weaker adhesions like keratocytes (Parsons et al. (2010), Kaverina et al. (2002)).

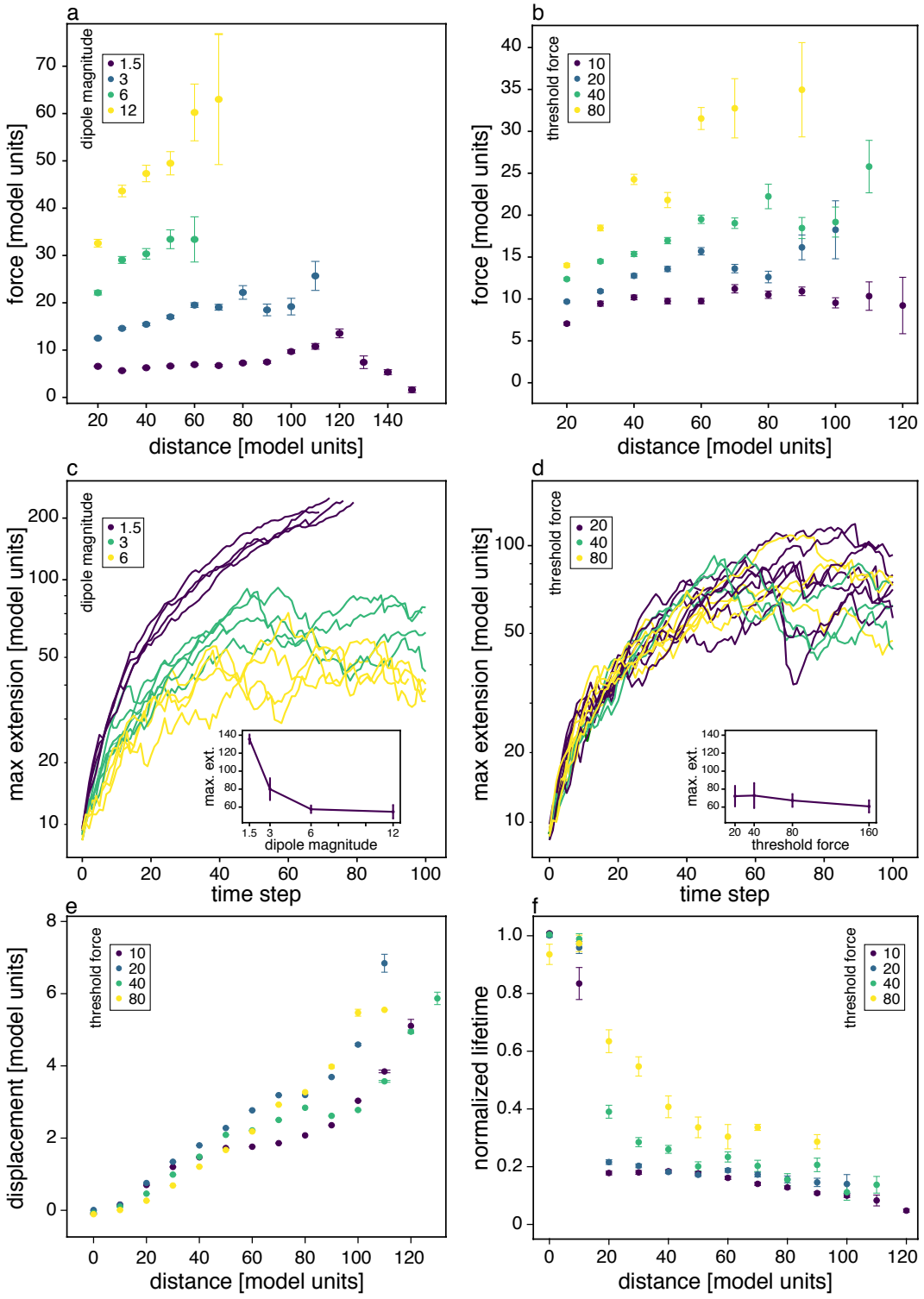

Figure 9.5 – Effect of parameters on the system characteristics and evolution. Legend on the next page.

Figure 9.5 – Effect of parameters on the system characteristics and evolution. (a-b) Force-distance relationship. (a) Different dipole magnitudes lead to different steepness in the force-distance relationship. Anchor removal threshold force was set to $F_{max} = 40$. Note that for $M = 12$ the mean force at distances higher than 20 are on average larger than the threshold. (b) Anchor removal threshold force also impacts the correlation between force and distance. Dipole magnitude was set to $M = 3$. (c-d) Maximal extension as a function of the step for multiple runs and different parameters. (c) Maximal extension depends on the dipole magnitude. Runs on the weakest magnitude ($M = 1.5$) have been stopped when the time to complete a single step exceeded a day. Anchor removal threshold force was set to $F_{max} = 40$. Inset shows mean maximal extension for different dipole magnitudes. Extension was averaged after 40 steps to allow the system to reach a steady state. Note that the value for $M = 1.5$ is likely underrated. (d) Parameter F_{max} does not influence the maximal extension of the system. Inset displays mean maximal extension for different threshold forces. (e) Mean displacement of the nodes during a single step grows as a function of the distance. Dependence on F_{max} is less trivial. Dipole magnitude was set to $M = 3$. (f) Lifetime of an anchor depends on the distance to the origin of the sector and increases for increasing values of F_{max}. (a-e) Other parameters are $\rho = 0.7$, $\rho_d = 0.2$, $\rho_a = 0.02$, $\mu = 1024$. Errorbars denote the standard error on the mean.

Next, we investigated evolution of the maximal extension of the system during simulations. At fixed F_{max}, dipole force had a strong impact on the maximal extension of the system. Simulations with low dipole force ($M = 1-2$) grew indefinitely (Fig. 9.4 b, f, and 9.5 a). For higher forces ($M \geq 3$), the system displayed oscillations (Fig. 9.5 a). We observed that systems with weaker dipoles had greater mean maximal extension than stronger ones (Fig. 9.5 a, inset). Frequency and amplitude of the oscillations also appeared to depend on M. Higher forces led to higher frequency and lower amplitude oscillations. However, limited run time of simulation did not allow for detailed analysis of the oscillations' frequency and amplitude. These results could be related to experiments with cells having different contractilities. When myosin contractility was inhibited with blebbistatin, keratocytes did not exhibit protrusion-retraction cycles and extended uncontrollably upon polarization (Chs. 6, 2 and Raynaud et al. (2016)). In control conditions, keratocytes displayed large oscillations of their edge while strong pulling cells like fibroblasts are reported to display small protrusion-retraction patterns (Parsons et al. (2010)). At fixed dipole force, we did not observe significant change in mean maximal extension over the considered range of values of F_{max} (Fig. 9.5 d inset). These results are more difficult to interpret. It appears that, in the considered range of parameters, the system is always able to create strong forces rapidly and detach anchors before growing in size. Note that anchors are depleted only after energy minimization. Thus, even if an anchor is removed at the end of a step, the network will not retract close to it, the edge will advance and possibly a new anchor will be placed in the newly formed network. In contrast to our simulations, it was shown experimentally that size of the cell correlates with adhesion strength (Barnhart et al. (2011)). However, a more detailed assessment with a wider range of the model parameters should be performed.

Finally, we tested characteristics inherent to the fact that the system evolves in time. We measured the mean displacement of nodes as a function of the distance. The displacement of the nodes was obtained by measuring their positions before and after energy minimization. We plotted the displacement as a function of the distance to the sector origin of the nodes' initial position ((Fig. 9.5 e). The model reproduced patterns of retrograde flow observed in experiments during retraction (Sec. 8.2). For all values of F_{max}, nodes away from the origin of the system moved more rapidly than closer nodes. Increase of velocity of motion with distance is expected for a system composed of multiple contractile units connected in series and was also recently observed in disordered actomyosin networks (Linsmeier et al. (2016)). We measured the mean lifetime of anchors as function of the distance to the origin of the sector for different values of the anchors removal threshold (Fig. 9.5 f). It follows that the anchor lifetime decreases with distance and increases with F_{max}. This results parallels adhesion dynamics observed in experiments. Near the cell edge, nascent adhesions turn over rapidly while mature adhesions located deeper in the cell are more stable (Parsons et al. (2010), Kaverina et al. (2002)). The fact that anchors have generally longer lifetime at higher F_{max} is intuitive. The higher the threshold, the more time the system will need to create forces high enough to detach anchors. It is also possible to compare this results to experimental observations. Strong adhering cells that do not exhibit fast shape changes (e.g. fibroblasts and endothelial cells) have low adhesion turnover rate while cells that move rapidly and have weaker substrate adhesions like keratocytes or B16 cells display fast turnover (Ch. 5 and Kaverina et al. (2002)).

In summary, the dynamic version of the model with simple rules for cytoskeletal turnover and addition of new network produces oscillating systems reminiscent of fluctuating cells (Fig. 9.4). The model reproduces other elementary features like force-distance relationship, force-dependent size of the system, retrograde flow and distance-dependent adhesion lifetime (Fig. 9.5). However, it is still a work in progress. The above results were obtained with a limited number of simulations. In the future, broader parameter ranges would be considered and we would explore the effect of other model parameters. It would also be interesting to test implementation of other rules. For example, we observed in experiments that actin polymerization seems to stop for a certain time during edge retraction. Extension of the system could depend on how much the edge retracted in the last minimization step. Another feature, that could also be added to the static model, is an elastic response of the anchors to force. For now, the anchors are immobile. We could instead model them as springs as it was done in recent extension of the original model (Ronceray et al. (2019)). Impact of the geometry of the original sector could be investigated. Size and angle of the sector could be changed or we could study other geometries (e.g. sector with flat or semi-circular bottom). Finally, the present implementation of the model limits the run length. Time of minimization steps grows exponentially with the size of the system. An optimized implementation would allow the longer runs. Finally, we would run simulations not in a sector but with a full cell as in the static version of the model and assess the capacity of such system to polarize.

10 Conclusion and Outlook

In this work, we addressed the mechanism underlying organization and patterning of cell-edge activity. We tested a hypothesis that traction force could be the mediator of distance sensing and a trigger for protrusion-retraction switches. To do so, we analyzed traction force dynamics during keratocyte polarization using traction force microscopy. With a numerical model, we reproduced experimentally observed results. Overall we have found that:

- During protrusion-retraction cycles, distribution of stress is highly dynamical and follows the motion of the cell-edge.
- Stress is necessary to organize cell-edge activity during migration and sufficient to induce edge retraction.
- Stress is correlated with the distance from the cell center locally in individual cells as well as on average in cell populations under different experimental conditions.
- Distance dependence is an emergent property of elastic fiber networks that can be reproduced with a simple mechanical model.
- Temporal dynamics of stress correlate with dynamics of the cell-edge during protrusion-retraction cycles suggesting that traction forces trigger onset of edge retraction.
- Stress continues to increase for a short time after onset of edge retraction indicating that adhesions continue to transmit force to the substrate in the early stages of retraction and therefore edge retraction is not triggered by a decrease in adhesion strength.
- Actin retrograde flow correlates with stress during retraction but not during protrusion suggesting that increase of stress during protrusion is independent of the motion of the actin network.
- Extended mechanical model including mechanism for cytoskeleton turnover reproduces patterns of protrusion-retraction and other features observed in experiments.

Overall our results constitute a strong evidence that traction forces mediate edge activity but they also raised new questions. Analysis of actin retrograde flow during protrusion-retraction

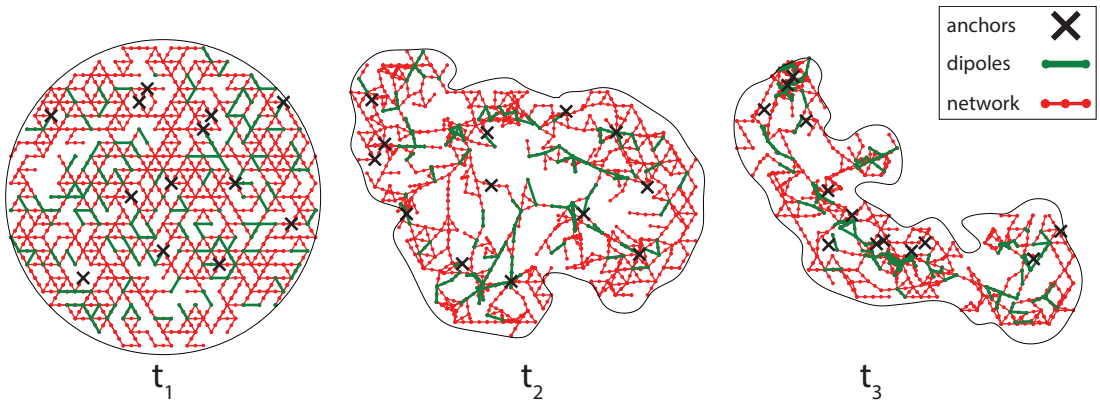

Figure 10.1 – Preliminary result of simulations of the extended mechanical model with a full cell. Network configurations after 0, 10 and 19 simulation steps. Parameters are $\rho = 0.6$, $\rho_d = 0.1$, $\rho_a = 0.03$, $M = 2$, $\mu = 256$, $F_{max} = 8$. Radius of the initial system configuration is 20.

cycle suggests that the way force is transmitted to the substrate is different between protrusion and retraction. However, in our experiments, actin flow and traction forces were measured separately and only their averaged behavior were compared, leaving the possibility that local correlation between stress and flow could have been lost in the averaging process. In the future, we will analyze the force-transmission modes in protrusion retraction cycle by combining traction force microscopy and visualization of actin flow. In order to do this we will use epidermal keratocytes from Zebrafish genetically modified to express fluorescent actin marker. As for the dynamic version of the model, it remains largely unexplored. We intend to perform a full analysis of the effect of model parameters on the system's behavior, test other rules (e.g. geometry of the initial sector, anchors acting as springs instead of firmly attached to the substrate). Finally, we would like to address the possibility of simulating a full cell (Fig. 10.1). We would test whether this model is sufficient to reproduce the entire polarization process. If not we would look for possible modifications of the model e.g. exploring the possibility of introducing feedback between motion and turnover in the system and/or elements of viscosity.

Bibliography

Adler, Y. and Givli, S. (2013). Closing the loop: Lamellipodia dynamics from the perspective of front propagation. *Phys. Rev. E*, 88:042708.

Alexandrova, A. Y., Arnold, K., Schaub, S., Vasiliev, J. M., Meister, J.-J., Bershadsky, A. D., and Verkhovsky, A. B. (2008). Comparative dynamics of retrograde actin flow and focal adhesions: Formation of nascent adhesions triggers transition from fast to slow flow. *PLOS ONE*, 3(9):1–9.

Allard, J. and Mogilner, A. (2013). Traveling waves in actin dynamics and cell motility. *Current Opinion in Cell Biology*, 25(1):107 – 115. Cell architecture.

Alt, W., Brosteanu, O., Hinz, B., and Kaiser, H. W. (1995). Patterns of spontaneous motility in videomicrographs of human epidermal keratinocytes (hek). *Biochem Cell Biol*, 73(7-8):441–459.

Álvarez-González, B., Meili, R., Bastounis, E., Firtel, R. A., Lasheras, J. C., and del Álamo, J. C. (2015). Three-dimensional balance of cortical tension and axial contractility enables fast amoeboid migration. *Biophysical Journal*, 108(4):821 – 832.

Ambühl, M., Brespant, C., Meister, J.-J., Verkhovsky, A. B., and Sbalzarini, I. (2012). High-resolution cell outline segmentation and tracking from phase-contrast microscopy images. *Journal of Microscopy*, 245(2):161–170.

Ananthakrishnan, R. and Ehrlicher, A. (2007). The forces behind cell movement. *Int J Biol Sci*, 3(5):303–317.

Arai, Y., Shibata, T., Matsuoka, S., Sato, M. J., Yanagida, T., and Ueda, M. (2010). Self-organization of the phosphatidylinositol lipids signaling system for random cell migration. *Proceedings of the National Academy of Sciences*, 107(27):12399–12404.

Awrangjeb, M. (2016). Using point cloud data to identify, trace, and regularize the outlines of buildings. *International Journal of Remote Sensing*, 37(3):551–579.

Bangasser, B. L., Rosenfeld, S. S., and Odde, D. J. (2013). Determinants of maximal force transmission in a motor-clutch model of cell traction in a compliant microenvironment. *Biophysical Journal*, 105(3):581 – 592.

Barnhart, E., Lee, K.-C., Allen, G. M., Theriot, J. A., and Mogilner, A. (2015). Balance between cell-substrate adhesion and myosin contraction determines the frequency of motility initiation in fish keratocytes. *Proceedings of the National Academy of Sciences*, 112(16):5045–5050.

Barnhart, E. L., Lee, K.-C., Keren, K., Mogilner, A., and Theriot, J. A. (2011). An adhesion-dependent switch between mechanisms that determine motile cell shape. *PLOS Biology*, 9(5):1–19.

Barr, V. A. and Bunnell, S. C. (2009). Interference reflection microscopy. *Curr Protoc Cell Biol*, Chapter 4:Unit 4.23.

Bear, J. E., Svitkina, T. M., Krause, M., Schafer, D. A., Loureiro, J. J., Strasser, G. A., Maly, I. V., Chaga, O. Y., Cooper, J. A., Borisy, G. G., and Gertler, F. B. (2002). Antagonism between ena/vasp proteins and actin filament capping regulates fibroblast motility. *Cell*, 109(4):509 – 521.

Begemann, I., Saha, T., Lamparter, L., Rathmann, I., Grill, D., Golbach, L., Rasch, C., Keller, U., Trappmann, B., Matis, M., Gerke, V., Klingauf, J., and Galic, M. (2019). Mechanochemical self-organization determines search pattern in migratory cells. *Nature Physics*, 15(8):848–857.

Blaser, H., Reichman-Fried, M., Castanon, I., Dumstrei, K., Marlow, F. L., Kawakami, K., Solnica-Krezel, L., Heisenberg, C.-P., and Raz, E. (2006). Migration of zebrafish primordial germ cells: A role for myosin contraction and cytoplasmic flow. *Developmental Cell*, 11(5):613 – 627.

Bohnet, S., Ananthakrishnan, R., Mogilner, A., Meister, J.-J., and Verkhovsky, A. B. (2006). Weak force stalls protrusion at the leading edge of the lamellipodium. *Biophysical Journal*, 90(5):1810 – 1820.

Bornert, A. (2016). *Protrusion-retraction switches and traction forces in spontaneous cell polarization*. PhD thesis, EPFL.

Breitsprecher, D. and Goode, B. L. (2013). Formins at a glance. *Journal of Cell Science*, 126(1):1–7.

Bretschneider, T., Anderson, K., Ecke, M., Müller-Taubenberger, A., Schroth-Diez, B., Ishikawa-Ankerhold, H. C., and Gerisch, G. (2009). The three-dimensional dynamics of actin waves, a model of cytoskeletal self-organization. *Biophysical Journal*, 96(7):2888 – 2900.

Broedersz, C. P. and MacKintosh, F. C. (2014). Modeling semiflexible polymer networks. *Rev. Mod. Phys.*, 86:995–1036.

Broedersz, C. P., Mao, X., Lubensky, T. C., and MacKintosh, F. C. (2011). Criticality and isostaticity in fibre networks. *Nature Physics*, 7(12):983–988.

Burnette, D. T., Manley, S., Sengupta, P., Sougrat, R., Davidson, M. W., Kachar, B., and Lippincott-Schwartz, J. (2011). A role for actin arcs in the leading-edge advance of migrating cells. *Nature Cell Biology*, 13(4):371–382.

Burnette, D. T., Shao, L., Ott, C., Pasapera, A. M., Fischer, R. S., Baird, M. A., Der Loughian, C., Delanoe-Ayari, H., Paszek, M. J., Davidson, M. W., Betzig, E., and Lippincott-Schwartz, J. (2014). A contractile and counterbalancing adhesion system controls the 3D shape of crawling cells. *Journal of Cell Biology*, 205(1):83–96.

Burridge, K. and Guilluy, C. (2016). Focal adhesions, stress fibers and mechanical tension. *Exp Cell Res*, 343(1):14–20.

Butler, J. P., Tolić-Nørrelykke, I. M., Fabry, B., and Fredberg, J. J. (2002). Traction fields, moments, and strain energy that cells exert on their surroundings. *Am J Physiol Cell Physiol*, 282(3):C595–605.

Cai, Y., Rossier, O., Gauthier, N. C., Biais, N., Fardin, M.-A., Zhang, X., Miller, L. W., Ladoux, B., Cornish, V. W., and Sheetz, M. P. (2010). Cytoskeletal coherence requires myosin-iia contractility. *Journal of Cell Science*, 123(3):413–423.

Carlier, M.-F. and Shekhar, S. (2017). Global treadmilling coordinates actin turnover and controls the size of actin networks. *Nature Reviews Molecular Cell Biology*, 18(6):389–401.

Chaaban, S. and Brouhard, G. J. (2017). A microtubule bestiary: structural diversity in tubulin polymers. *Mol Biol Cell*, 28(22):2924–2931.

Charras, G. and Paluch, E. (2008). Blebs lead the way: how to migrate without lamellipodia. *Nature Reviews Molecular Cell Biology*, 9(9):730–736.

Cheffings, T. H., Burroughs, N. J., and Balasubramanian, M. K. (2016). Actomyosin ring formation and tension generation in eukaryotic cytokinesis. *Current Biology*, 26(15):R719 – R737.

Chen, B.-C., Legant, W. R., Wang, K., Shao, L., Milkie, D. E., Davidson, M. W., Janetopoulos, C., Wu, X. S., Hammer, J. A., Liu, Z., English, B. P., Mimori-Kiyosue, Y., Romero, D. P., Ritter, A. T., Lippincott-Schwartz, J., Fritz-Laylin, L., Mullins, R. D., Mitchell, D. M., Bembenek, J. N., Reymann, A.-C., Böhme, R., Grill, S. W., Wang, J. T., Seydoux, G., Tulu, U. S., Kiehart, D. P., and Betzig, E. (2014). Lattice light-sheet microscopy: Imaging molecules to embryos at high spatiotemporal resolution. *Science*, 346(6208).

Choi, C. K., Vicente-Manzanares, M., Zareno, J., Whitmore, L. A., Mogilner, A., and Horwitz, A. R. (2008). Actin and α-actinin orchestrate the assembly and maturation of nascent adhesions in a myosin ii motor-independent manner. *Nature Cell Biology*, 10(9):1039–1050.

Craig, E. M., Stricker, J., Gardel, M., and Mogilner, A. (2015). Model for adhesion clutch explains biphasic relationship between actin flow and traction at the cell leading edge. *Phys Biol*, 12(3):035002.

Craig, R. (2017). Molecular structure of muscle filaments determined by electron microscopy. *Appl Microsc*, 47(4):226–232.

Cramer, L. P., Kay, R. R., and Zatulovskiy, E. (2018). Repellent and attractant guidance cues initiate cell migration by distinct rear-driven and front-driven cytoskeletal mechanisms. *Curr Biol*, 28(6):995–1004.

Cramer, L. P., Mitchison, T. J., and Theriot, J. A. (1994). Actin-dependent motile forces and cell motility. *Curr Opin Cell Biol*, 6(1):82–86.

Curtis, A. S. (1964). The mechanism of adhesion of cells to glass. a study by interference reflection microscopy. *J Cell Biol*, 20(2):199–215.

De La Cruz, E. M. and Pollard, T. D. (1996). Kinetics and thermodynamics of phalloidin binding to actin filaments from three divergent species. *Biochemistry*, 35(45):14054–14061.

Dominguez, R. and Holmes, K. C. (2011). Actin structure and function. *Annual Review of Biophysics*, 40(1):169–186. PMID: 21314430.

Doubrovinski, K. and Kruse, K. (2008). Cytoskeletal waves in the absence of molecular motors. *EPL (Europhysics Letters)*, 83(1):18003.

Dreher, A., Aranson, I. S., and Kruse, K. (2014). Spiral actin-polymerization waves can generate amoeboidal cell crawling. *New Journal of Physics*, 16(5):055007.

Driscoll, M. K. and Danuser, G. (2015). Quantifying modes of 3d cell migration. *Trends in Cell Biology*, 25(12):749–759.

Du, X., Doubrovinski, K., and Osterfield, M. (2012). Self-organized cell motility from motor-filament interactions. *Biophysical Journal*, 102(8):1738 – 1745.

Engler, A. J., Sen, S., Sweeney, H. L., and Discher, D. E. (2006). Matrix elasticity directs stem cell lineage specification. *Cell*, 126(4):677–689.

Finer, J. T., Simmons, R. M., and Spudich, J. A. (1994). Single myosin molecule mechanics: piconewton forces and nanometre steps. *Nature*, 368(6467):113–119.

Fouchard, J., Bimbard, C., Bufi, N., Durand-Smet, P., Proag, A., Richert, A., Cardoso, O., and Asnacios, A. (2014). Three-dimensional cell body shape dictates the onset of traction force generation and growth of focal adhesions. *Proceedings of the National Academy of Sciences*, 111(36):13075–13080.

Fournier, M. F., Sauser, R., Ambrosi, D., Meister, J.-J., and Verkhovsky, A. B. (2010). Force transmission in migrating cells. *Journal of Cell Biology*, 188(2):287–297.

Gabella, C., Bertseva, E., Bottier, C., Piacentini, N., Bornert, A., Jeney, S., Forró, L., Sbalzarini, I. F., Meister, J.-J., and Verkhovsky, A. B. (2014). Contact angle at the leading edge controls cell protrusion rate. *Current Biology*, 24(10):1126 – 1132.

Galbraith, C. G., Yamada, K. M., and Sheetz, M. P. (2002). The relationship between force and focal complex development. *J Cell Biol*, 159(4):695–705.

Gardel, M. L., Sabass, B., Ji, L., Danuser, G., Schwarz, U. S., and Waterman, C. M. (2008). Traction stress in focal adhesions correlates biphasically with actin retrograde flow speed. *J Cell Biol*, 183(6):999–1005.

Gardel, M. L., Schneider, I. C., Aratyn-Schaus, Y., and Waterman, C. M. (2010). Mechanical integration of actin and adhesion dynamics in cell migration. *Annu Rev Cell Dev Biol*, 26:315–333.

Gauthier, N. C., Masters, T. A., and Sheetz, M. P. (2012). Mechanical feedback between membrane tension and dynamics. *Trends in Cell Biology*, 22(10):527 – 535.

Geiger, B., Spatz, J. P., and Bershadsky, A. D. (2009). Environmental sensing through focal adhesions. *Nature Reviews Molecular Cell Biology*, 10(1):21–33.

Geiger, B. and Yamada, K. M. (2011). Molecular architecture and function of matrix adhesions. *Cold Spring Harb Perspect Biol*, 3(5).

Gerhardt, M., Ecke, M., Walz, M., Stengl, A., Beta, C., and Gerisch, G. (2014). Actin and pip3 waves in giant cells reveal the inherent length scale of an excited state. *Journal of Cell Science*, 127(20):4507–4517.

Giannone, G., Dubin-Thaler, B. J., Döbereiner, H.-G., Kieffer, N., Bresnick, A. R., and Sheetz, M. P. (2004). Periodic lamellipodial contractions correlate with rearward actin waves. *Cell*, 116(3):431–443.

Ginsberg, M. H. (2014). Integrin activation. *BMB Rep*, 47(12):655–659.

Gittes, F., Mickey, B., Nettleton, J., and Howard, J. (1993). Flexural rigidity of microtubules and actin filaments measured from thermal fluctuations in shape. *J Cell Biol*, 120(4):923–934.

Grashoff, C., Hoffman, B. D., Brenner, M. D., Zhou, R., Parsons, M., Yang, M. T., McLean, M. A., Sligar, S. G., Chen, C. S., Ha, T., and Schwartz, M. A. (2010). Measuring mechanical tension across vinculin reveals regulation of focal adhesion dynamics. *Nature*, 466(7303):263–266.

Grimm, H. P., Verkhovsky, A. B., Mogilner, A., and Meister, J. J. (2003). Analysis of actin dynamics at the leading edge of crawling cells: implications for the shape of keratocyte lamellipodia. *European Biophysics Journal*, 32(6):563–577.

Guo, W.-H., Frey, M. T., Burnham, N. A., and li Wang, Y. (2006). Substrate rigidity regulates the formation and maintenance of tissues. *Biophysical Journal*, 90(6):2213 – 2220.

Gupton, S. L. and Waterman-Storer, C. M. (2006). Spatiotemporal feedback between actomyosin and focal-adhesion systems optimizes rapid cell migration. *Cell*, 125(7):1361–1374.

Hall, A. (2012). Rho family GTPases. *Biochemical Society Transactions*, 40(6):1378–1382.

Harris, A. K., Wild, P., and Stopak, D. (1980). Silicone rubber substrata: a new wrinkle in the study of cell locomotion. *Science*, 208(4440):177–179.

Heasman, S. J. and Ridley, A. J. (2008). Mammalian rho gtpases: new insights into their functions from in vivo studies. *Nature Reviews Molecular Cell Biology*, 9(9):690–701.

Henderson, C. A., Gomez, C. G., Novak, S. M., Mi-Mi, L., and Gregorio, C. C. (2017). Overview of the muscle cytoskeleton. *Compr Physiol*, 7(3):891–944.

Hierro-Bujalance, C., Bacskai, B. J., and Garcia-Alloza, M. (2018). In vivo imaging of microglia with multiphoton microscopy. *Front Aging Neurosci*, 10:218.

Higgs, H. N. (2018). A fruitful tree: developing the dendritic nucleation model of actin-based cell motility. *Molecular Biology of the Cell*, 29(25):2969–2978.

Holenstein, C., Lendi, C., Wili, N., and Snedeker, J. (2019). Simulation and evaluation of 3d traction force microscopy. *Computer Methods in Biomechanics and Biomedical Engineering*, 22(8):853–860. PMID: 30963777.

Hotulainen, P. and Lappalainen, P. (2006). Stress fibers are generated by two distinct actin assembly mechanisms in motile cells . *Journal of Cell Biology*, 173(3):383–394.

Hu, X., Margadant, F. M., Yao, M., and Sheetz, M. P. (2017). Molecular stretching modulates mechanosensing pathways. *Protein Science*, 26(7):1337–1351.

Humphries, J. D., Wang, P., Streuli, C., Geiger, B., Humphries, M. J., and Ballestrem, C. (2007). Vinculin controls focal adhesion formation by direct interactions with talin and actin. *J Cell Biol*, 179(5):1043–1057.

Ji, L., Lim, J., and Danuser, G. (2008). Fluctuations of intracellular forces during cell protrusion. *Nature Cell Biology*, 10(12):1393–1400.

Jilkine, A. and Edelstein-Keshet, L. (2011). A comparison of mathematical models for polarization of single eukaryotic cells in response to guided cues. *PLOS Computational Biology*, 7(4):1–15.

Juliano, R. L. (2002). Signal transduction by cell adhesion receptors and the cytoskeleton: Functions of integrins, cadherins, selectins, and immunoglobulin-superfamily members. *Annual Review of Pharmacology and Toxicology*, 42(1):283–323. PMID: 11807174.

Jurado, C., Haserick, J. R., and Lee, J. (2005). Slipping or gripping? fluorescent speckle microscopy in fish keratocytes reveals two different mechanisms for generating a retrograde flow of actin. *Mol Biol Cell*, 16(2):507–518.

Kaverina, I., Krylyshkina, O., and Small, J. (2002). Regulation of substrate adhesion dynamics during cell motility. *The International Journal of Biochemistry and Cell Biology*, 34(7):746 – 761.

Kendall, R. T. and Feghali-Bostwick, C. A. (2014). Fibroblasts in fibrosis: novel roles and mediators. *Frontiers in Pharmacology*, 5:123.

Keren, K., Pincus, Z., Allen, G. M., Barnhart, E. L., Marriott, G., Mogilner, A., and Theriot, J. A. (2008). Mechanism of shape determination in motile cells. *Nature*, 453(7194):475–480.

Kim, D.-H., Han, K., Gupta, K., Kwon, K. W., Suh, K.-Y., and Levchenko, A. (2009). Mechanosensitivity of fibroblast cell shape and movement to anisotropic substratum topography gradients. *Biomaterials*, 30(29):5433 – 5444.

Korenbaum, E., Nordberg, P., Björkegren-Sjögren, C., Schutt, C. E., Lindberg, U., and Karlsson, R. (1998). The role of profilin in actin polymerization and nucleotide exchange. *Biochemistry*, 37(26):9274–9283.

Kratky, O. and Porod, G. (1949). Röntgenuntersuchung gelöster fadenmoleküle. *Recueil des Travaux Chimiques des Pays-Bas*, 68(12):1106–1122.

Kuhn, J. R. and Pollard, T. D. (2005). Real-time measurements of actin filament polymerization by total internal reflection fluorescence microscopy. *Biophys J*, 88(2):1387–1402.

Kulkarni, A. H., Ghosh, P., Seetharaman, A., Kondaiah, P., and Gundiah, N. (2018). Traction cytometry: regularization in the fourier approach and comparisons with finite element method. *Soft Matter*, 14(23):4687–4695.

Landau L.D., L. E. (1986). *Theory of elasticity*. Pergamon, 3rd edition.

Langanger, G., Moeremans, M., Daneels, G., Sobieszek, A., De Brabander, M., and De Mey, J. (1986). The molecular organization of myosin in stress fibers of cultured cells. *J Cell Biol*, 102(1):200–209.

Langhans, S. A. (2018). Three-dimensional in vitro cell culture models in drug discovery and drug repositioning. *Frontiers in Pharmacology*, 9:6.

Lauffenburger, D. A. and Horwitz, A. F. (1996). Cell migration: a physically integrated molecular process. *Cell*, 84(3):359–369.

Laurent, V. M., Kasas, S., Yersin, A., Schäffer, T. E., Catsicas, S., Dietler, G., Verkhovsky, A. B., and Meister, J.-J. (2005). Gradient of rigidity in the lamellipodia of migrating cells revealed by atomic force microscopy. *Biophysical Journal*, 89(1):667 – 675.

Lee, J., Ishihara, A., Theriot, J. A., and Jacobson, K. (1993). Principles of locomotion for simple-shaped cells. *Nature*, 362(6416):167–171.

Li, S., Mecca, A., Kim, J., Caprara, G. A., Wagner, E. L., Du, T.-T., Petrov, L., Xu, W., Cui, R., Rebustini, I. T., Kachar, B., Peng, A. W., and Shin, J.-B. (2020). Myosin-viia is expressed in multiple isoforms and essential for tensioning the hair cell mechanotransduction complex. *Nature Communications*, 11(1):2066.

Li, Y., Bhimalapuram, P., and Dinner, A. R. (2010). Model for how retrograde actin flow regulates adhesion traction stresses. *J Phys Condens Matter*, 22(19):194113.

Lieber, A. D., Yehudai-Resheff, S., Barnhart, E. L., Theriot, J. A., and Keren, K. (2013). Membrane tension in rapidly moving cells is determined by cytoskeletal forces. *Current Biology*, 23(15):1409 – 1417.

Linsmeier, I., Banerjee, S., Oakes, P. W., Jung, W., Kim, T., and Murrell, M. P. (2016). Disordered actomyosin networks are sufficient to produce cooperative and telescopic contractility. *Nature Communications*, 7(1):12615.

Liu, S.-L., May, J. R., Helgeson, L. A., and Nolen, B. J. (2013). Insertions within the actin core of actin-related protein 3 (arp3) modulate branching nucleation by arp2/3 complex. *J Biol Chem*, 288(1):487–497.

Machacek, M. and Danuser, G. (2006). Morphodynamic profiling of protrusion phenotypes. *Biophysical Journal*, 90(4):1439 – 1452.

MacKintosh, C. and MacKintosh, R. W. (1994). Inhibitors of protein kinases and phosphatases. *Trends Biochem Sci*, 19(11):444–448.

Maiuri, P., Rupprecht, J.-F., Wieser, S., Ruprecht, V., Bénichou, O., Carpi, N., Coppey, M., Beco, S. D., Gov, N., Heisenberg, C.-P., Crespo, C. L., Lautenschlaeger, F., Berre, M. L., Lennon-Dumenil, A.-M., Raab, M., Thiam, H.-R., Piel, M., Sixt, M., and Voituriez, R. (2015). Actin flows mediate a universal coupling between cell speed and cell persistence. *Cell*, 161(2):374 – 386.

Martin, S. G. (2009). Microtubule-dependent cell morphogenesis in the fission yeast. *Trends in Cell Biology*, 19(9):447 – 454.

Martino, F., Perestrelo, A. R., Vinarský, V., Pagliari, S., and Forte, G. (2018). Cellular mechanotransduction: From tension to function. *Frontiers in Physiology*, 9:824.

Mattila, P. K. and Lappalainen, P. (2008). Filopodia: molecular architecture and cellular functions. *Nature Reviews Molecular Cell Biology*, 9(6):446–454.

Maugis, B., Brugués, J., Nassoy, P., Guillen, N., Sens, P., and Amblard, F. (2010). Dynamic instability of the intracellular pressure drives bleb-based motility. *Journal of Cell Science*, 123(22):3884–3892.

Messi, Z., Bornert, A., Raynaud, F., and Verkhovsky, A. B. (2020). Traction forces control cell-edge dynamics and mediate distance sensitivity during cell polarization. *Current Biology*, 30(9):1762 – 1769.e5.

Millius, A., Dandekar, S. N., Houk, A. R., and Weiner, O. D. (2009). Neutrophils establish rapid and robust wave complex polarity in an actin-dependent fashion. *Current Biology*, 19(3):253 – 259.

Mim, C. and Unger, V. M. (2012). Membrane curvature and its generation by bar proteins. *Trends in Biochemical Sciences*, 37(12):526 – 533.

Mogilner, A., Allard, J., and Wollman, R. (2012). Cell polarity: Quantitative modeling as a tool in cell biology. *Science*, 336(6078):175–179.

Morris, C. E. and Homann, U. (2001). Cell surface area regulation and membrane tension. *The Journal of Membrane Biology*, 179(2):79–102.

Mseka, T. and Cramer, L. P. (2011). Actin depolymerization-based force retracts the cell rear in polarizing and migrating cells. *Current Biology*, 21(24):2085 – 2091.

Mullins, R. D., Heuser, J. A., and Pollard, T. D. (1998). The interaction of arp2/3 complex with actin: Nucleation, high affinity pointed end capping, and formation of branching networks of filaments. *Proceedings of the National Academy of Sciences*, 95(11):6181–6186.

Munjal, A. and Lecuit, T. (2014). Actomyosin networks and tissue morphogenesis. *Development*, 141(9):1789–1793.

Myasnikova, E., Samsonova, A., Kozlov, K., Samsonova, M., and Reinitz, J. (2001). Registration of the expression patterns of drosophila segmentation genes by two independent methods. *Bioinformatics*, 17(1):3–12.

Narang, A. (2006). Spontaneous polarization in eukaryotic gradient sensing: A mathematical model based on mutual inhibition of frontness and backness pathways. *Journal of Theoretical Biology*, 240(4):538 – 553.

Nicholson-Dykstra, S., Higgs, H. N., and Harris, E. S. (2005). Actin dynamics: Growth from dendritic branches. *Current Biology*, 15(9):R346 – R357.

Nishimura, S. I., Ueda, M., and Sasai, M. (2009). Cortical factor feedback model for cellular locomotion and cytofission. *PLOS Computational Biology*, 5(3):1–11.

Oakes, P. W., Banerjee, S., Marchetti, M. C., and Gardel, M. L. (2014). Geometry regulates traction stresses in adherent cells. *Biophys. J.*, 107(4):825–833.

Okimura, C., Taniguchi, A., Nonaka, S., and Iwadate, Y. (2018). Rotation of stress fibers as a single wheel in migrating fish keratocytes. *Scientific Reports*, 8(1):10615.

Oliver, T., Dembo, M., and Jacobson, K. (1999). Separation of propulsive and adhesive traction stresses in locomoting keratocytes. *Journal of Cell Biology*, 145(3):589–604. cited By 135.

Panzetta, V., Fusco, S., and Netti, P. A. (2019). Cell mechanosensing is regulated by substrate strain energy rather than stiffness. *Proceedings of the National Academy of Sciences*, 116(44):22004–22013.

Parent, C. A. (2004). Making all the right moves: chemotaxis in neutrophils and dictyostelium. *Current Opinion in Cell Biology*, 16(1):4 – 13.

Parsons, J. T., Horwitz, A. R., and Schwartz, M. A. (2010). Cell adhesion: integrating cytoskeletal dynamics and cellular tension. *Nat Rev Mol Cell Biol*, 11(9):633–643.

Peleg, B., Disanza, A., Scita, G., and Gov, N. (2011). Propagating cell-membrane waves driven by curved activators of actin polymerization. *PLOS ONE*, 6(4):1–11.

Pellegrin, S. and Mellor, H. (2007). Actin stress fibres. *Journal of Cell Science*, 120(20):3491–3499.

Petrie, R. J. and Yamada, K. M. (2012). At the leading edge of three-dimensional cell migration. *Journal of Cell Science*, 125(24):5917–5926.

Piazzesi, G., Reconditi, M., Linari, M., Lucii, L., Bianco, P., Brunello, E., Decostre, V., Stewart, A., Gore, D. B., Irving, T. C., Irving, M., and Lombardi, V. (2007). Skeletal muscle performance determined by modulation of number of myosin motors rather than motor force or stroke size. *Cell*, 131(4):784 – 795.

Picone, R., Ren, X., Ivanovitch, K. D., Clarke, J. D. W., McKendry, R. A., and Baum, B. (2010). A polarised population of dynamic microtubules mediates homeostatic length control in animal cells. *PLOS Biology*, 8(11):1–17.

Pieuchot, L., Marteau, J., Guignandon, A., Dos Santos, T., Brigaud, I., Chauvy, P.-F., Cloatre, T., Ponche, A., Petithory, T., Rougerie, P., Vassaux, M., Milan, J.-L., Tusamda Wakhloo, N., Spangenberg, A., Bigerelle, M., and Anselme, K. (2018). Curvotaxis directs cell migration through cell-scale curvature landscapes. *Nature Communications*, 9(1):3995.

Plotnikov, S. V., Sabass, B., Schwarz, U. S., and Waterman, C. M. (2014). High-resolution traction force microscopy. *Methods Cell Biol*, 123:367–394.

Pollard, T. D. (2019). Cell motility and cytokinesis: From mysteries to molecular mechanisms in five decades. *Annual Review of Cell and Developmental Biology*, 35(1):1–28. PMID: 31394047.

Pollard, T. D. and Borisy, G. G. (2003). Cellular motility driven by assembly and disassembly of actin filaments. *Cell*, 112(4):453 – 465.

Pollitt, A. Y. and Insall, R. H. (2009). Wasp and scar/wave proteins: the drivers of actin assembly. *Journal of Cell Science*, 122(15):2575–2578.

Ponti, A., Machacek, M., Gupton, S. L., Waterman-Storer, C. M., and Danuser, G. (2004). Two distinct actin networks drive the protrusion of migrating cells. *Science*, 305(5691):1782–1786.

Prass, M., Jacobson, K., Mogilner, A., and Radmacher, M. (2006). Direct measurement of the lamellipodial protrusive force in a migrating cell . *Journal of Cell Biology*, 174(6):767–772.

Rafelski, S. M. and Theriot, J. A. (2004). Crawling toward a unified model of cell mobility: spatial and temporal regulation of actin dynamics. *Annu Rev Biochem*, 73:209–239.

Rape, A. D., hui Guo, W., and li Wang, Y. (2011). The regulation of traction force in relation to cell shape and focal adhesions. *Biomaterials*, 32(8):2043–2051.

Raynaud, F., Ambühl, M., Gabella, C., Bornert, A., Sbalzarini, I., Meister, J.-J., and Verkhovsky, A. (2016). Minimal model for spontaneous cell polarization and edge activity in oscillating, rotating and migrating cells. *Nature Physics*, 12.

Roca-Cusachs, P., Iskratsch, T., and Sheetz, M. P. (2012). Finding the weakest link: exploring integrin-mediated mechanical molecular pathways. *J Cell Sci*, 125(Pt 13):3025–3038.

Ronceray, P. (2016). *Active contraction in biological fiber networks*. PhD thesis, Université Paris-Sud.

Ronceray, P., Broedersz, C. P., and Lenz, M. (2016). Fiber networks amplify active stress. *Proceedings of the National Academy of Sciences*, 113(11):2827–2832.

Ronceray, P., Broedersz, C. P., and Lenz, M. (2019). Fiber plucking by molecular motors yields large emergent contractility in stiff biopolymer networks. *Soft Matter*, 15:1481–1487.

Ruprecht, V., Wieser, S., Callan-Jones, A., Smutny, M., Morita, H., Sako, K., Barone, V., Ritsch-Marte, M., Sixt, M., Voituriez, R., and Heisenberg, C.-P. (2015). Cortical contractility triggers a stochastic switch to fast amoeboid cell motility. *Cell*, 160(4):673 – 685.

Ryan, G. L., Petroccia, H. M., Watanabe, N., and Vavylonis, D. (2012). Excitable actin dynamics in lamellipodial protrusion and retraction. *Biophysical Journal*, 102(7):1493 – 1502.

Sabass, B., Gardel, M. L., Waterman, C. M., and Schwarz, U. S. (2008). High resolution traction force microscopy based on experimental and computational advances. *Biophysical Journal*, 94(1):207 – 220.

Sabass, B. and Schwarz, U. S. (2010). Modeling cytoskeletal flow over adhesion sites: competition between stochastic bond dynamics and intracellular relaxation. *Journal of Physics: Condensed Matter*, 22(19):194112.

Schaub, S., Bohnet, S., Laurent, V. M., Meister, J.-J., and Verkhovsky, A. B. (2007). Comparative maps of motion and assembly of filamentous actin and myosin ii in migrating cells. *Mol Biol Cell*, 18(10):3723–3732.

Schmeiser, C. and Winkler, C. (2015). The flatness of lamellipodia explained by the interaction between actin dynamics and membrane deformation. *Journal of Theoretical Biology*, 380:144 – 155.

Schwarz, U. S., Balaban, N. Q., Riveline, D., Bershadsky, A., Geiger, B., and Safran, S. A. (2002). Calculation of forces at focal adhesions from elastic substrate data: the effect of localized force and the need for regularization. *Biophysical journal*, 83(3):1380–1394.

Schwarz, U. S. and Soiné, J. R. (2015). Traction force microscopy on soft elastic substrates: A guide to recent computational advances. *Biochimica et Biophysica Acta (BBA) - Molecular Cell Research*, 1853(11, Part B):3095 – 3104. Mechanobiology.

Selden, L. A., Kinosian, H. J., Estes, J. E., and Gershman, L. C. (1999). Impact of profilin on actin-bound nucleotide exchange and actin polymerization dynamics,. *Biochemistry*, 38(9):2769–2778.

Sellers, J. R. (2000). Myosins: a diverse superfamily. *Biochimica et Biophysica Acta (BBA) - Molecular Cell Research*, 1496(1):3 – 22.

Shao, D., Levine, H., and Rappel, W.-J. (2012). Coupling actin flow, adhesion, and morphology in a computational cell motility model. *Proceedings of the National Academy of Sciences*, 109(18):6851–6856.

Shekhar, S. and Carlier, M.-F. (2016). Single-filament kinetic studies provide novel insights into regulation of actin-based motility. *Mol Biol Cell*, 27(1):1–6.

Shekhar, S. and Carlier, M.-F. (2017). Enhanced depolymerization of actin filaments by adf/cofilin and monomer funneling by capping protein cooperate to accelerate barbed-end growth. *Current Biology*, 27(13):1990 – 1998.e5.

Sixt, M. (2012). Cell migration: fibroblasts find a new way to get ahead. *J Cell Biol*, 197(3):347–349.

Sjöblom, B., Salmazo, A., and Djinović-Carugo, K. (2008). Alpha-actinin structure and regulation. *Cell Mol Life Sci*, 65(17):2688–2701.

Stricker, J., Sabass, B., Schwarz, U. S., and Gardel, M. L. (2010). Optimization of traction force microscopy for micron-sized focal adhesions. *J Phys Condens Matter*, 22(19):194104.

Suetsugu, S. and Gautreau, A. (2012). Synergistic bar–npf interactions in actin-driven membrane remodeling. *Trends in Cell Biology*, 22(3):141 – 150.

Svitkina, T., Bulanova, E., Chaga, O., Vignjevic, D., Kojima, S.-I., Vasiliev, J., and Borisy, G. (2003). Mechanism of filopodia initiation by reorganization of a dendritic network. *Journal of Cell Biology*, 160(3):409–421. cited By 528.

Svitkina, T. M., Verkhovsky, A. B., McQuade, K. M., and Borisy, G. G. (1997). Analysis of the Actin–Myosin II System in Fish Epidermal Keratocytes: Mechanism of Cell Body Translocation . *Journal of Cell Biology*, 139(2):397–415.

Swaminathan, V., Kalappurakkal, J. M., Mehta, S. B., Nordenfelt, P., Moore, T. I., Koga, N., Baker, D. A., Oldenbourg, R., Tani, T., Mayor, S., Springer, T. A., and Waterman, C. M. (2017). Actin retrograde flow actively aligns and orients ligand-engaged integrins in focal adhesions. *Proc Natl Acad Sci U S A*, 114(40):10648–10653.

Tan, J. L., Tien, J., Pirone, D. M., Gray, D. S., Bhadriraju, K., and Chen, C. S. (2003). Cells lying on a bed of microneedles: An approach to isolate mechanical force. *Proceedings of the National Academy of Sciences*, 100(4):1484–1489.

The CGAL Project (2020). *CGAL User and Reference Manual*. CGAL Editorial Board, 5.1.1 edition.

Tikhonov, A. N. and Arsenin, V. Y. (1977). *Solutions of Ill-posed problems*. W.H. Winston.

Tojkander, S., Gateva, G., and Lappalainen, P. (2012). Actin stress fibers – assembly, dynamics and biological roles. *Journal of Cell Science*, 125(8):1855–1864.

Tse, J. R. and Engler, A. J. (2010). Preparation of hydrogel substrates with tunable mechanical properties. *Curr Protoc Cell Biol*, Chapter 10:Unit 10.16.

Tseng, Q., Duchemin-Pelletier, E., Deshiere, A., Balland, M., Guillou, H., Filhol, O., and Théry, M. (2012). Spatial organization of the extracellular matrix regulates cell-cell junction positioning. *Proceedings of the National Academy of Sciences of the United States of America*, 109(5):1506–1511.

Turing, A. M. (1952). The chemical basis of morphogenesis. *Philosophical Transactions of the Royal Society of London. Series B, Biological Sciences*, 237(641):37–72.

Tyska, M. J. and Warshaw, D. M. (2002). The myosin power stroke. *Cell Motil Cytoskeleton*, 51(1):1–15.

Vale, R. D. (2003). The molecular motor toolbox for intracellular transport. *Cell*, 112(4):467–480.

Vallotton, P., Danuser, G., Bohnet, S., Meister, J.-J., and Verkhovsky, A. B. (2005). Tracking retrograde flow in keratocytes: news from the front. *Molecular biology of the cell*, 16(3):1223–1231.

Vallotton, P., Gupton, S. L., Waterman-Storer, C. M., and Danuser, G. (2004). Simultaneous mapping of filamentous actin flow and turnover in migrating cells by quantitative fluorescent speckle microscopy. *Proceedings of the National Academy of Sciences*, 101(26):9660–9665.

van der Flier, A. and Sonnenberg, A. (2001). Structural and functional aspects of filamins. *Biochimica et Biophysica Acta (BBA) - Molecular Cell Research*, 1538(2):99 – 117.

Van Haastert, P. J. M. and Devreotes, P. N. (2004). Chemotaxis: signalling the way forward. *Nat Rev Mol Cell Biol*, 5(8):626–634.

Venneman, P. (2020). Jpiv.

Verkhovsky, A. B. (2015). The mechanisms of spatial and temporal patterning of cell-edge dynamics. *Curr Opin Cell Biol*, 36:113–121.

Verkhovsky, A. B., Svitkina, T. M., and Borisy, G. G. (1995). Myosin ii filament assemblies in the active lamella of fibroblasts: their morphogenesis and role in the formation of actin filament bundles. *Journal of Cell Biology*, 131(4):989–1002.

Verkhovsky, A. B., Svitkina, T. M., and Borisy, G. G. (1999). Self-polarization and directional motility of cytoplasm. *Curr Biol*, 9(1):11–20.

Verschueren, H. (1985). Interference reflection microscopy in cell biology: methodology and applications. *Journal of Cell Science*, 75(1):279–301.

Vianay, B., Senger, F., Alamos, S., Anjur-Dietrich, M., Bearce, E., Cheeseman, B., Lee, L., and Théry, M. (2018). Variation in traction forces during cell cycle progression. *Biology of the Cell*, 110(4):91–96.

Vicker, M. G. (2002). Eukaryotic cell locomotion depends on the propagation of self-organized reaction–diffusion waves and oscillations of actin filament assembly. *Experimental Cell Research*, 275(1):54 – 66.

Vinzenz, M., Nemethova, M., Schur, F., Mueller, J., Narita, A., Urban, E., Winkler, C., Schmeiser, C., Koestler, S. A., Rottner, K., Resch, G. P., Maeda, Y., and Small, J. V. (2012). Actin branching in the initiation and maintenance of lamellipodia. *Journal of Cell Science*, 125(11):2775–2785.

Volkmann, N., Amann, K. J., Stoilova-McPhie, S., Egile, C., Winter, D. C., Hazelwood, L., Heuser, J. E., Li, R., Pollard, T. D., and Hanein, D. (2001). Structure of arp2/3 complex in its activated state and in actin filament branch junctions. *Science*, 293(5539):2456–2459.

Wang, X. and Carlsson, A. E. (2014). Feedback mechanisms in a mechanical model of cell polarization. *Physical Biology*, 11(6):066002.

Waterman-Storer, C. M., Desai, A., Chloe Bulinski, J., and Salmon, E. (1998). Fluorescent speckle microscopy, a method to visualize the dynamics of protein assemblies in living cells. *Current Biology*, 8(22):1227 – S1.

Weiner, O. D., Marganski, W. A., Wu, L. F., Altschuler, S. J., and Kirschner, M. W. (2007). An actin-based wave generator organizes cell motility. *PLOS Biology*, 5(9):1–11.

Weiner, O. D., Neilsen, P. O., Prestwich, G. D., Kirschner, M. W., Cantley, L. C., and Bourne, H. R. (2002). A ptdinsp3- and rho gtpase-mediated positive feedback loop regulates neutrophil polarity. *Nature Cell Biology*, 4(7):509–513.

Wells, A. L., Lin, A. W., Chen, L.-Q., Safer, D., Cain, S. M., Hasson, T., Carragher, B. O., Milligan, R. A., and Sweeney, H. L. (1999). Myosin vi is an actin-based motor that moves backwards. *Nature*, 401(6752):505–508.

Wilson, C. A., Tsuchida, M. A., Allen, G. M., Barnhart, E. L., Applegate, K. T., Yam, P. T., Ji, L., Keren, K., Danuser, G., and Theriot, J. A. (2010). Myosin ii contributes to cell-scale actin network treadmilling through network disassembly. *Nature*, 465(7296):373–377.

Wolven, A. K., Belmont, L. D., Mahoney, N. M., Almo, S. C., and Drubin, D. G. (2000). In vivo importance of actin nucleotide exchange catalyzed by profilin. *J Cell Biol*, 150(4):895–904.

Wong, K., Pertz, O., Hahn, K., and Bourne, H. (2006). Neutrophil polarization: Spatiotemporal dynamics of rhoa activity support a self-organizing mechanism. *Proceedings of the National Academy of Sciences*, 103(10):3639–3644.

Woolley, D. M., Crockett, R. F., Groom, W. D. I., and Revell, S. G. (2009). A study of synchronisation between the flagella of bull spermatozoa, with related observations. *Journal of Experimental Biology*, 212(14):2215–2223.

Xiong, Y., Huang, C.-H., Iglesias, P. A., and Devreotes, P. N. (2010). Cells navigate with a local-excitation, global-inhibition-biased excitable network. *Proceedings of the National Academy of Sciences*, 107(40):17079–17086.

Yam, P. T., Wilson, C. A., Ji, L., Hebert, B., Barnhart, E. L., Dye, N. A., Wiseman, P. W., Danuser, G., and Theriot, J. A. (2007). Actin–myosin network reorganization breaks symmetry at the cell rear to spontaneously initiate polarized cell motility . *Journal of Cell Biology*, 178(7):1207–1221.

Yamashiro, S. and Watanabe, N. (2014). A new link between the retrograde actin flow and focal adhesions. *The Journal of Biochemistry*, 156(5):239–248.

Yang, C. and Svitkina, T. (2011). Filopodia initiation: focus on the arp2/3 complex and formins. *Cell Adh Migr*, 5(5):402–408.

Yip, A. K., Iwasaki, K., Ursekar, C., Machiyama, H., Saxena, M., Chen, H., Harada, I., Chiam, K.-H., and Sawada, Y. (2013). Cellular response to substrate rigidity is governed by either stress or strain. *Biophysical Journal*, 104(1):19 – 29.

Ziebert, F. and Aranson, I. S. (2013). Effects of adhesion dynamics and substrate compliance on the shape and motility of crawling cells. *PLOS ONE*, 8(5):1–14.

Ziebert, F., Swaminathan, S., and Aranson, I. S. (2012). Model for self-polarization and motility of keratocyte fragments. *Journal of The Royal Society Interface*, 9(70):1084–1092.

Zeno Messi
BSP-413 EPFL
1015 Lausanne
Switzerland

Phone : +41 21 6933359
Website: https://www.epfl.ch/labs/lbem/
http://people.epfl.ch/zeno.messi
E-mail : zeno.messi@epfl.ch

Education

2017-Present	**PhD** EPFL, Switzerland
2014-2015	**Scientific Assistant** EPFL Laboratory of Cell Biophysics
2009-2014	**Bachelor and Master** EPFL MSc thesis supervisor : Prof. Paolo De Los Rios.

Research projects

2014–Present	**Mechanisms of cell polarization and organization of the cell-edge** Swiss National Science Foundation grant

Publications

Traction Forces Control Cell-Edge Dynamics and Mediate Distance Sensitivity during Cell Polarization. *Messi Z., Bornert A., Raynaud F., Verkhovksy A.B.*
Current Biology 30(9):1762 - 1769, May 2020

Teaching

Teaching assistant for courses

- Basic physics courses for undergraduate students

  Thermodynamics, mechanics, electromagnetism, etc.

Conferences Summer Schools (selection)

2017	**EMBL Symposium: Mechanical Forces in Biology** Heidelberg, Germany **5th Swiss-Japan Workshop on Biomechanics** Zermatt, Switzerland
2018	**3rd Course on Multiscale Integration in Biological Systems** Paris, France
2019	**Quantitative biology: Bridging the gap between computational and experimental approaches** Fiesch, Switzerland
2020	**Biophysical Society Annual Meeting** San Diego, USA